Forschungszentrum Jülich
in der Helmholtz-Gemeinschaft

Institut für Bio- und Nanosysteme
Institut 2: Bioelektronik

Transport and noise properties of AlGaN/GaN heterostructures for high-frequency applications

Andriy Kurakin

Zusammenfassung

Gruppe-III-Nitride und insbesondere Werkstoffe auf Gallium-Nitrid-Basis erfahren zunehmend mehr Aufmerksamkeit bei Wissenschaftlern im Bereich der Hochleistungs- und Hochfrequenz-Elektronik für den Einsatz in künftigen Kommunikationssystemen. Deren breite Bandlücke (z.B. GaN – 3,4 eV, AlN – 6,2 eV) erlaubt es diese Halbleiterwerkstoffe bei viel höheren Temperaturen und höherer ionisierender Strahlung zu betreiben, als das bei konventionellem GaAs oder Si möglich wäre. Die höhere Driftgeschwindigkeit und das höhere elektrische Feld der III-Nitrid-Werkstoffe ermöglichen eine hohe Ausgangsleistung bei hohen Frequenzen von bis zu 1 THz. Die Verwendung von HF-Verstärkern auf der Basis dieser Werkstoffe führt zu einer höheren Ausgangsleistung, die vergleichbar mit der von Vakuumbauelementen ist. Die höhere Durchbruchfeldstärke dieser Werkstoffe erlaubt eine weitreichende Miniaturisierung der Bauelemente und Optimierung des Stromverbrauchs. Trotz der oben angeführten Fortschritte und Vorteile der III-Nitrid-Halbleiter wird die kommerzielle Markteinführung der auf diesen Werkstoffen basierenden Elektronik noch dauern, da eine Untersuchung der Faktoren, die die Leistung und Zuverlässigkeit von Bauelementen auf III-Nitrid-Basis begrenzen, noch aussteht.

Diese Arbeit konzentriert auf eine umfassende Charakterisierung von Einzel- und Doppelbarriere-AlGaN/GaN-Strukturen und auf eine Analyse der Transportphänomene in diesen Strukturen. Gegenstand dieser Untersuchung sind High-Electron-Mobility-Transistoren (HEMT) und Resonanztunneldioden (RTD) auf der Basis von AlGaN/GaN-Heterostrukturen. Im Rahmen dieser Arbeit wurden Werkstoff- und Bauelementtechnologien entwickelt und unterschiedliche Bauelemente zur Untersuchung der Transporteigenschaften der AlGaN/GaN-Heterostrukturen hergestellt. Einige Metallisierungsschemata und Wärmebehandlungsprogramme wurden auf zuverlässige Bildung der ohmschen Kontakte geprüft. Mehrere Lithographiemasken wurden zur Erreichung der Arbeitsziele konstruiert und entwickelt. Ein Teil dieser Arbeit beschäftigte sich mit der Automatisierung des Versuchsablaufs und der Versuchapparatur, so dass ein Programm erfolgreich in der Delphi-Sprache geschrieben und bei Messungen eingesetzt werden konnte. Das Programm dient dazu, die Messeinrichtungen zu kontrollieren und die Versuchsdaten zu erfassen.

Als historischer Ausgangspunkt für die Arbeit diente eine Untersuchung der Strahlungshärte von AlGaN/GaN-HEMT zur Abschätzung des Potentials der III-Nitride für Satellitenanwendungen. Trotz deutlicher Verschlechterung der Bauelementleistung (in einigen Fällen zeigen die Bauelemente nur 50 % ihrer Ausgangsleistung) funktionieren sie noch bei einer sehr hohen Gamma-Strahlungsdosis ($2x10^9$ Rad). (Man beachte, dass laut Literaturangaben HEMT auf GaAs-Basis katastrophales Versagen bei einer hohen Gamma-Strahlungsdosis von bis zu $6x10^8$ Rad aufweisen.) Die erstaunlichste Wirkung der Gamma-Strahlung zeigt sich in der Verbesserung der HEMT-Betriebsparameter und einer deutlichen Abnahme ihrer Ausbreitung über den Wafer bei niedrigen Dosen (unter 10^6 Rad). Um diese strahlungsbedingte Verbesserung besser zu verstehen, wurden verschiedene Strukturuntersuchungen (XRD, Auger) an Proben vorgenommen. Es zeigte sich, dass die Relaxation der mechanischen Spannung in der Struktur und die strahlungsbedingte Struktur- und Defektordnung für diese Verbesserung verantwortlich sind. Seitdem werden kleine Gammastrahlungsdosen bei der Bauelementfertigung eingesetzt.

Kürzlich wurde eine deutliche Verbesserung der Niedrigtemperaturmobilität und der Quantumlebensdauer nach Einsatz einer kleinen Gammastrahlungsdosis festgestellt.

Kenntnisse der grundlegenden Parameter der Werkstoffe und der Bedingungen, die diese Parameter beeinflussen, sind für eine Leistungsanalyse der DC- und HF-Bauelemente wichtig. Die Niedrigtemperatur-Nanotransportmessungen und die temperaturabhängigen Charakterisierungen sind sehr empfindliche Methoden zur Feststellung der Transporteigenschaften bei Halbleiterstrukturen. Die effektive Masse, Quantumlebensdauer und Elektronendichte wurden für jede Probe erfasst. Anhand einer umfassenden Analyse dieser Daten und der technologischen Parameter der aktuellen Strukturen (Schichtdicke und –zusammensetzung) wurde eine empirische Abhängigkeit der effektiven Masse von der Schichtzusammensetzung festgestellt. Eine sorgfältige Analyse des Niedrigfeld-Magnetotransports der 2DEG in AlGaN/GaN-Heterostrukturen zeigte Besonderheiten hinsichtlich der Spin-Bahn-Wechselwirkung im hochdichten Elektronengas.

Eine weitere wichtige Frage bezüglich der Zuverlässigkeit von AlGaN/GaN-HEMT betrifft die Selbsterhitzung während des Betriebs. Das Problem der thermischen Bilanz wurde für die konventionelle Geometrie des Transistors gelöst. Der Einfluss der thermischen Leitfähigkeit des Substrats und der Dicke der GaN-Pufferschicht auf die Höhe der Überhitzung wurden als kritisch eingestuft.

Temperaturabhängige Messungen der Rauschspektra der AlGaN/GaN-HEMT sind für das Abschätzen der HF-Leistung von Bedeutung. Durch Untersuchungen der Rauschspektra konnten die Eigenschaften der Rauschquellen in den Kontakten und in den aktiven und passiven Bereichen der HEMT definiert werden. Es wurde auch gezeigt, dass die einfache Verwendung einer dünnen Zwischenschicht oder Deckschicht in die Bauelementenstruktur eine deutliche Abnahme des Rauschens in AlGaN/GaN-Bauelementen bewirken kann. Diese Ergebnisse eignen sich als Richtlinien zur Optimierung der Bauelementenstruktur.

Resonanztunneldioden zeigen großes Potential für HF-Anwendungen. Das Hauptproblem bei den AlGaN/GaN-RTD stellen die Strominstabilitäten in diesen Strukturen dar. Im Gegensatz zur I-U-Charakterisierung der Doppelbarriere-Heterostrukturen zeigen unsere Kapazitäts-Messungen reproduzierbare Kennlinien im MHz-Frequenzbereich. Die beobachteten Eigenschaften der Kapazität-Spannungs-Charakteristiken zeigen eine starke Korrelation mit den geschätzten Resonanzparametern für die untersuchten Doppelbarriere-Strukturen. Eine Analyse der frequenzabhängigen Änderungen der Kapazität-Spannungs-Profile liefert zusätzliche Informationen über die Besonderheiten der Transporteigenschaften von RTD-Bauelementen bezüglich des Grenzflächenzustandes. Die Kapazitätsmessungen der Doppelbarrier-RTD sind daher eine leistungsfähige und empfindliche Methode zur Untersuchung der Transporteigenschaften und Strukturqualität. Die Ergebnisse dienen einer optimierten Konstruktion von AlGaN/GaN-RTD und einer effizienteren Analyse der Resonanztunnelprozesse sowie einer Verbesserung des Maximum-Minimum-Stromverhältnisses der NDW-Regionen.

Abstract

III-nitrides and especially gallium nitride based materials are attracting significant attention of researchers in the field of high-power and high-frequency electronics for future communication systems. Wide bandgap (for instance, GaN – 3.4 eV, AlN – 6.2 eV) allows these semiconductor materials to operate at much higher temperatures and at higher levels of ionizing radiation then conventional GaAs or Si. Higher drift velocity and critical electric field of III-nitrides materials allow high power output at high frequencies up to 1 THz. Introduction of RF amplifiers based on these materials will allow higher output power compatible with this of vacuum tube devices. Higher breakdown field of these materials will allow significant miniaturization of devices and optimization of power consumption. However despite above mentioned advances and benefits of III-nitride semiconductors, the commercial release of electronics based on them is delayed because of factors which limit the performance and reliability of III-nitride based devices are still under investigation.

This work is focused on comprehensive characterization of single-barrier and double-barrier AlGaN/GaN structures and analysis of transport phenomena in these structures. The objects of the work are high electron mobility transistors (HEMT) and resonant tunneling diodes (RTD) based on AlGaN/GaN heterostructures. In this work material and device technology have been developed. Different devices were fabricated for the investigation of transport properties of AlGaN/GaN heterostructures . A number of metallization schemes and annealing programs were tested for reliable ohmic contact formation. Several lithography masks were designed and developed in order to succeed in achieving the goals of the work. Some attention was given to experiment and test equipment automation, as a result of such efforts a program written on Delphi language was successfully used in measurements. The purpose of the program is to control measurement setup and acquire experimental data.

Historically the work was started with radiation hardness investigation of AlGaN/GaN HEMTs, in order to estimate the potential of III-nitrides for satellite applications. It appears that despite of significant degrade in device performance (in some cases devices show only 50% of their initial performance) at very high dose of gamma radiation ($2x10^9$ Rad), they are still operating (it should be noted that according to literature HEMTs based on GaAs are experiencing catastrophic failure at dose of gamma radiation as high as $6x10^8$ Rad). The most astonishing effect of gamma radiation has been found is the improvement of HEMT operational parameters and significant decrease in their dispersion over the wafer under low-doses (lower then 10^6 Rad). To get insight of this radiation stimulated improvement the various structural investigations (XRD, Auger) were carried out on test samples. It is revealed that the relaxation of mechanical stress in the structure and radiation stimulated structural and defect ordering are responsible for such improvement. Since than small dose gamma irradiation is used as required

step of device processing. Recently the significant improvement of low-temperature mobility and quantum life-time was observed after small dose of gamma irradiation.

The knowledge of fundamental parameters of materials and conditions which affect these parameters are important for DC and RF device performance analysis. The low-temperature magnetotransport measurements and temperature dependent characterizations are very sensitive tools for monitoring transport peculiarities in semiconductor structures. Effective mass, quantum life-time, sheet carrier concentration values were extracted for each sample under test. Comprehensive analysis of these data and technological parameters of state-of-the-art structures (layer thickness and composition) allowed establishing empirical dependence of effective mass on layer composition. Careful analysis of low-field magnetotransport of 2DEG in AlGaN/GaN heterostructure reveal peculiarities related to spin-orbit interaction in high density electron gas.

Another important issue on reliability of AlGaN/GaN HEMTs is self-heating during operation. The thermal budget problem was solved for conventional geometry of the transistor. The influence of substrate thermal conductivity and GaN buffer layer thickness on strength of overheating found to be critical.

The temperature dependent measurements of noise spectra of AlGaN/GaN HEMTs are important for RF performance estimation. Research of noise spectra allowed to define the specifics of noise sources from contacts, active and passive regions of HEMT. It was also revealed that by simple introduction of thin interlayer or cap in the device structure can significantly reduce noise level in AlGaN/GaN devices. These results can be used as guidelines for device structure optimization.

Resonant tunneling diodes are very promising for RF application. The main problem of AlGaN/GaN RTDs is current instabilities in these structures. In contrast to the I-V characterization of double-barrier heterostructures, our capacitance measurements demonstrate reproducible characteristics in MHz frequency ranges. The observed peculiarities in capacitance-voltage characteristics reveal a strong correlation with estimated resonance parameters for the investigated double-barrier structures. The analysis of frequency-dependent changes of capacitance-voltage profiles provides additional information on peculiarities in the transport properties of RTD devices related to an interface state. Thus, the capacitance measurements of double-barrier RTDs are a powerful and sensitive tool for the exploration of transport features and structural quality. The results can be used for designing AlGaN/GaN RTDs with optimized layout and a more efficient analysis of resonant tunneling processes and for improving the peak-to-valley ratio of NDR regions.

Content

Acronyms and Symbols 8

Introduction 9

Chapter 1. III-Nitride Semiconductor Heterostructures
- AlGaN/GaN Heterostructures 13
- Transport Effects and Noise Properties 15
- Reliability and Radiation Hardness 20
- Conclusions and Motivations 24

Chapter 2. AlGaN/GaN Heterostructures: Design and Processing 26

Chapter 3. Transport Phenomena of AlGaN/GaN Heterostructures in Magnetic Field
- Experimental Details and Theory 32
- Electron Effective Mass in AlGaN/GaN 2DEG 39
- Study of Spin-Orbit Interaction 45

Chapter 4. Reliability of AlGaN/GaN-based HEMTs
- Operational parameters of HEMT and TLM devices 50
- Noise Characteristics 53
  - Low-Frequency Noise 56
  - Middle Frequency Range Investigation 60
- Radiation Effect on Transport and Structural Properties of AlGaN/GaN heterostructures 69
- Study of Selfheating Effect in High-Power AlGaN/GaN-based HEMTs 72

Chapter 5. Transport of AlGaN/GaN-based RTD structures 78

Conclusions 83

References 86

Acknowledgement 97

Personal Publication List 98

Appendixes
- A. Photolithography Masks 100
- B. Properties of Digamma Function 104

Acronyms and Symbols

2DEG – two dimensional electron gas

HEMT – high electron mobility transistor

TLM patterns – transmission line model patterns

QW – quantum well

RTD – resonant-tunnelling diode

MOCVD – metal-organic chemical vapor deposition

MBE – molecular beam epitaxy

SOI – spin-orbit interaction

WAL – weak antilocalization

SdH oscillations – Shubnikov-de Haas oscillations

RF – radio frequency

I-V characteristics – current-voltage characteristics

C-V characteristics – capacitance-voltage characteristics

XRD – X-Ray diffraction

LL – Landau level

e – electron charge

k – Boltzmann constant

$\hbar$ - Plank constant

τ – transport lifetime

E_{Fi} - Fermi energy with respect to i^{th} subband

α_{SO} - Rashba constant

μ - electron mobility

μ_B - Bohr magnetron

Introduction

High-power device technology is a key technological factor for wireless communication, which is one of the information network infrastructures in the 21st century, as well as power electronics innovation, which contributes considerably to solving the energy saving problem in the future energy network. Wide-bandgap semiconductors, such as GaN and SiC, are promising for high-power and high-frequency device application owing to their unique properties. AlN, GaN, InN and their alloys are the most important compounds of the group-III nitrides. They crystallize in both wurtzite and zincblende polytypes. Wurtzite GaN, AlN and InN have direct room temperature bandgaps of 3.4, 6.2, and 0.65 eV, respectively. In cubic form, GaN and InN have direct bandgaps while AlN has indirect energy bandgap. GaN to be alloyed with AlN and InN makes available a wide range of energy bandgaps. The group-III nitrides thus formed span a continuous range of direct energy bandgap energies throughout much of the visible spectrum well into the ultraviolet wavelengths. This is one of the reasons filling the recent interest in GaN, AlN, InN, and their ternary alloys for short wavelength optoelectronic device applications.

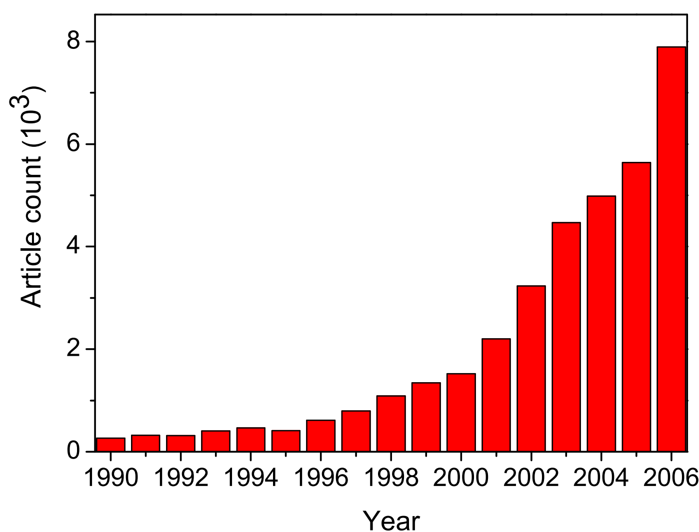

Figure I.1. Publication statistics in AlGaN/GaN heterostructures research field according to [4].

Despite decades of study, only recently GaN-based materials have moved from research laboratories to commercial markets. This change was due to a rapid progression of improvements in epitaxial growth, demonstration of p-type conductivity, and the fabrication of commercially viable devices [1-3]. The fabrication of highly efficient blue and green light emitting diodes and diode lasers is driving the development of gallium nitride technology, but the robust and versatile properties of gallium nitride make it an excellent candidate for high speed and high power electronics, cold cathode emitters, and solar blind ultraviolet light detectors.

Interest in gallium nitride has exploded in the past few years (see Fig. I.1), leading to an expansion of its potential applications on an almost monthly basis. This broad spectrum of applications has led some to predict that GaN will eventually become the third most important semiconductor system, behind GaAs and Si.

Table 1. Fundamental properties of Si, SiC, GaAs and GaN.

Property \ Material	Si	SiC	GaAs	GaN
Energy Gap (eV)	1.11	3.2	1.43	3.4
Breakdown E-Field (V/cm)	$6.0x10^5$	$3.5x10^6$	$6.5x10^5$	$3.5x10^6$
Saturation Velocity (cm/s)	$1.0x10^7$	$2.0x10^7$	$2.0x10^7$	$2.5x10^7$
Electron Mobility (cm^2/Vs)	1350	800	6000	1000
2DEG density* (cm^{-2})	-	-	10^{11}	10^{13}
2DEG mobility* (cm^2/Vs)	-	-	650	2000
Thermal Conductivity (W/cmK)	1.5	3.5	0.46	2.1

* two dimensional electron gas at the interface of AlGaN/GaN, or AlGaAs/GaAs heterostructures

Table 1 compares some fundamental properties of GaN, GaAs, SiC and Si. The most fundamental and significant difference is the energy bandgap. This parameter affects the intrinsic electronic properties of these semiconductors. With increasing of semiconductor bandgap the intrinsic concentration decreases and the intrinsic resistivity significantly increases. Wide bandgap ensures the high isolation, low parasitic and high temperature operation. In reality, it has not been possible to grow intrinsically pure GaN in a semi-insulating state because of a quite high background doping (typically 10^{16} cm^{-3}) due to residual defects concentration.

The electron mobility and saturation velocity are also important parameters, which indicate high-speed potential of the material. It should be noted that mobility depends on different factors, such as temperature, carrier and doping concentration etc (for two-dimensional electron gas system these factors also include composition and thickness of layers forming heterostructure). The values of mobility listed in the table 1 are taken at room temperature for top-quality materials. It is a fact that electron mobility in GaAs is significantly higher than that in

other semiconductors; this property is a major factor which allows the higher speed performance of bulk GaAs devices in comparison with other semiconductors. It should be noted, however, in the case of heterostructures the mobility and carrier concentration of 2DEG confined at the interface of AlGaN/GaN are much higher that those for AlGaAs/GaAs. Additionally, the thermal conductivity of GaN is almost a factor of five better than that of GaAs; this factor points at an inherited benefits of GaN crystals to move heat from device areas to the heat-sinking areas. Considering above mentioned advanced characteristics of AlGaN/GaN 2DEG and the values of breakdown field and thermal conductivity of GaN it is clear that AlGaN/GaN heterostructures are perfect for high-power and high-speed applications.

In the frame of this work, the fundamental transport properties of AlGaN/GaN heterostructures and devices have been investigated in order to find new approaches of device performance optimization for high-frequency applications. Special attention is given to factors which limit the performance of state-of-the-art devices at room, low and elevated temperatures, in radiation active environment or during long-term operation.

The work contains five major chapters.

The first chapter provides a scientific background to this work. It reviews present-day achievements in investigations of transport and noise properties of III-nitrides materials and devices.

The second chapter gives the detailed description of samples under investigation. Also it contains important information on device processing technologies, which have been used in this work: mask design, photolithography, etching, annealing and packaging.

In the third chapter the results of comprehensive investigation of low-temperature transport features in AlGaN/GaN heterostructures are described and discussed. The magnetoresistance is studied in low- and high-magnetic fields. The values of sheet carrier concentration, effective mass and quantum lifetime are extracted and analyzed for investigated samples from well resolved Shubnikov-de Haas oscillations. The effect of effective mass enhancement in 2DEG at AlGaN/GaN interface due to wave function hybridization is observed and analyzed. Phenomena related to spin-orbit coupling in the systems possessing both bulk inversion asymmetry and structural inversion asymmetry are studied. The strength of spin-orbit coupling is estimated using measurements of electric conductivity in low-magnetic field.

The fourth chapter provides important information on general reliability and gamma-ray radiation stimulated effects in AlGaN/GaN heterostructures and devices. The high potential of AlGaN/GaN-based devices for satellite communication systems is confirmed by strong resistance of transport characteristic of the device to high doses of gamma irradiation (up to 10^9

rad). The effect of improvement of transport properties of AlGaN/GaN HEMT structures under small-doses of gamma irradiation (10^6 rad) is revealed and analyzed. It should be noted that radiation-stimulated improvement of 2DEG mobility at low-temperatures is much higher than at room temperature (by factor of 2 and 1.01 at 0.3K and 300K, respectively). Spectral noise characteristics of the devices is studied and analyzed in different operational regimes and operational temperatures. It was found that the noise behaviour depends on several factors: layer structure design, processing technology, operating voltages, heating effects and quantum phenomena, variation of designed structure parameters with temperature, and radiation surrounding. The influence of these factors on the fundamental properties of AlGaN/GaN heterostructures were investigated and analyzed by monitoring of transport and noise characteristics. The radiation stimulated structural ordering is confirmed by XRD study of samples before and after irradiation. The effect of HEMT self-heating during work cycle is investigated. The calculation of temperature profiles the AlGaN/GaN TLM device has revealed the strong influence buffer layer on overheating of the structure. The obtained results are highly important for the design of an ultra low noise oscillators and sensors.

In the fifth chapter, the observed transport phenomena in AlGaN/GaN double heterostructure (double-barrier resonant tunneling structures) are analyzed. Since current-voltage characteristics of RTD demonstrate current instabilities and low repeatability resonant-tunneling conditions were investigated by capacitance voltage (C-V) characterization in wide frequency range of test signal. The C-V characteristics of a double-barrier RTD shows different behavior under forward and reverse polarities and a strong dependence on frequency. In order to analyze this dependence a self-consistent calculation of the potential profile of the structure was performed taking into account polarization effects at the AlN/GaN interfaces. The observed peculiarities are analyzed in the frame of possible charge trapping at the interface defect states.

The most important results of this work and perspectives for further works towards the development of high-power high-frequency devices are summarized in the conclusions.

CHAPTER 1. III-Nitride Semiconductor Heterostructures

This chapter briefly describes current status of AlGaN/GaN heterostructures researches, and provides general information concerning the most important transport phenomena and transport features observed in these structures.

AlGaN/GaN Heterostructures

Since the first AlGaN/GaN heterostructures and high electron mobility transistor (HEMT) devices were demonstrated the investigation of physical origin and properties of extremely high two-dimensional electron gas (2DEG) concentration in this system become one of the most important area in GaN research [1-3, 5-10]. It was found that high sheet carrier density of 2DEG can be formed at the AlGaN/GaN interface, without intentional doping of the structure. The polarization effects are the key factors determining the band structure and charge distribution in the AlGaN/GaN heterostructure [8]. The difference in spontaneous and piezoelectric polarization between AlGaN and GaN effectively results in a fixed sheet of polarization charge at the AlGaN/GaN interface, which brings high two-dimensional (2D) carrier density. This polarization charge is positive for structures grown on Ga-polar GaN, and serves to attract high concentrations of electrons. The origin of the 2D electrons at AlGaN/GaN is still under discussion, however, the most reasonable model to date, proposed by Ibbetson et al. [10], suggests that the electrons originate from donor-like states at the AlGaN surface (Fig. 1.1). It was shown that experimentally obtained carrier concentration of 2DEG is in a good agreement with one estimated with single surface donor model. In this model deep surface donor with energy of 1.65 eV below the conduction band-edge of AlGaN (with concentration about $1.1x10^{13}$ cm^{-2}) is actual source of electrons in the 2DEG.

Similarly, to the formation of a 2DEG at AlGaN/GaN interface, a two-dimensional hole gas (2DHG) can be formed at AlGaN/GaN interface with a negative polarization charge [11-13]. Such 2DHG is accumulated at the interface between AlGaN barrier grown on N-polar GaN, and in GaN/AlGaN structures grown on Ga-polar GaN. The formation of 2DHGs has been observed experimentally for Mg-doped GaN/AlGaN/GaN structures and AlGaN/GaN superlattices [14-16].

Taking into account above mentioned effect of free surface in AlGaN/GaN, it is clear that properties and performance of 2DEG are strongly affected by surface conditions, which can be monitored by measurements of characteristics of GaN-based devices (HEMTs, transmission line model (TLM) patterns, hall-bars etc).

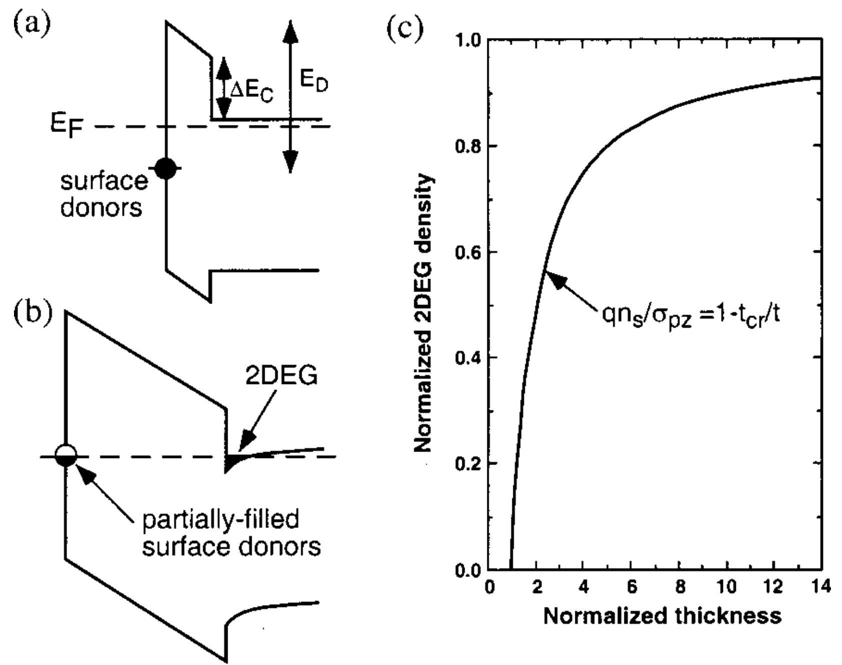

Figure 1.1. Schematic band diagram illustrating the surface donor model with the undoped AlGaN barrier thickness (a) less than, and (b) greater than the critical thickness for the formation of the 2DEG. Note the position of the Fermi level relative to the surface state in each case. (c) Calculated 2DEG density as a function of barrier thickness according to the surface donor model [10].

Another important structure is double-barrier heterostructure, which is a building block of resonant-tunnelling devices. Resonant tunnelling diodes (RTDs) are known to exhibit negative differential resistance (NDR) in current–voltage (I–V) characteristics. Typical RTDs are double-barrier structures in which a GaN quantum well (QW) is sandwiched between two thin AlGaN barriers.

AlGaN/GaN resonant-tunnelling diodes are intensively studied as one of next-generation quantum effect devices for high-speed (up to terahertz frequency range) electronics [17]. Until recently terahertz signals were an almost unexplored area of research due to the difficulties in generation and detection of electromagnetic fields at these wavelengths. Optical and microwave techniques can not be directly applied in the terahertz range investigation since optical wavelengths are too short and microwave wavelengths are too long compared to terahertz field wavelengths. It is expected that the development of reliable ultrafast RTDs based on GaN technology will boost the research in terahertz fields with many important applications. To develop a commercially useful RTD, peak-to-valley current ratios (PVCRs) of more than around 10 and current densities of more than the order of kA/cm^2 are required. To obtain the high current density, it is required to form highly doped emitter layers at both the sides of the double quantum well. However, heavy n-doping during the buffer growth results in a degradation in the

buffer surface crystallinity and the threading dislocations are easily generated and propagated to the surface [18]. Such degradation on growth stage could be responsible for observed low performance of present-day III-nitride RTDs.

Transport Effects and Noise Properties

Since the first days of AlGaN/GaN HEMT investigation scientific attention in GaN research area was attracted by effect of current drop in saturation region of HEMT output I-Vs. This effect is known in literature as ‘current collapse’ [19-22]. It is very important to understand what causes this drastic reduction in the current response, because it brings a serious limitation in the output power density and significant discrepancy between DC and RF performance of HEMT devices.

It is believed that the presence of surface states, associated with traps at the ungated region of surface, can cause observed current collapse [19-22]. Charging or discharging of these traps is modulating the depletion of the channel under the device surface. An extended depletion region can be formed by the exchange of charge between traps and conduction and/or valence bands, through the emission and/or recombination of electrons. Also, filling and emptying of traps would change the density of the surface charge in the semiconductor and influence the 2DEG sheet concentration. This parasitic effect is very common in GaN FETs and it is very important to include it in physical models, fitting more exactly the operation of a real device.

The similar change in I-V behaviour of AlGaN/GaN HEMTs can be caused by changes in carriers mobility due to channel overheating [23-25]. The problem of self-heating in AlGaN/GaN is very crucial because of GaN high-power applications, and originates from use of low thermal conductance sapphire as a substrate of choice in GaN heteroepitaxy. It was shown that Joule self-heating effect and effect of high electric field can lead to current saturation or negative differential resistance regimes even in ungated AlGaN/GaN devices, such TLM resistances [23]. The proposed theoretical model is in a good agreement with experimentally observed data, it is based on heat dissipation and heat-transfer modelling in the device and self-consistent solution of coupled nonlinear equations for the channel current and the channel temperature. The model allows one to discriminate between the current reduction due to hot-electron effect and channel temperature rise caused by the self-heating. The obtained results allow to suggest that to utilize unique properties of group III-nitride heterostructures, including high-speed channel electrons, it is necessary to further optimize the thermal budget of devices. Such optimization can be

achieved by choosing a thinner sapphire substrate or other substrate materials (SiC or Si), a shorter conducting channel, as well as short-time operating regimes [26].

It is clear from discussion above, that carrier concentration and carrier mobility are two of the most important parameters, which define HEMT device capabilities and performance. The knowledge of factors and effects, which have direct impact on concentration and mobility, are required for superior device design and fabrication.

Because of the lack of suitable bulk substrates for GaN homoepitaxy, heteroepitaxial growth of GaN mostly relies on the nucleation and buffer layers on lattice mismatched Al_2O_3 or SiC substrates. Large lattice mismatch ~2.5% GaN/AlN, ~3.4% in the GaN/SiC and ~11% in GaN/Al_2O_3 systems produce the mechanical strain in these systems. It should be noted, that the hexagonal 4H- and 6H-SiC or Si offer a significant advantage over sapphire, including a high thermal conductivity and smaller lattice mismatch with GaN. Over the past decade, AlN buffer layers have been routinely used to achieve high quality GaN layers on SiC or Al_2O_3 owing to the low in-plane lattice mismatch. AlN buffers compensate tensile strain for subsequent high-temperature growth of GaN film and result in highly compressive GaN layers. The compressive strain in the epilayer is partially relaxed during growth through misfit dislocations at the interface. The dislocation density in GaN grown on sapphire is quite high in the range 10^6–10^9 cm^{-2} [2]. Also it should be noted that the relaxation of the tensile strain results in cracks and the anisotropic strain gradient along the surface, which strongly affect device performance.

The formation of a two dimensional electron gas at the AlGaN/GaN heterointerface depends on spontaneous and piezoelectric polarization field. It should be emphasized here that 2DEG density is very sensitive to any change in stress field of the structure because this built-in strain is responsible for generation of piezoelectric field [8-14]. Such high sensitivity to stress variation enables AlGaN/GaN heterostructures to cover important segment of pressure sensors [27].

It is obvious that in AlGaN/GaN system the degree of lattice mismatch depends on Al mole fraction of AlGaN layer. The change in Al content of AlGaN layer allows not only 'strain engineering' but even more important 'bandgap engineering': bandgap of AlGaN film can be controlled by its Al content. The heterostructures we have consist of at least two semiconductor layers with different bandgaps. The difference in electron energy spectrum between wide bandgap semiconductor and narrow bandgap semiconductor results in the offsets in the conduction and valence bands of heterostructure constituents at the heterointerface. A number of theoretical and experimental works is devoted to study of band offsets problem in strained AlGaN/GaN structures [28-35], but no reliable data have been obtained, because of quite large

discrepancy in results by different research groups. To estimate the conduction and valence band offsets in AlGaN/GaN heterostructure the semi-empirical formulas are usually used [28]:

$$\mathbf{\Delta E_V(x) = 0.3x}, \quad (1.3.1)$$

$$\mathbf{\Delta E_C(x) = 1.41x+x^2}, \quad (1.3.2)$$

where x is the Al mole fraction of AlGaN layer.

The band offsets in conduction band (E_c) and valance band (E_v) at heterointerface influence the carrier transport and the carrier confinement, as well as the performance and reliability of devices. Control of band offsets with Al mole fraction of wide bandgap regions may lead to a new perspectives in the design of group III-nitride heterostructure devices for high-temperature and high-pressure device applications. Usually the macroscopic effects at the interface are the change in the bandgap energy, effective mass, intrinsic carrier density, and dielectric constant. Therefore, quantitatively precise and reliable determination of band offsets, effective mass, intrinsic carrier density, and dielectric constant is desirable for the comprehensive analysis of transport effects and properties of AlGaN/GaN based heterostructures.

The two-dimensional electron gas can be characterized by electron effective mass, which incorporates information not only about the electronic bands at the interface but also about many-body effects. It is known that the magnetoresistive effect measured at low-temperatures gives important information about the band structure of semiconductors and about the character of the scattering of mobile charge carriers. Measurements of the Hall effect and Shubnikov-de Haas oscillations permits the evaluation of a number of AlGaN/GaN transport properties [36-54], such as, 2DEG concentration, mobility, quantum and transport lifetimes and

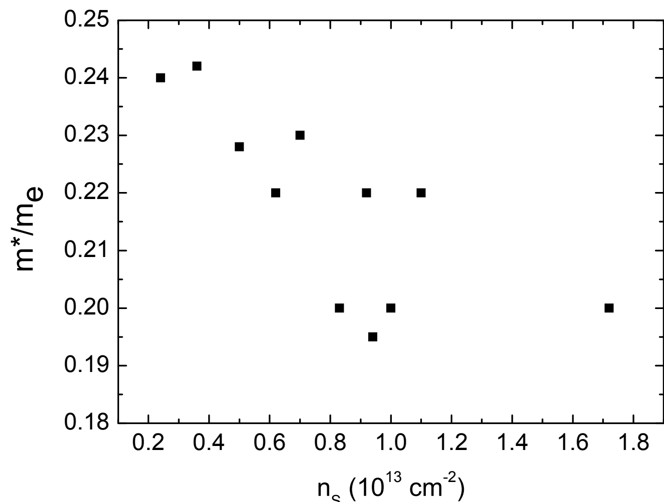

Figure 1.2. Experimental values of the effective mass measured for different 2DEG density [36-41].

effective mass of carriers in 2DEG system. The in-plane effective masses measured for AlGaN/GaN 2DEG systems by different research groups show large scattering of the data (see Fig. 1.2).

This scattering is not surprising because it simply reflects the variation of band structure caused by the polarization charges at the interface, residual doping, the structure design, alloy disorder degree in the barrier, interface roughness etc. All this could obviously be quite different for different samples grown in different growth environments. The mass enhancement in 2DEGs should be easily understood if the effective mass used in the calculation of the various transport properties of such structures is often approximated by the corresponding value for bulk material. However, this assumption becomes less valid with increase of Fermi energy. It is known, for instance, that the in-plane effective masses are expected to exceed the bulk values considerably due to the increasing effect of band nonparabolicity at higher Fermi energy. At the same time a large scattering of the data is not well understood and attempts have to be made in resolving the origins of such scattering. It has been pointed out that this discrepancy can be attributed to the effect of the wave-function penetration into the barrier. However, there is still no clear evidence to demonstrate the penetration effect.

The improvement of performances in modern AlGaN/GaN power devices requires the investigation and identification of parasitic scattering mechanisms that are likely responsible for the lack of reliability frequently observed up to now. One of the most efficient ways to identify these scattering mechanisms is the study of scattering lifetimes versus carrier density in the 2DEG. In the study of the transport properties of the two-dimensional electron gas it has long been recognized that two distinct relaxation times can be defined [55]. The most commonly encountered is the transport lifetime defined as

$$\tau = \mu m^*/e, \tag{1.3.3}$$

where μ is the low-field Hall mobility, m^* is the effective mass of the charge carrier, and e is the electronic charge.

Another relaxation time is the quantum scattering time τ_q, which is a measure of the time that an electron remains in a single momentum eigenstate in the presence of scattering. The transport and the quantum lifetimes will be substantially different for large and small angle scattering processes. Consequently, the ratio of the two scattering times τ/τ_q has traditionally been used in the study of semiconductor transport to discriminate between various scattering mechanisms and to measure the degree to which carrier scattering is predominantly large or

small angle. Experimentally obtained lifetime ratios for 2DEG AlGaN/GaN system are varied from 1 to 30 [40, 41, 43, 49-51]. The proper analysis of the quantum scattering time and the degree to which scattering is predominately large or small angle still remains controversial [56-59].

The quantum oscillations are highly sensitive to the fine structure of the energy spectrum of carriers, so that even small spin splitting, small as compared to the Fermi energy but commensurable with the energy distance between Landau levels, qualitatively modifies the oscillation behavior. In a magnetic field, the spin splitting at the Fermi surface gives rise to the oscillations with close frequencies, i.e. to beats [60-64]. Such a behavior was observed and attributed to the zero-field spin splitting in 2D electron gas at AlGaN/GaN heterointerface. Spin-dependent transport phenomena in two-dimensional electron systems are of broad interest at present time. Spin-orbit interaction governs the wide class of spin phenomena. Among them are spin relaxation, spin transport controlled with an external electric field by the Rashba effect, circular photogalvanic and spin-galvanic effects, electric current-induced spin orientation and precession, intrinsic spin Hall effect, etc.

Recently, the low-temperature magnetoconductivity measurements of high mobility 2DEGs confined in the wide bandgap AlGaN/GaN system show non-monotonic behavior in the magnetoconductivity with a pronounced weak localization/antilocalization effects [41, 65-67]. Anomalous magnetoresistance caused by weak localization/antilocalization is a powerful tool for extracting kinetic and band structure parameters of 2DEG systems. Antilocalization effect in AlGaN/GaN 2DEG system is indicating the presence of significant spin-orbit coupling. It should be noted that the magnetic field at which the magnetoconductivity minimum occurs does not depend sensitively on electron density. Latter indicates that the Bychkov-Rashba mechanism [68] is the dominant spin-orbit coupling in AlGaN/GaN 2DEG systems. The extracted Rashba coupling constant α_{so} are ranging from 0.6 to 8.1 x10^{-12} eVm [41, 48, 67]. It is believed that extremely high build-in electric field at the AlGaN/GaN interface is responsible for strong enhancement of Rashba constant in 2DEG AlGaN/GaN systems. Further extensive investigation of spin-orbit coupling will allow one to estimate the III-nitride potential for spintronic applications.

Reliability and Radiation Hardness

Above mentioned achievements in the investigation of transport properties of III-nitrides, are the basis for development of new high-performance devices with superior functionality. However, till now III-nitride based devices show quite low reproducibility and fabrication yield. Reliability analysis and detailed knowledge of the device properties and characteristics and their dependence on environment conditions are necessary in order to determine the suitability of the selected component for the application and improvement of fabrication yield. These issues are of particular importance for the application of III-nitride devices in high reliability systems due to the need for the utilization of large numbers of these devices at the upper limit of their performance. In order to realize nitride device potential, it is required to understand not only the transport properties and capabilities of AlGaN/GaN based devices but also the failure mechanisms, factors responsible for defect formation and compensation.

It is known, that native point defects control many aspects of semiconductor behavior. Such defects can be electrically charged, both in the bulk and on the surface. This charging can affect numerous properties such as structure, thermal diffusion rates, as well as electronic properties of device structures such as leakage currents, trapping and recombination rates for electrons and holes etc.

One of the most effective technique of traps dynamic monitoring in electronic devices is noise measurements [69]. Low-frequency noise measurements are a powerful tool for study impurity and defects in semiconductor structures [70] and to diagnose quality and reliability of semiconductor devices [71,72]. Noise in electronic devices arises mainly from the capture and subsequent emission of charge carriers at discrete trap levels. Simple analysis of charge trapping of the carriers in the $Al_xGa_{1-x}N$ layer shows that the number of traps in GaN-based devices is higher than in GaAs based devices, and the traps are deeper than for GaAs [73]. Despite the existence of many of low frequency noise reports on III-Nitride materials and electronic devices, there is considerable discrepancy between the reported noise levels and trap energies. Hooge factors in the range of $8x10^{-5}$ to $5x10^{-2}$ for AlGaN/GaN based devices, have been reported in the literature [69-72, 74-77]. It is well known that low-frequency noise in semiconductor devices is a performance limiting factor in radio frequency (RF) circuits. Therefore its understanding, modelling, control and suppression are key points to the design of reliable RF products with improved performance.

For emerging signal-processing applications, the properties of noise characteristics play a critical role. The investigation of fluctuation phenomena of the HEMT structure in a wide range

of applied electrical fields is an important issue because its noise is up-converted to the high-frequency noise in the oscillator circuit [78], and especially the MHz frequency range plays a crucial role. This frequency region (where 1/f noise decreases to the level of white noise) is an intermediate one. The lower the level of noise in this region the lower and the narrower is up-converted high-frequency band noise. Noise reduction in this region will allow to increase the density and rate of transmitted information in communication systems. Additional noise reduction and increasing stability and reliability are expected after characterization of trap centers, control of the traps-related effects and the structure passivation. Investigations of low-frequency fluctuations have proven to be useful for studying “slow” fluctuations at low electric fields (*E*), while more important for various applications is the study of intermediate -frequency and high-frequency range fluctuations with increasing *E* and “fast” process phenomena (where hot electron effects, energy and impulse relaxation mechanisms become essential) is more important for various applications. The optimal value of the minimum noise in field effect transistors (FETs) is usually obtained with a relatively low drain and gate voltage [79] while high operating voltages are desirable for power applications. One of the reasons of high -frequency noise in FETs proposed in [80] is a hot carriers noise. In this case, the carrier lifetime and the noise level of the device are determined by interface states, introduced by hot carriers. The authors found that the presence of interface states decreases the channel conductance and high-frequency thermal current noise, and at the same time increases the induced gate current noise.

Detailed analysis by Pantisano and Cheng [81] of the FET high-frequency noise (1-2.5 GHz) as a function of degradation induced by electrical stress allows them to conclude that the physical origin of FET noise differs from that following from the usually accepted physical models of thermal noise, and is due to previously unaccounted flicker noise at microwave (MW) frequencies. The FET MW noise study, revealed a defect-related (flicker) origin of the noise in the FET. It was demonstrated that in order to contribute to the high-frequency noise, the traps must be very close to the interface. In this case, tunneling can be very efficient and the minimum time constant for the charge exchange must be much shorter than the 10 ns. Therefore, the authors provide evidence that the high-frequency noise of the FET should not be thermal.

Large gate leakage current and current dispersion due to GaN surface states remain the major obstacles for further improvement in these devices. Recently, effective gate leakage suppression has been realized by surface passivation technique. Passivation of HEMT involves covering the device surface between source, gate and drain electrodes with a dielectric layer. Si_3N_4, SiO_2, Al_2O_3, GaN, AlN and Sc_2O_3 have been used as the surface passivation layer and/or the gate insulator for AlGaN/GaN HEMTs [82–89]. Passivated HEMTs has exhibited

improvement in device characteristics relative to the regular unpassivated HEMTs. An increase not only in carrier concentration but also in mobility of the 2DEG in AlGaN/GaN heterostructures was observed. Surface passivation using silicon nitride has been found to reduce current slump and microwave power degradation of intentionally undoped AlGaN/GaN HEMTs [90]. Such improvements are believed a result of long term suppression of surface traps.

Although, extensive studies have shown that surface passivation using silicon nitride can suppress the current collapse and microwave power degradation, the exact passivation mechanism is not yet well understood. Since the origins of passivation effect are questionable, a further investigation of these phenomena and their physical origins will be required to choose better dielectrics and design in order to optimize the performances of AlGaN/GaN HEMTs. However, recent reports claimed that tensile stress produced by silicon nitride passivation dielectric is a significant factor that resulted in those improvements [91]. On the contrary [92] the additional strain could form a non-uniform polarization induced charges and deteriorate device performance significantly. Furthermore, this excess strain can locally relax the film eliminating the piezoelectric induced charge or to forming defects that act as electron traps.

The understanding of trapping mechanism and defect origins is even more required in development of reliable double and multi-barrier structures based on AlGaN. These structures suppose to be sources of RF and terahertz fields in future high-speed electronics. Demonstration of a vertical RTD, whose current-voltage characteristics has persistent region of negative differential resistance at least roughly, has not been achieved so far in the AlGaN system. I-V characteristics that include resonant tunnelling effects have been published up to now by the groups of Kikuchi et al. [93] and Foxon et al. [94, 95] Controversial discussion [96,97] was led about the published results partly due to irreproducibility of the published data. However, these I-V characteristics exhibit

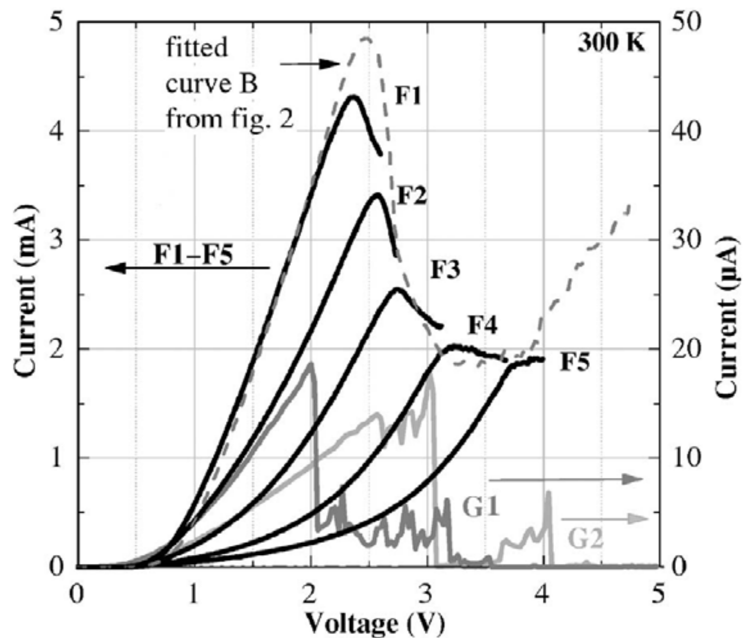

Figure 1.3. Room temperature subsequent traces of RTD I-V characteristics, black and gray corresponds to devices from different parts of wafer. The dashed curve corresponds to single trace until catastrophic failure of the device [98].

clear negative differential resistance, which is the signature of any resonant tunnelling. Recently, quite weak NDR was observed in I-V characteristics of GaN RTD [98] (see Fig. 1.3), despite of using native GaN substrate. In most of the studies abrupt change in the I-V curve has been observed after the first trace on the subsequent retrace or any further trace. After a few subsequent measurements only the exponential background remains in I-V characteristics of GaN RTD. Accordingly to Ref. 98, after every trace of I-Vs the resonance peak is shifted to higher voltages. The envelope of the traces coincides with what would have been observed in a single complete trace, but no strong conclusion on this observation has been made. It is believed that low reliability and performance are partially caused by trapping effects in the structure. The letter indicates the necessity for comprehensive investigation of traps origins, their influence on transport properties of devices and development of methods, which will allow control or suppression of traps and trapping processes.

Some of these methods are well known and widely used in state-of-the-art semiconductor devices technology cycle. These include a variety of active treatments such as conventional rapid thermal annealing [99], and advanced: laser, microwave or radiation treatments [101-102]. Considerable interest to study of the mechanisms of ionizing radiation effect on III-nitride materials and structures is generated mainly by the following two factors. One of them is the investigation of radiation hardness of GaN-based devices and the possibility to improve its degradation resistance for different applications including satellite communication systems. Another factor is the possibility to control over the properties and performance of III-nitride based devices and structures with small doses of radiation.

For applications involving significant radiation exposure, such as in aerospace, medicine, military, and nuclear applications, the study of high-energy irradiation effects on device performance is essential to assess long-term device reliability and develop radiation tolerant circuits and systems. Exposure of GaN semiconducting films to energetic particle irradiation invariably results in the introduction of vacancy and interstitial point-defects by displacement of N and Ga species from their respective sublattices. However, the isolated character of these defects may be modified by thermally activated defect migration and interactions with native defects even at temperatures near 300 K. The evolution from isolated point defects, as initially introduced by irradiation at cryogenic temperatures, to more complex defect structures has been clearly evidenced by electron paramagnetic resonance studies of electron-irradiated GaN films [103,104]. Similar to other semiconductor materials, the introduction of radiation-induced defects in GaN films results in the creation of levels in the forbidden energy gap that may act as scattering centers and as either donors, acceptors, traps, or recombination centers, thereby

affecting the electronic and optical material properties and, consequently, semiconductor device performance [105-109]. At sufficiently high concentrations, radiation-induced defects have been shown to result in degradation of carrier mobility and changes in free carrier concentration, which vary with the material doping level, an indication that irradiation-induced point defects may interact with impurities as well as native defects [110,111]. The relatively high irradiation doses employed in most published studies of GaN, which have been necessary in order to induce sufficiently high defect concentrations, indicate low defect production rates and high energy thresholds for displacement damage. Such studies confirm the potential of GaN-related materials and devices to be used in circuit and system applications requiring radiation-hardness. Low susceptibility of bulk material to radiation damage allows to develop radiation-hard devices. The radiation tolerance of electronic devices and circuits is usually limited by radiation-induced effects associated with electrical contacts, surfaces and interfaces, and the presence of extended defects such as dislocations [112]. But the most important effect of small doses ionizing radiation (in particular gamma radiation) on GaN-based electronics is discovered only recently [113]. It was shown that parameters of HEMT devices can be improved and fabrication yield can be increased by implementing irradiation procedures with optimal exposure dose on device processing stage.

Conclusions and motivation

A comprehensive up-to-date overview on transport properties of AlGaN/GaN heterostructures is presented.

The technology developed during commercialization of GaN photonic devices has resulted in great respect in remarkable progress in GaN-based electronics over the past 10 years.

GaN-based electronics show significant advances in microwave power performance over structures based on conventional semiconductors. This wide bandgap material system will play a major role in future telecommunication technologies. Furthermore, with improved understanding of the material and device physics, additional advantages in active device performance and expanded wide bandgap device functionally are realized. The understanding of transport properties of AlGaN/GaN interfaces and devices, which utilize these interfaces properties, is crucial in design and development of RF device and circuits with superior characteristics.

Despite a huge number of research groups working on investigation of transport phenomena in GaN-based devices there are many open questions in this field.

Therefore motivation for the PhD work is theoretical and experimental investigation of the effects, which influence transport properties of AlGaN/GaN structure such effective mass, lifetimes, device performance, and factors, which limit the performance and reliability of AlGaN-based devices including radiation stimulated effects.

The accomplishment of this task requires the following:

- device processing, i.e. fabrication of transmission line patterns, hall-bars, high electron mobility transistors, resonant tunnelling diodes;
- measurements of DC, pulse characteristics of the devices;
- research on DC characterisation and frequency dependent characteristics of devices (. capacitance-voltage and noise characterization)
- comprehensive investigation of transport phenomena in test structures in magnetic field;
- investigation of radiation hardness of devices and structures;
- investigation of structural properties with X-ray diffraction, Auger spectroscopy etc.

Chapter 2. AlGaN/GaN Heterostructures: Design and Processing

This chapter provides important information about device fabrication techniques used in this work, and description of investigated AlGaN/GaN wafers. Single barrier structures were grown by MOCVD on Sapphire and SiC substrates, with different layer composition. The investigated structures were supplied by Forschungszentrum Juelich Epitaxy Growth team (Germany), and partners in Cornell University (USA), Nottingham University (UK) and Center of Heteroepitaxy Research and Application (France). TLM patterns, HEMT and RTD devices were designed and processed on the wafers using photolithography masks produced in this work.

The processing of the wafers starts from photolithography [116]. Photolithography is the process of transferring patterns of geometric shapes on a mask to a thin layer of photosensitive material (called photoresist) covering the surface of a semiconductor wafer. Photoresist is a radiation-sensitive compound that can be classified as positive or negative, depending on how they respond to radiation. For positive resists, the exposed regions become more soluble and thus more easily removed in the development process. The result is that the patterns formed in the positive resist are the same as those on the mask. Prior to exposure, the photosensitive compound is insoluble in the developer solution. After exposure, the photosensitive compound absorbs radiation in the exposed pattern areas, changes its chemical structure, and becomes soluble in the developer solution. After development, the exposed areas are removed. With negative resists, exposed regions become less soluble, and the patterns formed in the negative resist are the reverse of the mask patterns. After development, the unexposed areas are removed. One major drawback of a negative photoresist is that in the development process, the whole resist mass swells by absorbing developer solvent. This swelling action limits the resolution of negative photoresists.

Figure 2.1 (a) shows a typical exposure response curve and image cross section for a positive resist. The response curve describes the percentage of resist remaining after exposure and development versus the exposure energy. As the exposure energy increases, the solubility gradually increases until at a threshold energy E_T , the resist becomes completely soluble. The sensitivity of a positive resist is defined as the energy required to produce complete solubility in the exposed region. Thus, E_T corresponds to the sensitivity.

The image cross section in Fig. 2.1 (a) illustrates the relationship between the edges of a photomask image and the corresponding edges of the resist images after development. The edges of the resist image are generally not at the vertically projected positions of the mask edges because of diffraction. The edge of the resist image corresponds to the position where the total

absorbed optical energy equals the threshold energy E_T. Fig. 2.1 (b) shows the exposure response curve and image cross section for a negative resist. The sensitivity of a negative resist is defined as the energy required to retain 50% of the original resist film thickness in the exposed region.

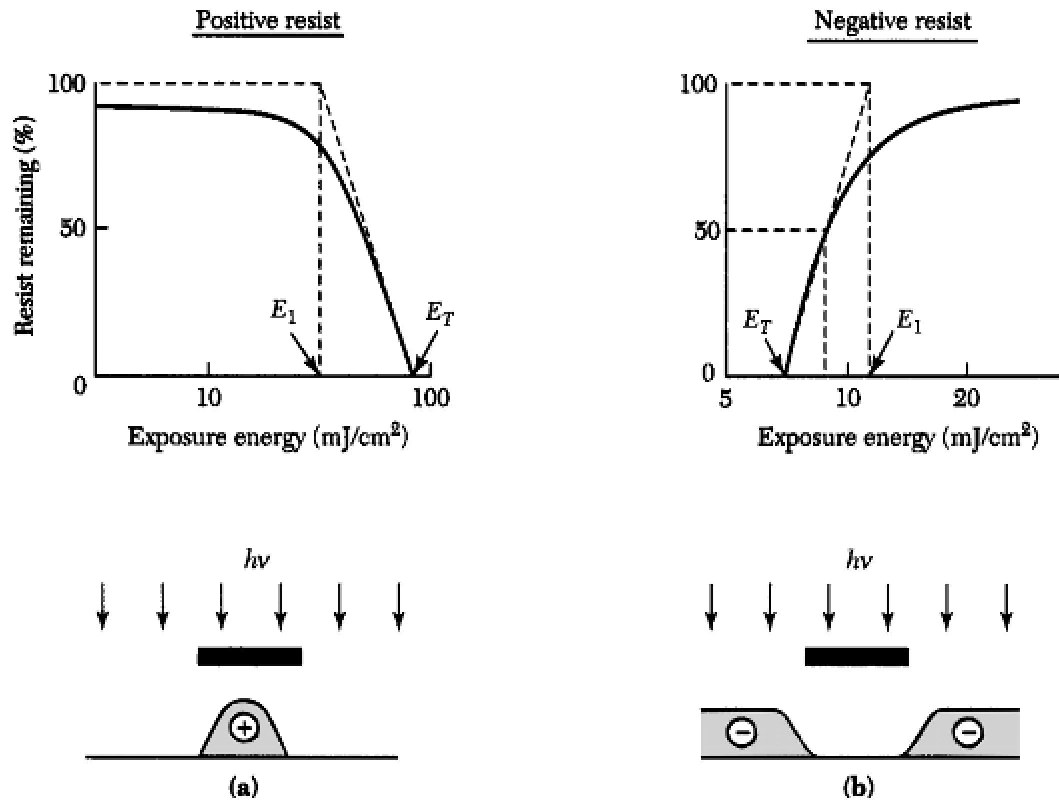

Figure 2.1. Exposure response curve and cross section of resist image after development for (a) positive photoresist and (b) negative photoresist [116].

Patterns on the mask define the various regions in an integrated circuit, such as the implantation regions, the contact windows, and the bonding pad areas. Photolithography requires a clean processing room. The need for a clean room arises because dust particles in the air can settle on semiconductor wafers or lithographic masks and cause defects that result in circuit failure. For example, a dust particle on a semiconductor surface can disrupt the growth of an epitaxial film, causing the formation of dislocations. A dust particle incorporated into a gate oxide can result in enhanced conductivity and cause device failure due to low breakdown voltage. The situation is even more critical in photolithography. When dust particles adhere to the surface of a photomask, they behave as opaque patterns on the mask, and these patterns will be transferred to the underlying layer along with the circuit patterns on the mask. This may result in the formation of a pinhole in the underlying layer or can lead to a short circuit between the two conducting regions and render the circuit useless. In a cleanroom, the total number of dust particles per unit volume must be tightly controlled along with the temperature and humidity. There are two systems to define the classes of cleanroom. For the English system, the numerical

designation of the class is taken from the maximum allowed number of particles 0.5 μm and larger per cubic foot of air. For the metric system, the class is taken from the logarithm (base 10) of the maximum allowed number of particles 0.5 μm and larger, per cubic meter. For example, a class 100 cleanroom (English system) has a dust count of 100 particles/ft^3 with particle diameters of 0.5 μm and larger, whereas a class M 3.5 cleanroom (metric system) has a dust count of $10^{3.5}$ or about 3500 particles/m^3 with particle diameters of 0.5 μm or larger. Since the number of dust particles increases as particle size decreases, more stringent control of the cleanroom environment is required as the minimum feature lengths of ICs are reduced. For most IC fabrication areas, a class 100 cleanroom is required; that is, the dust count must be about four orders of magnitude lower than that of ordinary room air. However, for photolithography, a class 10 cleanroom or one with a lower dust count is required.

The pattern transfer process is accomplished by using a lithographic exposure tool. The performance of an exposure tool is determined by resolution and registration. Resolution is the minimum feature dimension that can be transferred with high fidelity to a resist film on a semiconductor wafer. Registration is a measure of how accurately patterns on successive masks can be aligned (or overlaid) with respect to previously defined patterns on the wafer. There are two primary optical exposure methods: shadow printing and projection printing. Shadow printing may have the mask and wafer in direct contact with one another (as in contact printing), or in close proximity (as in proximity printing). Fig. 2.2 (a) shows a basic setup for contact printing where a resist-coated wafer is brought into physical contact with a mask, and the resist is exposed by a nearly collimated beam of ultraviolet light through the back of the mask for a fixed time. The intimate contact between the resist and mask provides a resolution of ~1 μm. However, contact printing suffers from one major drawback—a dust particle on the wafer can be embedded into the mask when the mask makes contact with the wafer. The embedded particle causes permanent damage to the mask and results in defects in the wafer with each succeeding exposure. To minimize mask damage, the proximity exposure method is used. Fig. 2.2 (b) shows the basic setup, which is similar to contact printing except that there is a small gap (10–50 μm) between the wafer and the mask during exposure. The small gap, however, results in optical diffraction at feature edges on the photomask; that is, when light passes by the edges of an opaque mask feature, fringes are formed and some light penetrates into the shadow region. As a result, resolution is degraded to the 2–5-μm range. In shadow printing, the minimum linewidth, or critical dimension (CD), that can be printed is approximately

$$CD \cong \sqrt{\lambda g} \tag{2.1.1}$$

where λ is the wavelength of the exposure radiation and g is the gap between the mask and the wafer and includes the thickness of the resist. For $\lambda = 0.25$ μm and $g = 50$ μm, the CD is 3.5 μm. Thus, there is an advantage in reducing both λ and g to get lower CD. However, for a given distance g, any dust particle with a diameter larger than g potentially can cause mask damage. To avoid the mask damage problem associated with shadow printing, projection printing tools have been developed to project an image of the mask patterns onto a resist-coated wafer many centimeters away from the mask [116].

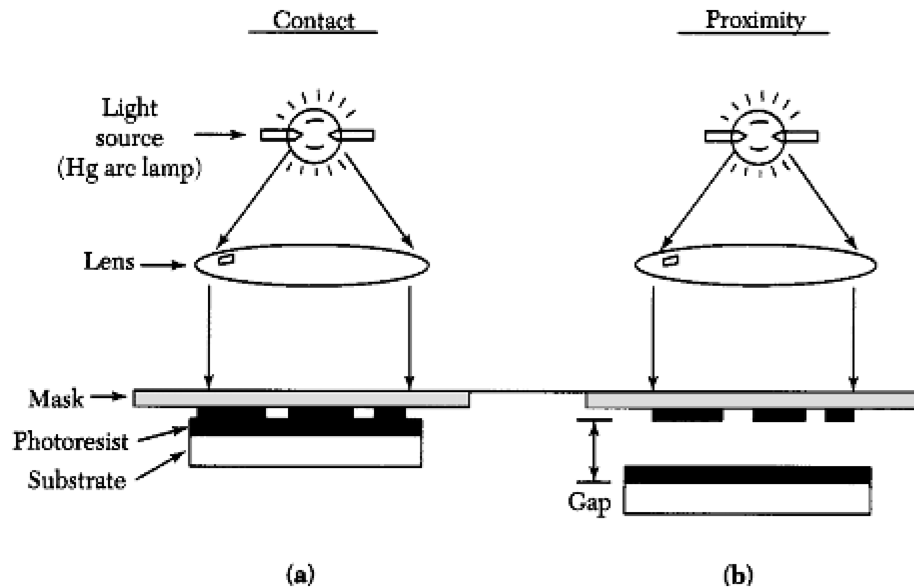

Figure 2.2. Optical shadow printing techniques: (a) contact printing;(b) proximity printing [116].

The first step in maskmaking is to use a computer-aided design (CAD) system in which designers can completely describe the circuit patterns electrically. The digital data produced by the CAD system then drive a pattern generator, which is an electron-beam lithographic system that transfers the patterns directly to electron-sensitized mask. The mask consists of a fused silica substrate covered with a chrominum layer. The circuit pattern is first transferred to the electron-sensitized layer (electron resist), which is transferred once more into the underlying chrominum layer for the finished mask.

Another important step of device processing is deposition of metallization for device formation. The most common methods of physical vapor deposition (PVD) of metals are evaporation, electron-beam evaporation, plasma spray deposition, and sputtering [116]. Metals and metal compounds can be deposited by PVD. Evaporation occurs when a source material is heated above its melting point in an evacuated chamber. The evaporated atoms then travel at high velocity in straight-line trajectories. The source can be melted by resistance heating, by radio frequency (RF) heating, or with a focused electron beam (or e-beam). Evaporation and e-beam evaporation were used extensively in earlier generations of integrated circuits, but they

have been replaced by sputtering for modern integrated circuits (ICs). In ion-beam sputtering, a source of ions is accelerated toward the target and impinges on its surface. The sputtered material deposits on a wafer that is placed facing the target. The ion current and energy can be independently adjusted. Since the target and wafer are placed in a chamber that has lower pressure, more target material and less contamination are transferred to the wafer. One method to increase the deposition rate in sputtering is to use a third electrode that provides more electrons for ionization. Another method is to use a magnetic field to capture and spiral electrons, increasing their ionizing efficiency in the vicinity of the sputtering target. This technique, referred to as magnetron sputtering, has found widespread applications for the deposition of aluminium and its alloys at a rate that can approach 1 μm/min.

Formation of the device requires not only metal deposition but also shaping of the wafer, by removing its material trough resist patterns with etching techniques. The most wide spread etches are wet etching, dry etching (this includes plasma assisted etching and reactive ion etching), and ion beam etching. First two rely on chemical reaction between wafer material and etching solution (the solution is supplied to the surface, reacts with material, the products of reaction are removed). The latter one is almost mechanical shaping, by bombardment of wafer surface with fast Ar ions.

After device formation wafers are cut into pieces, which fit package dimensions. In research fabrication, circuits or devices usually bonded to a package with wires. The ultrasonic bonding is the most effective technique of wire bonding. In this approach the aluminium wire is fed from the spool through a hole in a bonding needle, which is lowered then into position as an ultrasonic vibration at 20-60 kHz causes the metal to deform and flow (even at room temperature). The needle is raised after the bond to the package is formed, a clamp pulls and brakes the wire.

In order to accomplish this PhD work 4 lithography masks were designed (see Appendix A). Processing of single and double heterostructures has required at least two steps of photolithography (one – for electric contacts metallization deposition, another – for mesa formation).

All investigated single barrier structures were grown by metalorganic chemical vapor deposition using three different types of reactors [117-119]. Single barrier structures were grown on Sapphire and SiC substrates, with different layer composition (Fig. 2.3 (a)-(e)). Double barrier structures AlN/GaN/AlN (see. Fig. 2.4) were grown on 5 micrometer thick undoped MOCVD-GaN templates on Sapphire substrate by molecular beam epitaxy [117].

Usual size of wafer in single lithography step was 10x10 mm^2. Device mesas etching was performed with use of ion-beam etch with Oxford IBE unit. Mesa height was about 300 nm for single barrier structures and 800 nm for double barrier structures.

Electrical ohmic contacts were formed by magnetron sputtering of Ti/Al/Ni/Au-35nm/200nm/45nm/100nm metal components with subsequent RTA for 40 seconds at 900 ^{o}C. Formation of ohmic contacts to highly doped regions of double-barrier structures did not require annealing. The smallest feature size obtained is 2 μm.

The wafers were diced into smaller pieces 2.5x2.5 mm^2 for subsequent packaging and ultrasound bonding by "Kulicke & SoFFA" manual bonder 4123.

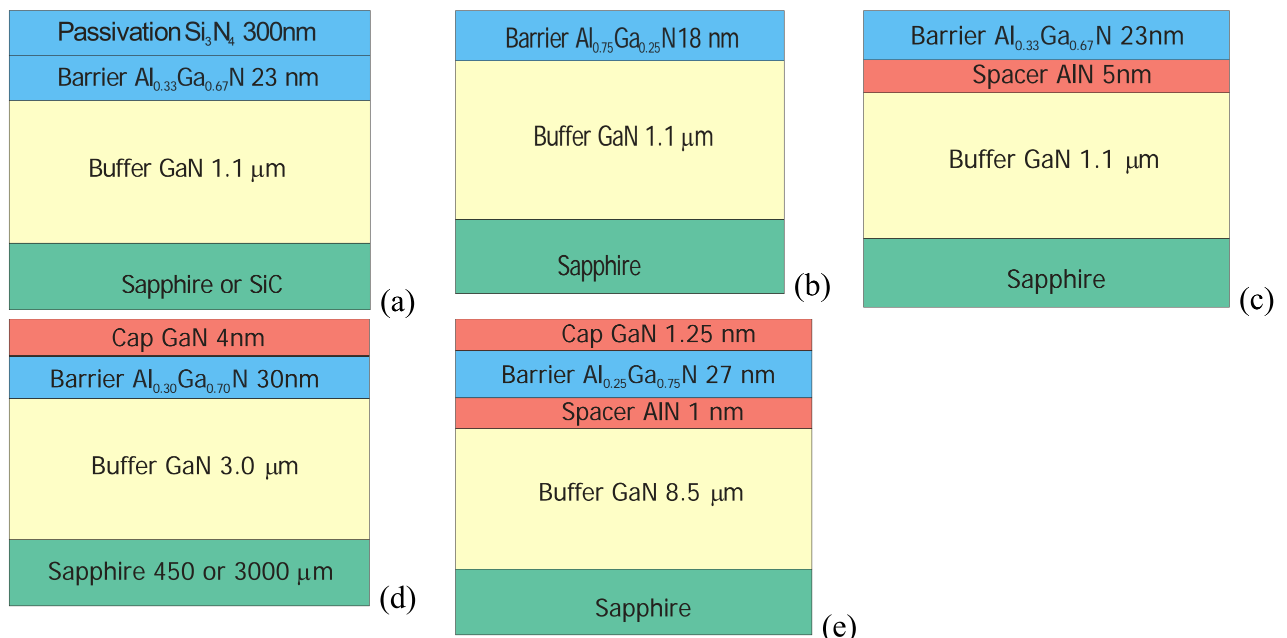

Figure 2.3. Schematics of single barrier heterostructures under investigation.

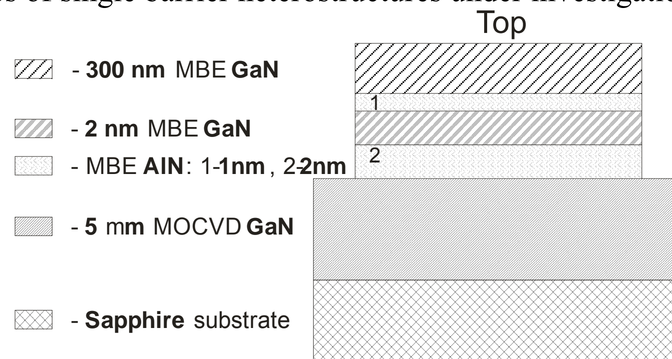

Figure 2.4. Schematics of double barrier heterostructures under investigation.

Devices were processed using Clean room facilities of Forschungszentrum Juelich. The transport properties of these devices were studied by magnetoresistance analysis, noise spectroscopy, current-voltage and capacitance-voltage techniques.

For the convenience, in further discussion the HEMT samples shown in Fig. 2.3 (a) will be labeled as sample #A, in Fig. 2.3 (b) – as sample #B, etc.

Chapter 3. Transport Phenomena of AlGaN/GaN Heterostructures in Magnetic Field

In this chapter the results of AlGaN/GaN devices measurements at low temperatures in external magnetic field are presented. The magnetoresistance, SdH oscillations, weak antilocalization effect, SOI effect are investigated and analyzed.

Experimental Details and Theory

In magnetic fields, electrons (or holes) perform a cyclotron motion with frequency

$$\omega_c = eB/m^* \quad (3.1.1)$$

where B – magnetic field, m^* - effective mass.

The free cyclotron motion can only occur between two scattering events. Thus, to study cyclotron motion and magnetotransport properties of charged carriers are only possible when

- $\omega_c\tau >> 1$, i.e. when the average scattering time t is sufficiently large. This requires high mobility.
- the magnetic field is sufficiently strong and the temperature sufficiently low, i.e. $\hbar\omega_c > kT$, such that thermal excitations do not scatter electrons between different Landau levels.
- the cyclotron path is free of geometric obstructions.

Investigation of transport phenomena of semiconductor structures in magnetic field requires sufficiently low-temperatures. The standard technique for producing temperatures in the range between 300 K and 4.2 K involves the use of cryogenic liquids N_2, ^4He and ^3He, which have boiling point 77.4 K, 4.21 K and 3.19 K respectively. In order to reduce the temperature of liquid helium one often simply pumps the vapor above the helium bath. In this way, it is possible to reach temperatures down to about 1.3 K without much effort. However, this procedure results in enormous helium consumption, since cooling the liquid from 4.2 K to 1.3 K requires about 40% of the liquid helium to be evaporated. More elegant and efficient method of cooling is the use of an additional vessel filled with ^4He or ^3He that is located inside a vacuum chamber (Fig. 3.1). In this case, the temperature is lowered only in a much smaller system, reducing the helium consumption needed to produce the low temperature. In addition, this method requires a lower pumping capacity as compared to pumping the larger main bath. Continuous operation of such a cryostat can be achieved by refilling the separate small vessel via a small capillary from the main

helium bath. To prevent the inflow of impurities, or small particles, which potentially could block the capillary, a filter made of sintered metal is usually installed in front of the capillary.

The use of ^{3}He has two essential advantages over ^{4}He. First, the high vapor pressure allows temperatures as low as 0.3 K to be reached with modest pumping systems. Secondly, ^{3}He does not possess the problem created by the superfluid film, which leads to an unwanted heat transport from warm to cold parts in ^{4}He evaporation cryostats. However, the cost for ^{3}He is much higher than for ^{4}He.

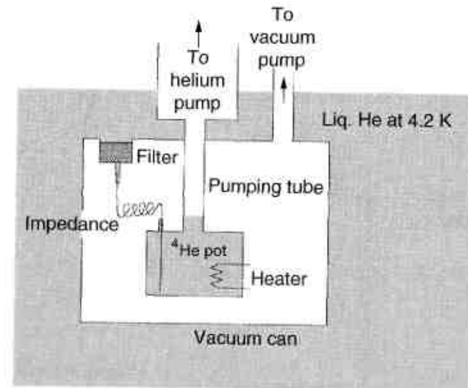

Figure 3.1. Schematic diagram of a continuously operating ^{4}He evaporation cryostat with a separate ^{4}He pot [120].

Two principal versions of ^{3}He cryostats can be distinguished, namely continuously working ones in which the ^{3}He is recirculated, and single-shot cryostats in which the ^{3}He is first condensed into a pot and subsequently pumped out. Recirculation of the ^{3}He typically results in a 10% higher minimum temperature in comparison to single-shot operation.

A special class of ^{3}He evaporation cryostats are systems with an adsorption pump. In this case, the ^{3}He that is condensed into the ^{3}He pot is adsorbed onto the cold surface of a sinter of fine metal powder, or onto charcoal powder. Because of the large surface area of these materials the ^{3}He is pumped very efficiently. While in operation, this adsorption pump is thermally anchored at a pumped ^{4}He pot (often called a 1K pot), which provides the required low temperatures.

After the ^{3}He pot is empty and the pumping is finished, the adsorption pump is pulled up to a warmer region in the cryostat. Upon warming, the ^{3}He is desorbed from the powder and then condenses into the ^{3}He pot. The cycle can be started again by cooling the adsorption pump back to the temperature of the 1K pot. A design of such a cryostat is shown in Fig. 3.2. In this case, the charcoal pump is manipulated via chains using a spindle valve. Because of their enormous pumping power, ^{3}He cryostats with absorption pumps have high cooling powers compared to those with mechanical pumps.

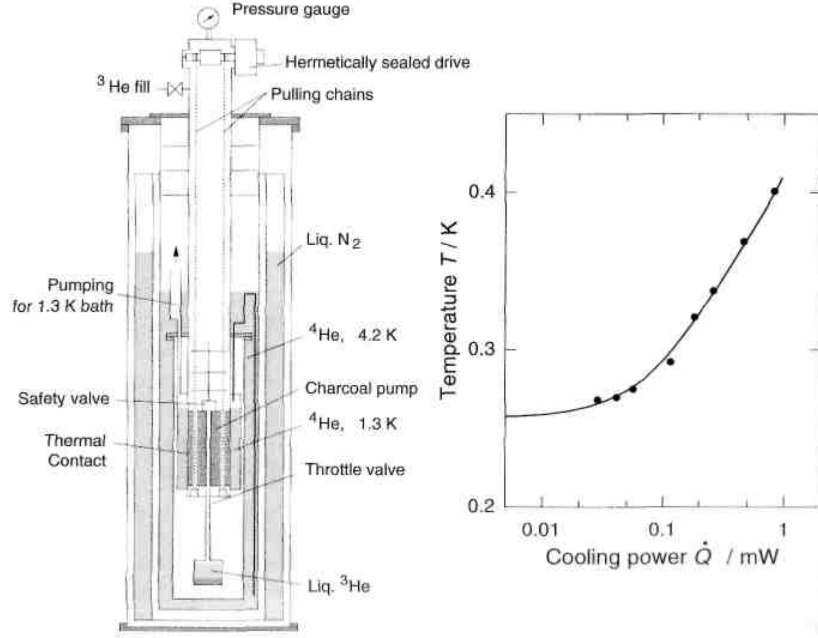

Figure 3.2. Sketch of a ^{3}He cryostat with charcoal absorption pump [120].

In order to investigate the effect of magnetic field on properties of samples under test the cryostats are mounted with superconducting magnet (niobium based), which is fully submerged into main ^{4}He bath and provide magnetic fields up to 22 T [121].

In a magnetic field the density of states in two-dimensional electron gas system *Z* acquires an oscillatory component *ΔZ* which, at low fields, can be written as [122]

$$\frac{\Delta Z(E)}{Z_0} = 2\sum_{m=1}^{\infty} \exp(-\pi m / \omega_c \tau_q) \cos\left(\frac{2\pi m E}{\hbar \omega_c} - m\pi\right) \tag{3.1.2}$$

where Z_0 is the zero-field density of states, and *E* is the electron energy, $\tau_q = \frac{\hbar}{2\Gamma}$. The above expression assumes that the Landau levels are broadened and each can be represented by a Lorentzian with a width *Γ* independent of energy or magnetic field. The oscillation in *Z*, results in oscillatory behaviour in all the physical properties, particularly in conductivity and resistivity.

Oscillatory part of resistivity at finite temperature can be written as

$$\frac{\Delta \rho_{xx}}{\rho_0} = 2\sum_{m=1}^{\infty} P_m(T) \frac{\Delta Z_m(E_{F0})}{Z_0}, \tag{3.1.3}$$

where $P_m(T) = \frac{m\chi(T)}{\sinh(m\chi(T))}$ – temperature damping factor, where $\chi(T) = \frac{2\pi^2 kT}{\hbar\omega_c}$, and index *m* corresponds to m^{th} oscillatory term.

The observed effect of oscillations of longitudinal resistance when an external magnetic field is applied to a two-dimensional electron gas called the Shubnikov–de Haas effect, and is highly useful in characterizing a two-dimensional electron system.

Each minimum in oscillatory component of resistivity corresponds to alignment between Fermi energy and a Landau level. This can be expressed by

$$(N+\frac{1}{2})\hbar\omega_c = E_{F0}, \tag{3.1.4}$$

where N – Landau level number.

Taking into account that Fermi energy in 2DEG system can be expressed as

$$E_{F0} = \frac{\pi\hbar^2 n_S}{m^*} \tag{3.1.5}$$

it become obvious that 2DEG sheet concentration can be extracted from linear fit of N on $1/B_N$ dependence (B_N – magnetic field at which minimum of resistivity occurs)

$$N = \frac{\pi\hbar n_S}{e}\frac{1}{B_N} - \frac{1}{2}. \tag{3.1.6}$$

Analysis of eq.(3.1.3) shows that using the temperature dependence of amplitude of SdH oscillation:

$$A_m(T) = 4P_m(T)\exp(-\frac{\pi m}{\omega_c \tau_q}) \tag{3.1.7}$$

one can estimate the value of effective mass of 2D carriers. At high temperatures the logarithm of the amplitude can be written as

$$\ln(\frac{A_m}{T}) = -m\chi(T) + const(independed\ of\ T) \tag{3.1.8}$$

Quantum lifetime τ_q can also be estimated from dependence of the amplitude on magnetic field at given temperature.

From the free-electron dispersion relation $E = \frac{\hbar^2 k^2}{2m}$ the mass of the particle is inversely proportional to the curvature of the dispersion relation, i.e.

$$\frac{1}{m^*} = \frac{d^2 E}{dk^2} \tag{3.1.9}$$

It should be noted that in general case effective mass is a tensor $(m^{*-1})_{ij} = \frac{\partial^2 E}{\partial k_i \partial k_j}$ [122].

Usually, the dispersion around the conduction-band minimum is only parabolic for small k. The larger wave vector the more the actual dispersion deviates from the ideal parabola. This effect is called nonparabolicity. Typically, the energy increases less quickly with k than in the

parabolic model. This can be described in a so-called two-level model with the dispersion relation [122]

$$\frac{\hbar^2 k^2}{2m_0^*} = E\left(1 + \frac{E}{E_0^*}\right) \tag{3.1.10}$$

where $E_0^* > 0$ parameterizes the amount of nonparabolicity (a parabolic band corresponds to $E_0^* = \infty$). The curvature is reduced for larger k and thus the effective mass is energy dependent and increases with the energy. Equation (3.1.10) leads to the energy-dependent effective mass

$$m^*(E) = m_0^*\left(1 + \frac{2E}{E_0^*}\right) \tag{3.1.11}$$

where m^*_0 denotes here effective mass at k=0.

Another effect, which leads to an increase of effective mass, is polaronic effect. In ionic lattice, the electron polarizes the ions causes a change of their equilibrium position. The electron movement results in dragging this ion displacement together with this electron. The enhancement of the effective mass due this effect can be expressed by

$$m_p^* = m^*(1 + \alpha/6 + 0.025\alpha^2) \tag{3.1.12}$$

where m^* is ideal effective mass given by (3.1.9) and α the Froehlich coupling constant [123].

With introduction of semiconductor heterostructures another important effect has an influence on effective mass value of 2D carriers, namely wave function hybridization. Because of special extention the tails of the wave function of electrons occupying the lowest subband penetrate into the layers confining the triangular well. The barrier wave function penetration then causes the effective mass value to drop off toward the barrier bulk mass value. In other words it leads to the enhancement of the effective mass value. The effective mass on ith subband of real heterostructure can be defined as [124]:

$$\frac{1}{m_i} = \int dz \psi_i^2(z) \frac{1}{m(z)} \tag{3.1.13}$$

where m_i is the effective mass of electron in the i-th subbband, ψ_i is the electron wave function of ith subband, *m(z)* is the position dependent effective mass, *z* is the direction perpendicular to the interface. In the case of flat band the right part of the Eq. (3.1.13) can be solved analytically:

$$\frac{1}{m_i} = \frac{1}{m_{wL}}\left[1 - P_b(E_i)\right] + \frac{1}{m_{bL}} P_b(E_i) \tag{3.1.14}$$

where m_{wL} is the effective mass in the quantum well layer, m_{bL} is the effective mass in the barrier layer. It is obvious that real heterostructures are far away from flat band conditions and therefore this simplified approximation for in-plane effective mass determination cannot be applied to real

case. The quantitative evaluation of the wave function penetration effect is difficult because theoretical models draw a very approximate picture and cannot take into account all factors influenced by depth and form of the triangular well formed at the interface.

External magnetic fields allow the investigation of the effect of splitting of the spin states. For the electron, the energy splitting ΔE is given by

$$\Delta E = g_e^* \mu_B B , \tag{3.1.15}$$

where B is the magnetic-field amplitude and g^* the (effective) electron g-factor. This value differs from the free-electron value in vacuum of g_e = 2.0023 due to the presence of spin-orbit interaction.

In high mobility 2DEG with only one populated subband the spin-orbit coupling leads to a splitting into two-spin separated subbands. There are few theoretical approaches describing mechanisms of spin orbit interaction in solids. In case of asymmetric quantum well spin-orbit interaction (SOI) usually described by Bychkov-Rashba mechanism [125].

For this case, the Hamiltonian of the system with spin-orbit interaction of an electron is

$$\hat{H} = \frac{\hbar^2 k^2}{2m^*} + \alpha_{SO} \left[\vec{\sigma} \times \vec{k} \right]_Z \tag{3.1.16}$$

where $\vec{\sigma}$ are the Pauli matrices, α_{SO} – Rashba constant, which is a measure of SOI strength. The spin-splitting at Fermi surface can be written as

$$\Delta_{SO} = 2\alpha_{SO} \hbar k_F \tag{3.1.17}$$

Experimentally, spin split III-V heterostructures can be studied by measuring SdH oscillations. A characteristic beating pattern indicates the occupation of two different subbands due to spin-orbit coupling of the electrons in the channel. As shown in [126] α_{SO} can be calculated with

$$\alpha_{SO} = \frac{\Delta n \hbar^2}{m^*} \sqrt{\frac{\pi}{2(n - \Delta n)}} \tag{3.1.18}$$

where Δn – difference in population between two spin-separated subbands, and n – electron density in degenerated state.

Another phenomenon, which is highly influenced by spin-orbit interaction, is weak localization. Using the functional dependence of the magnetoconductity, $\sigma(B)$, in classically weak magnetic fields, provides a sensitive tool for the extraction of strength of the spin-orbit (SO) coupling. At low-temperatures, when elastic scattering of carriers is dominating in periodic network of scatters (i.e atoms in crystal structure), the effect of interference between incident and

backscattered waves highly influences transport properties, such as conductivity, of the system [127]. It should be emphasized that effect of weak localization is only possible in systems with some deviation from ideal crystallinity (i.e. with presence of defects and inhomogenities in periodic structure).

In the presence of magnetic field the correction to conductivity $\Delta\sigma$ due to localization can be written as

$$\frac{\Delta\sigma}{\sigma_0} = \psi\left(\frac{1}{2} + \frac{\hbar}{4eBD\tau_\phi}\right) - \psi\left(\frac{1}{2} + \frac{\hbar}{4eBD\tau}\right) \quad (3.1.19)$$

where $\sigma_0 = \frac{e^2}{2\pi h}$, D – is diffusion constant, τ_ϕ – the inelastic dephasing time, τ – average time between two elastic scattering events, ψ is di-gamma function (see. Appendix B).

In system with spin-orbit interaction of Bychkov-Rashba kind the magnetoconductivity can be written as [128]:

$$\frac{\Delta\sigma}{\sigma_0} = \sum_{s=0,\pm1} u_s \psi\left(\frac{1}{2} + \frac{B_\varphi}{B} - v_s\right) - \psi\left(\frac{1}{2} + \frac{B_\varphi}{B}\right) - 2\ln\left(\frac{B_\varphi}{B}\right) + \frac{4B^2}{4(B_{SO} + B_\varphi)^2 - B^2}$$
$$- 2\ln\left(1 + \frac{B_{SO}}{B_\varphi}\right) - \ln\left(1 + \frac{2B_{SO}}{B_\varphi}\right) + \frac{8}{\sqrt{7 + 16\frac{B_\varphi}{B_{SO}}}} \cos^{-1}\left(\frac{2\frac{B_\varphi}{B_{SO}} - 1}{\sqrt{\left(2\frac{B_\varphi}{B_{SO}} + 3\right)^3 - 1}}\right) \quad (3.1.20)$$

where

$$v_s = 2\delta\cos\left(\theta - \frac{2\pi}{3}(1-s)\right), \quad u_s = \frac{3v_s^2 + 4b_{SO}v_s + 5b_{SO}^2 + 4b_{SO}b_\varphi - 1}{\prod_{s \neq s'}(v_s - v_{s'})}, \quad (3.1.21)$$

$$\delta = \sqrt{\frac{1 - 4b_{SO}b_\varphi - b_{SO}^2}{3}}, \quad \theta = \frac{1}{3}\cos^{-1}\left(-\left(\frac{b_{SO}}{\delta}\right)^3\left(1 + \frac{2b_\varphi}{b_{SO}}\right)\right), \quad (3.1.22)$$

$$B_{SO} = \frac{\hbar}{4eD\tau_{SO}}, \quad B_\varphi = \frac{\hbar}{4eD\tau}, \quad b_{SO} = \frac{B_{SO}}{B}, \quad b_\varphi = \frac{B_\varphi}{B}, \quad (3.1.23)$$

$$\text{and} \quad \frac{1}{\tau_{SO}} = D\left(\frac{2m^*\alpha_{SO}}{\hbar}\right)^2, \quad \alpha_{SO} = \frac{1}{2\sqrt{\pi n_S}\sqrt{\tau\tau_{SO}}}. \quad (3.1.24)$$

In low field limit ($B<<B_{SO}$) the equation (3.1.20) can be rewritten as [129]:

$$\frac{\Delta\sigma}{\sigma_0} \approx \psi\left(\frac{1}{2}+\frac{B_\varphi + B_{SO}}{B}\right) - 2\ln\left(\frac{B_\varphi + B_{SO}}{B}\right) + \psi\left(\frac{1}{2}+\frac{B_\varphi + 2B_{SO}}{B}\right) - \ln\left(\frac{B_\varphi + 2B_{SO}}{B}\right) \psi\left(\frac{1}{2}+\frac{B_\varphi}{B}\right) + \ln\left(\frac{B_\varphi}{B}\right) \qquad (3.1.25)$$

The fitting of experimental data on low-filed magnetoconductivity with formula (3.1.20) or (3.1.25) allows evaluation of characteristic times and Rashba constant of SOI.

Electron Effective Mass in AlGaN/GaN 2DEG

Figure 3.3 shows the trace of the typical evolution of resistance measured in a perpendicular magnetic field up to 10 T at different temperatures. The Shubnikov-de Haas (SdH) oscillations are clearly resolved starting with magnetic field of 2 T. From the SdH oscillations period the sheet concentrations of the 2DEG are calculated with use of eq. (3.1.6)

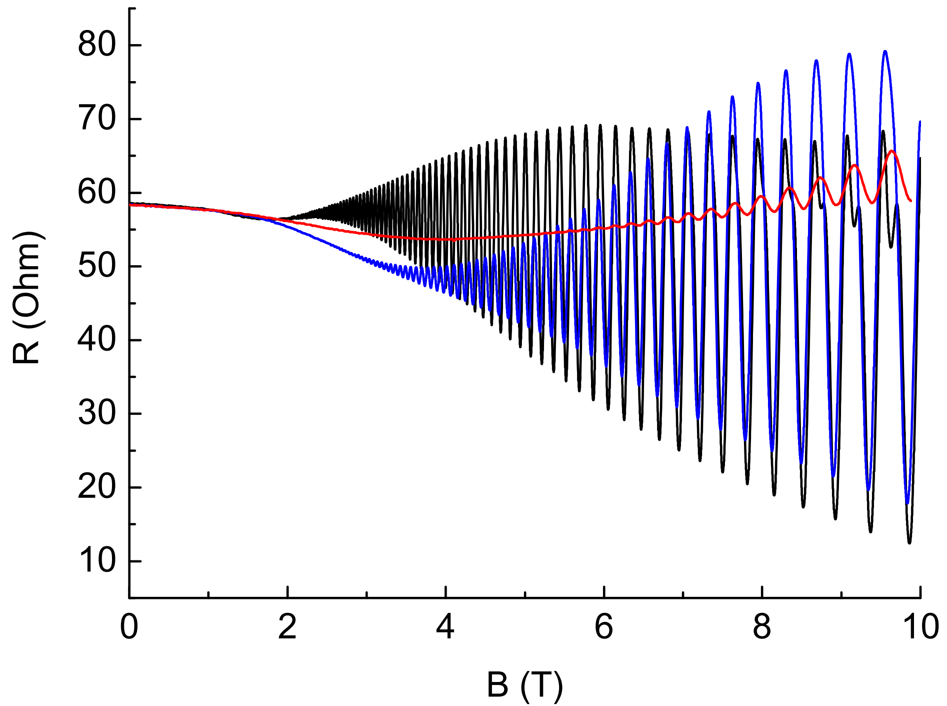

Figure 3.3. The measured magnetoresistance of sample #E at different temperatures.

As it was shown in previous chapter, knowing the temperature dependence of SdH oscillation amplitude makes it possible to estimate the effective mass value of the electrons in 2DEG (see eq. 3.1.7).

The cyclotron-resonance and the SdH oscillations are the two experimental techniques most widely used for the determination of the effective mass. In the cyclotron-resonance experiment, the separation of adjacent Landau levels, $\hbar\omega_c$, is measured as a function of the magnetic field B, allowing the effective mass m_E^* to be deduced from the relationship $m_E^* = eB/\omega_c$. Due to the conduction band nonparabolicity the spacing between Landau levels becomes irregular and, as a consequence, the measured effective mass manifests a dependence on the magnetic field. In the case of the SdH experiment, the situation is quite different. The SdH oscillations occur because the conductivity, σ_{xx}, depends on the density of states at the Fermi energy, $Z(E_F)$, both through the number of carriers and through the scattering rate.

Very often in analysis of SdH oscillations a simplified function (3.1.8) is used in the fitting procedure. However, it should be noted that the given approximation is not necessarily valid in the whole temperature range where the oscillations are observed. Figure 3.4 demonstrates the results of the fitting procedure performed for sample #D with using Eqs. (3.1.7) and (3.1.8).

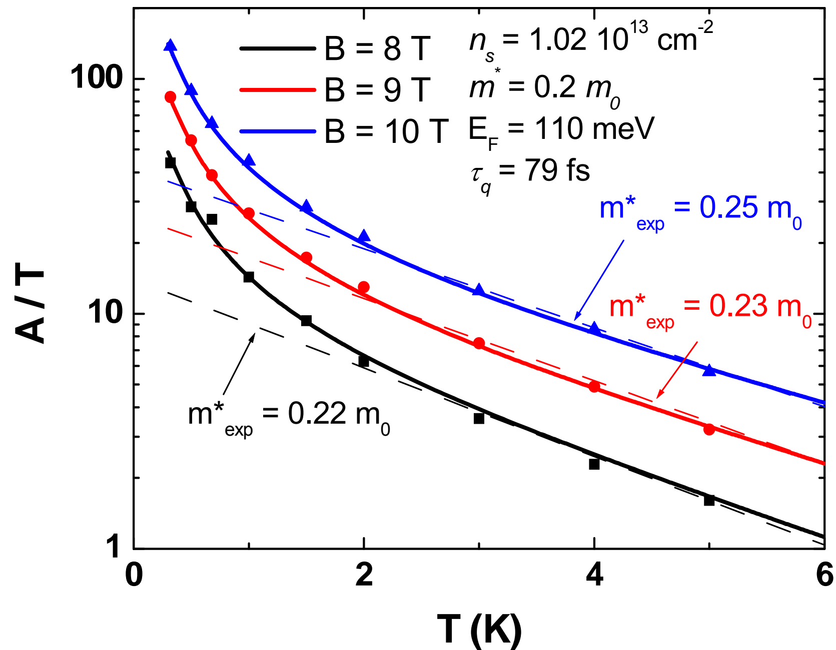

Figure 3.4. Amplitudes of SdH oscillations plotted as a function of temperature. Squares, circles and triangles correspond to oscillations observed at a magnetic field close to 8 T, 9 T, 10 T, respectively. Solid and dashed lines represent the fit by Eq.(3.1.7) and Eq.(3.1.8), respectively.

It is clearly seen from the Fig.3.4 that the simplified exponential dependence, first, brings an overestimated value of the effective mass and, second, reveals the effective mass dependence on magnetic field. At the same time the effective mass, estimated by using Eq.(3.1.7), is equal 0.2 m_0 for three different magnetic fields. As already mentioned above the SdH oscillations occur when the sequential Landau level crosses the Fermi level. Thus, the amplitude of each oscillation corresponds to the effective mass at the Fermi energy and we do not expect any magnetic field dependence of the effective mass at least for Landau levels with high indexes.

It should be emphasized that to obtain reliable experimental data at low temperatures (lover then 2K) low electric current (~100nA) should be supplied to structures under test in order to avoid overheating (see Fig. 3.5). It was revealed that current heating during the measurements gives overestimated effective mass.

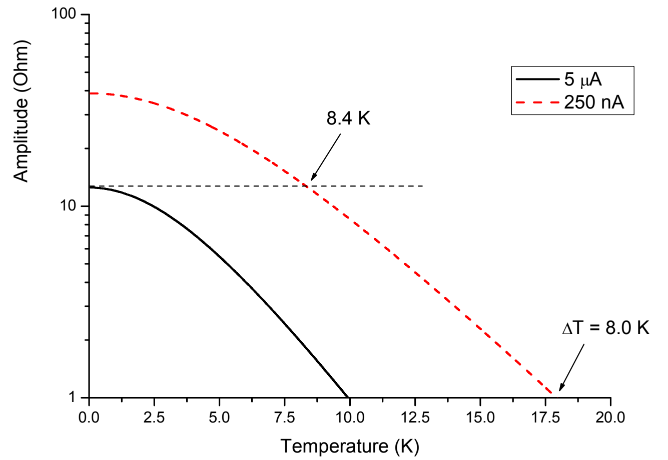

Figure 3.5. Amplitude of SdH oscillations of sample #A as a function of temperature measured at two different currents: 5 μA and 250 nA.

The results of analysis of SdH oscillations in different samples are summarized in table 3.1. where E_F is the Fermi energy measured starting from the with quantization energy E_0, n_S is the carrier concentration, m_E^* is the effective mass at the Fermi energy, τ_t is the transport lifetime, τ_q is the quantum lifetime, μ is the carrier mobility. The carrier concentration measured at low- (Hall effect) and high- (SdH oscillations) magnetic fields was the same order of magnitude (determined by polarization induced charge and strain distribution in the layers) for the investigated samples. The fact indicates that only the lowest subband is occupied.

Table 3.1.

Sample	E_F (meV)	n_s (10^{13}, cm^{-2})	m_E^* (m_0)	τ_t/ τ_q	μ (cm^2/V.s) (0.35K/300K)
#A	130	1.1	0.22±0.01	4.3	2300/1380
#D	121	1.02	0.20±0.01	7.7	5100/1260
#E	119	1.01	0.19±0.01	13.7	11500/1850

Analysis of the effective mass column of Table 3.1 reveals the inconsistence between the increase of the mass value from sample #E to sample #A and a minor change in carrier concentration**.** The fact cannot be explained by the conduction band nonparabolicity effect only.

Comparing τ_q with the momentum relaxation time τ_t determined from the zero-field mobility (1.3.3)*,* we find that the lifetime ratio. Since this ratio is not large in comparison to unity, we conclude that the small-angle scattering does not dominate, and the main scattering mechanism of carriers in our samples is the short-range scattering processes (possibly, the alloy scattering).

To elucidate the origin of the effective mass enhancement as well as the large scatter of the data known in literature we have to look more precisely for sources causing this effect.

A. The conduction band nonparabolicity effect.

The quantitative evaluation of band nonparabolicity in a triangular well formed at the AlGaN/GaN interface can be obtained according to the Ando approximation

$$\frac{m_E^* - m_0^*}{m_0^*} = \left[1 + 4(\langle K \rangle \ + E_F)/E_g\right]^{1/2} - 1 \qquad (3.2.1)$$

where m_0^* is the effective mass at the band edge, $\langle K \rangle$ is the kinetic energy, respectively and E_g is the bandgap energy. $\langle K \rangle$ can be estimated approximately as $E_0/3$, while the E_0 can be calculated from the simple Hartree formulation [130]. In the real cases the depth and curvature of the triangular well depend on number ofseveral factors – the polarization charge at the interface, doping, structure design, growth conditions, etc. – and could be quite different for samples with the same 2DEG concentration. The theoretical models are using idealize the energy picture. Estimations performed for the samples with $n_s \approx 10^{13}$ cm^{-2} taking 0.2 m_0 as the band edge effective mass bring approximately a 10% effective mass enhancement. Even using the more accurate Fang-Howard model [131] to calculate $\langle K \rangle$ does not considerably change the result.

B. The polaron effect.

Taking into account the large Fröhlich constant ($\alpha = 0.49$ [132]) for electron-longitudinal optical (LO) phonon coupling in polar GaN, we could expect a visible influence of polaron effect on the effective mass enhancement. However, the screening effect of the electron-LO phonon interaction as well as the quantum confinement of the electron wave function strongly suppress the polaron effect. According to the Das Sarma result [133] the polaron effective mass in this case can be written as

$$m_P^* = m_E^*\left[1 + (\pi\alpha/8)F(\gamma,\beta)\right], \tag{3.2.2}$$

where parameters $\gamma = q_{TF}/q_0$ and $\beta = b/q_0$ determine the strength of the screening and quantum confinement effects, respectively. Here q_{TF} is the two-dimensional screening constant, q_0 is LO-phonon wave vector, b is the variational parameter [133]. In the case of samples studied $F(\gamma,\beta) \approx 0.3$, therefore the polaron effect contribution to the effective mass correction does not exceed 3%. ByIn other words its effect is within the experimental error.

C. Wave function hybridization effect.

Because of the spatial extension the tails of the wave function of electrons occupying the lowest subband penetrate into the layers confining the triangular well. The barrier wave function penetration then causes the effective mass value to drop off toward the barrier bulk mass value. In other words, it leads to the enhancement of the effective mass value. To interpret quantify this kind enhancement of the effective mass enhancement, we calculated the energy band structure and the envelope wave function of the first subband for samples #A, #D and #E, using a self-consistent solution of Schrödinger and Poisson equations. The most remarkable difference of wave function penetration into barrier layer was found for samples #A and #E. The results are shown in Fig. 3.6.

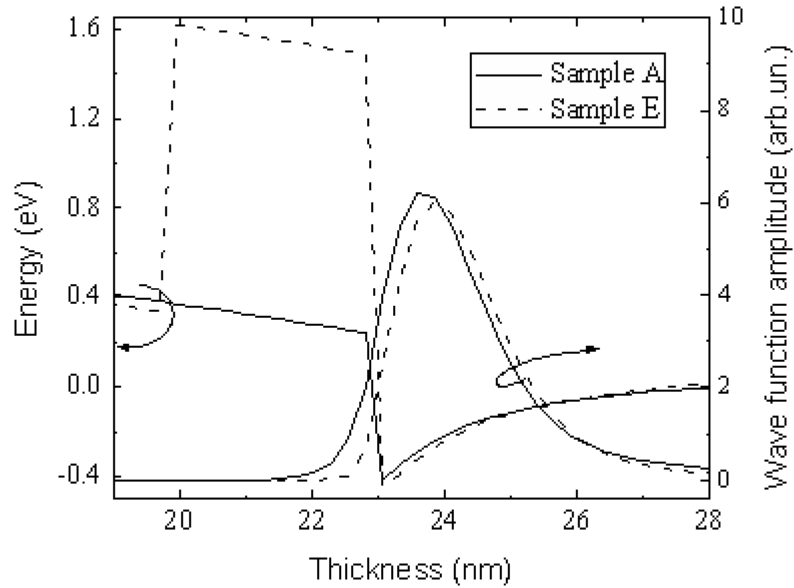

Figure 3.6. Calculated potential profile and wave function distribution for samples #A and #E.

It is seen that the addition of an AlN spacerlayer in sample #E reduces the wave function penetration into the barrier for a fixed well width. At the same time, the electrons in the first subband of sample #A are closer to the interface and. Their wave function extends deeper into the AlGaN barrier, resulting into a higher effective mass compared to sample #E. The results confirmed by experimental data obtained for samples #A, #D and #E, summarized in Table 3.1.

The solution of Eq. (3.1.14) using self –consistently calculated probabilities of wave function penetration in the barrier region of real heterostructures #A, #D, and #E gives underestimated in-plane effective mass values. It is obvious this simplified approximation cannot be applied for determination of effective mass in real heterostructure. The quantitative evaluation of the wave function penetration effect is difficult because theoretical models draw a very approximate picture and cannot take into account all factors influenced by depth and form of the triangular well formed at the interface. Nevertheless, we propose an empirical formula that could approximately estimate the contribution of the wave function hybridization to the effective mass enhancement:

$$m^*_{corr} = [1 + (\frac{E_0}{\Delta_c})^2 \frac{m^*_b}{m^*_w}] m^*_0 \ , \tag{3.2.3}$$

where m^*_{corr} is corrected effective masses, Δ_c, m^*_b are the conduction band offset and effective mass in the barrier, respectively; m^*_w is the effective mass in the quantum well at level with energy E_0 (relative to the conduction band edge). Using m^*_0 as a fitting parameter we achieve the lowest discrepancy between experimental and approximation results with value of m^*_0 = 0.185 m_0. This value together with band parameters calculated for samples #A, #D and #E allows estimating the contribution of wave function hybridization into the effective mass enhancement (Table 3.2).

Table 3.2.

Sample	#A	#D	#E
m^*_w (m_0)	0.185	0.185	0.185
m^*_b (m_0)	0.266	0.260	0.400
E_0 (eV)	0.29	0.25	0.34
Δ_c (eV)	0.61	0.59	2.00
m_E^* (m_0)	0.220	0.200	0.190
m^*_{corr} (m_0)	0.215	0.208	0.190

In spite of a very approximate character of the performed procedure, the values of the corrected effective mass are very close to the values obtained in the experiment for all samples. The fact proves the dominant role of the wave function penetration in the enhancement of the 2DEG effective mass. It should be noted, that the Eq. (3.2.3) allows to obtain the effective mass using the main parameters of real heterostructure, such as quantization energy, E_0, and band offset Δ_c. Moreover the hybridisation describes very well the effective mass enhancement in case of each specific potential profile of the samples. Therefore the Eq. (3.2.3) can be applied to different GaN-based heterostructures for estimation the influence of wave function hybridisation. In order to verify the formula (3.2.3), it was applied to our data and data found in literature. Figure 3.7 clearly shows reasonable coincidence between experiment and eq. 3.2.3.

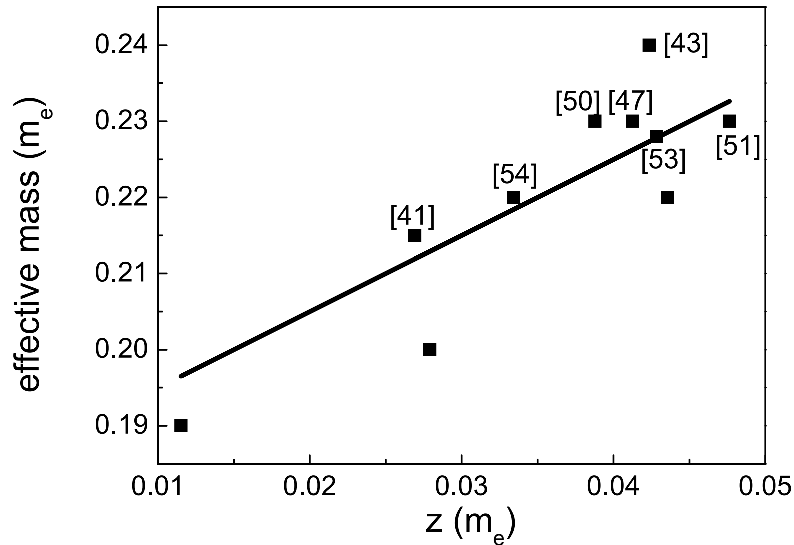

Figure 3.7. Effective mass vs. $z = \left(\frac{E_{F0}}{\Delta E_C}\right)^2 m_b$, square dots – experimentally obtained values, solid line fitting of the data with eq. 3.2.3.

Study of Spin-Orbit Interaction

Spin-split SdH oscillations of sample #E become well resolved at a magnetic field B >8 T as it is seen in Fig.3.8.

From the observed LLs spin splitting we were able to estimate the g-factors at different LL indices. Indeed, we did not observe any beating patterns in the magnetoresistance trace. Thus, as an approximation, the effective g-factor, g^*, can be obtained by the standard equation,

$$g^* = (n+\frac{1}{2})\frac{2\hbar e}{m^*\mu_B}\frac{(B_{n-}-B_{n+})}{(B_{n+}+B_{n-})} \qquad (3.3.1)$$

where B_{n+} and B_{n-} are the experimental values of the magnetic field when spin-up and spin-down levels of the *n*th Landau level pass through the Fermi level, respectively. Here we used the relation of the effective g-factor to the spin-splitting energy, Δ_{ss}, in the form $\Delta_{ss}=g^*\mu_B B$, where μ_B is the Bohr magneton.

By using Eq.(3.3.1) values of g^* were calculated for LLs with n = 20, 21, and 22 equal to 3.7, 3.3, and 2.8, respectively.

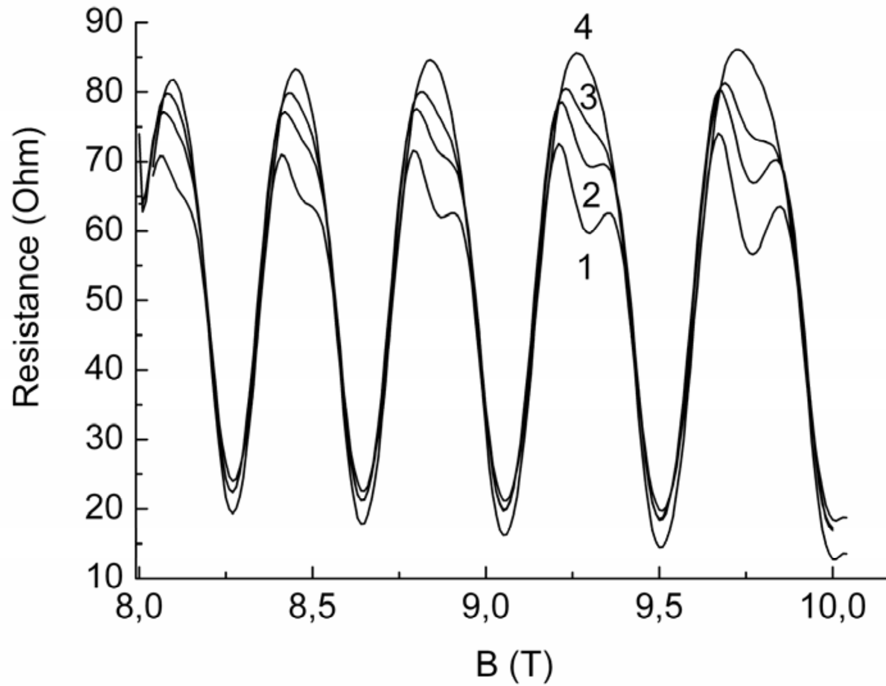

Figure 3.8. High magnetic field part of magnetoresistance of samle #E, at different temperatures: 1 – 0.3 K, 2 – 0.6 K, 3 – 1.0 K, 4 – 2.0 K.

As it was mentioned previously GaN and the nanostructures on its basis are the promising materials of semiconductor spintronics. Therefore, it is important to study the spin-orbit interaction (SOI) which determines the spin dynamics in these systems. The quantum wells forming at the heterojunction AlGaN/GaN and containing 2DEG are the useful object for the investigation of SOI. The confining potential in the quantum well, being determined by the growth, structural features, and the applied electric field *E,* possesses the structural inversion asymmetry. As a result, the 2DEG energy spectrum, in the lowest order of the wave vector k, is described by the (3.1.16).

It is known that the SOI manifests itself in the magnetoconductivity of the 2DEG. In low magnetic fields (of the order of 1 mT) one observes the effect of weak antilocalization. The low-field

magnetotransport in 2DEG is a more suitable tool for investigation of the SOI in GaN-based heterostructures. Owing to the SOI, the anomalous negative magnetoresistance, which is caused by the weak localization effect, becomes positive in low magnetic fields (the antilocalization effect). In the present study, we have investigated the magnetoresistivity of the single heterojunction AlGaN/GaN (sample #A). We have observed the maximum in the dependence of the resistivity on the magnetic field. The height of this maximum decreased with the increase of the temperature. Using the expression for the magnetoconductivity (3.1.25), a fit of the experimental data to the theoretical results has been carried out. Based on this procedure, the Rashba constant, the spin-orbit splitting at the Fermi level Δ_{SO}, and the spin-orbit (Dyakonov-Perel) relaxation time τ_{so} have beed estimated.

The 2DEG resistivity of the heterojunction $Al_{0.33}Ga_{0.67}N$/ GaN has been investigated also in the weak magnetic fields $B < 0.08$ T at several temperatures ranging between 0.3 K and 1 K (Fig. 3.9).

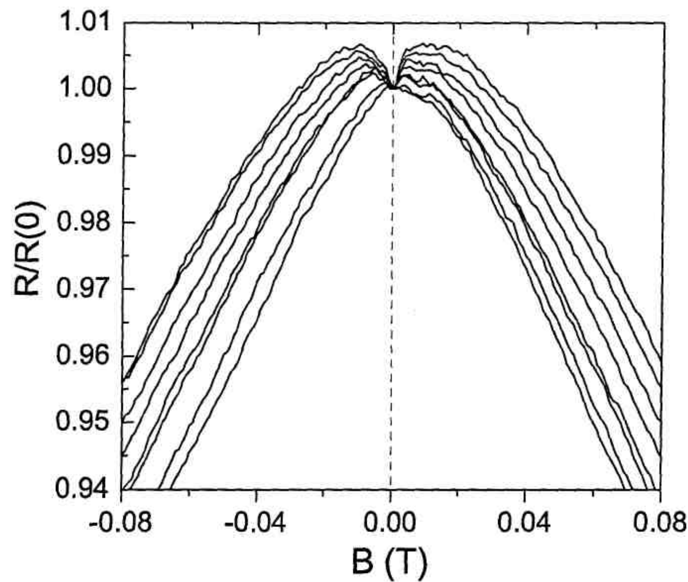

Figure 3.9. Dependence of the 2DEG resistance of the sample #A on th e magnetic field B measured at temperatures from 0.3 K to 1 K with 0.1 K step , form upper to lower plots respectively.

The dependences shown in Fig. 3.9 are nonmonotonic and have maxima at characteristic fields $B = B_{SO.}$ The height of the magnetoresistivity maxima decreases with the increase of the temperature, and the extremum disappears at T > 0.9 K. The position of the maxima for the curves in Fig. 3.9 is not stable. The characteristic magnetic fields *Bso* are close to 0.01 T, which exceeds B_{SO} for the systems with low 2DEG density. The fit of theoretical curves to the measured conductivity is carried out. The experimental and theoretical curves for the magnetoconductivity

at the temperatures T = 0.3 K and 0.5 K are given in the Fig. 3.10. The theory of weak antilocalization satisfactory describes our experimental data in the region of fields $B < 0.02$ T by using the reasonable fitting parameters we obtain τ_φ ranging from 70 ps to 25 ps.

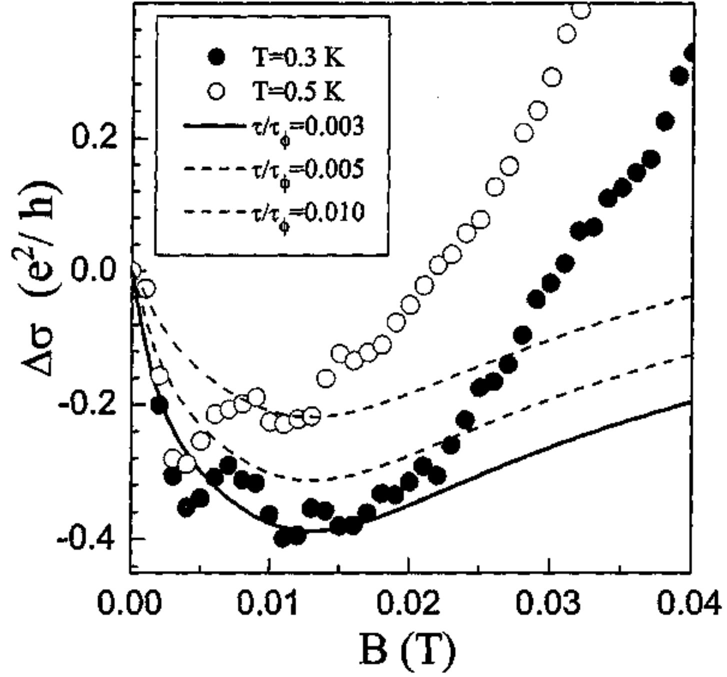

Figure 3.10. Experimental dependence of the 2DEG conductivity of the sample #A on magnetic field B, at T = 0.3 K and T = 0.5 K together with the results of calculation according to the theory (eq. 3.1.20, 3.1.25) using the parameters indicated.

The results presented above give the Rashba constant 1.01xl0^{-12} eVm, the spin-orbit splitting energy at the Fermi level Δ_{SO} = 2 meV, and the spin-orbit relaxation rate $1/\tau_{SO}$= 1.25 ps^{-1}.

Summary

In summary, the dependence of the in-plane effective mass of the 2DEG formed at the AlGaN/GaN heterojunction as a function of the quantum confinement is invesigated. The factors influencing the effective mass enhancement were analyzed. It is shown that in most cases the conduction band non-parabolicity effect is overestimated and that the wave function penetration into the barrier layer should be taken into account. It is shown that the wave function hybridization effect on effective mass enhancement is dominating over band non-parabolicity effect and polaron effect. The band edge effective mass value is deduced to be 0.185 ±0.01 m_0. The empirical formula (3.2.3) is proposed for quantitative estimation of mass enhancement due to wave function hybridization. The experimental results are in a good agreement with suggested model.

The effect of spin-orbit interaction is studied in 2DEG system at AlGaN/GaN interface. Effective g* factor of electrons in AlGaN/GaN 2DEG was found to be 3.7, 3.3, and 2.8 for LLs with n = 20, 21, and 22 respectively. The effect of weak antilocalization is studied in system structural inversion asymmetry. The fitting of experimental data gives value of Rashba constant 1.01×10^{-12} eVm.

These results should be taken into account for design of new devices with improved functionality and performance (i.e. ‘effective mass engineering’, spin-transistors).

Chapter 4. Reliability of AlGaN/GaN-based HEMTs

In this chapter the main results of AlGaN/GaN HEMTs performance and reliability investigation are presented and analyzed. Special attention is given to noise properties analysis and the study of possible origins of fluctuation phenomena in AlGaN/GaN HEMTs. The effects of device structure, thermal properties and environmental conditions (gamma radiation) on device performance are discussed in detail.

Operational parameters of HEMT and TLM devices

The basic structure of a high electron mobility transistor and conduction band diagram of the structure under the gate electrode are shown in Figure 4.1. In its simplest implementation, the structure consists of single barrier heterostructure with three electrical contacts. ‘Source’ and ‘Drain’ contacts are ohmic contacts to two-dimentional electron gas channel and ‘Gate’ is Schottky contact to the barrier. When DC bias is applied between source and drain contacts, the potential profile in the channel and current through the channel can be controlled by control by the gate potential. Typical transfer I-V characteristics are shown in Fig. 4.2 (a). The main operational parameters of HEMTs are transconductance, saturation current and pinch-off voltage.

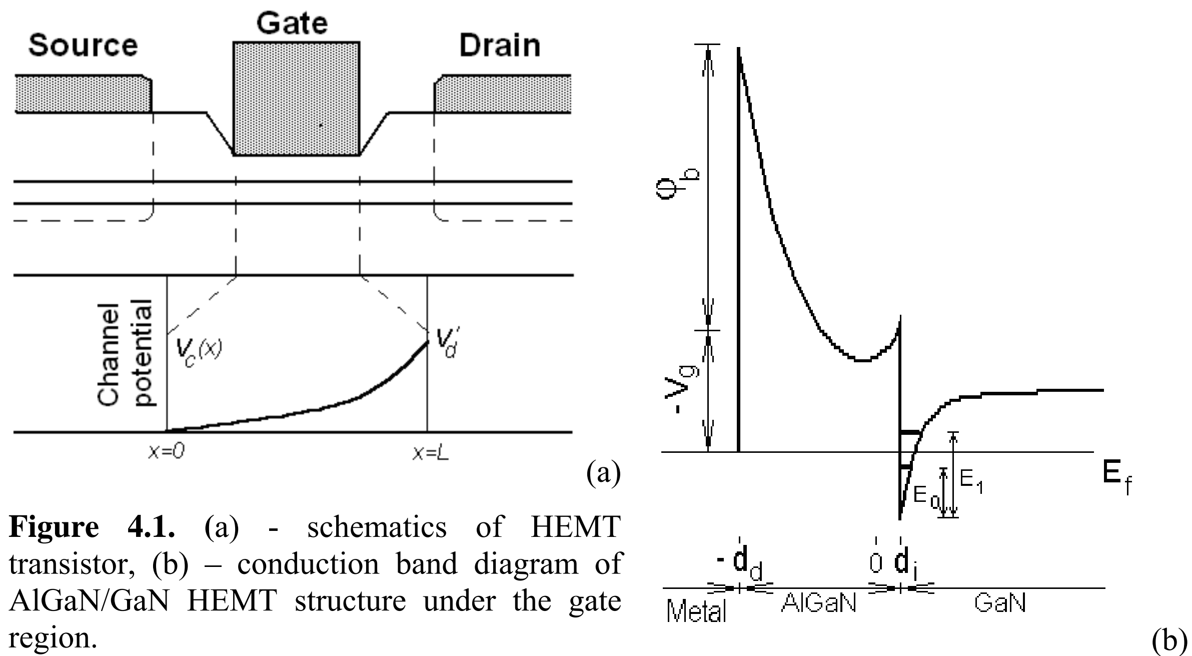

Figure 4.1. (a) - schematics of HEMT transistor, (b) – conduction band diagram of AlGaN/GaN HEMT structure under the gate region.

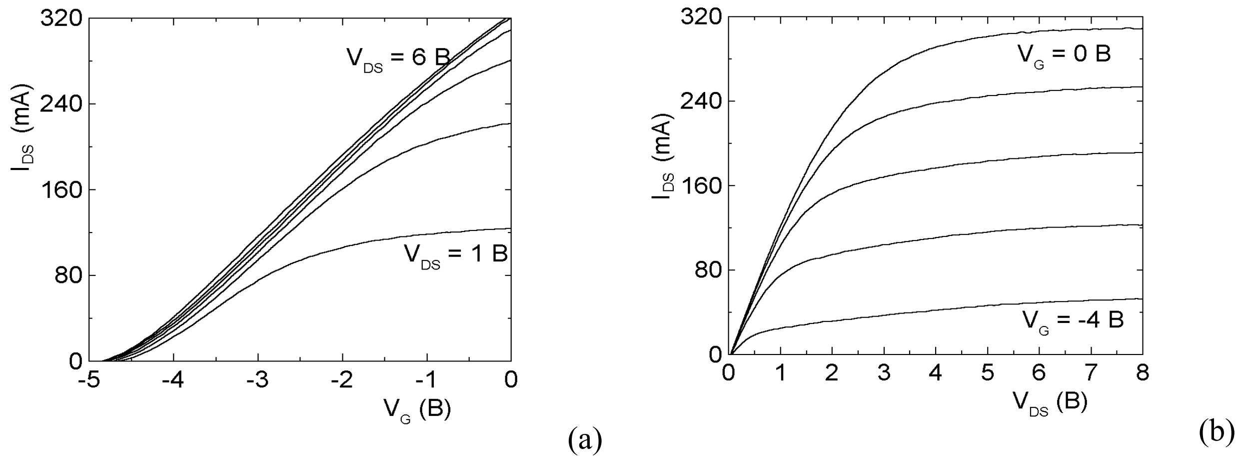

Figure 4.2. (a) – typical transfer current voltage characteristics of HEMT devices (sample #A), (b) – typical output IV of HEMT.

Knowing experimental DC current voltage characteristics allows direct evaluation of these parameters. The slope of linear region of the transfer I-V is transconductance, gate voltage at which linear fit of the transfer I-V intersects x-axis is pinch-off voltage. When one increases the source drain bias with fixed gate potential, the current through device or source-drain current increases almost linear and saturates at higher bias as shown on Fig. 4.2 (b).

Using these parameters allows to get important information about transport properties of the device structure (i.e. sheet carrier concentration, mobility).

As it is shown before [122], the carrier concentration under the gate of HEMT depends on gate voltage as

$$n_s = \frac{\varepsilon_{AlGaN}}{ed}(V_G - V_{off}) \tag{4.1.1}$$

where d – thickness of AlGaN barrier layer, ε_{AlGaN} is barrier permittivity, V_G – gate voltage,

$$V_{off} = \phi_b + \frac{1}{e}(E_{F0} - \Delta E_C) - \frac{eN_d d^2}{2\varepsilon_{AlGaN}} \tag{4.1.2}$$

where ϕ_b is Schottky barrier height, N_d is doping level in the barrier.

The transconductance of HEMT in saturation can be written as

$$g_m = \frac{W\varepsilon_{AlGaN}}{d} v_s \tag{4.1.3}$$

where W – channel width, v_s – electron velocity in the channel.

It should be noted that in reality the ohmic contacts in HEMT have finite resistance, and therefore part of source-drain bias is dropped on contact resistance. In any comprehensive investigation of HEMT performance the effect of contacts should be taken into account. In order to study effect of ohmic contacts and ungated regions of the structure on device performance the transmission line patterns are widely applied. Schematically TLM pattern is shown on Fig. 4.3.

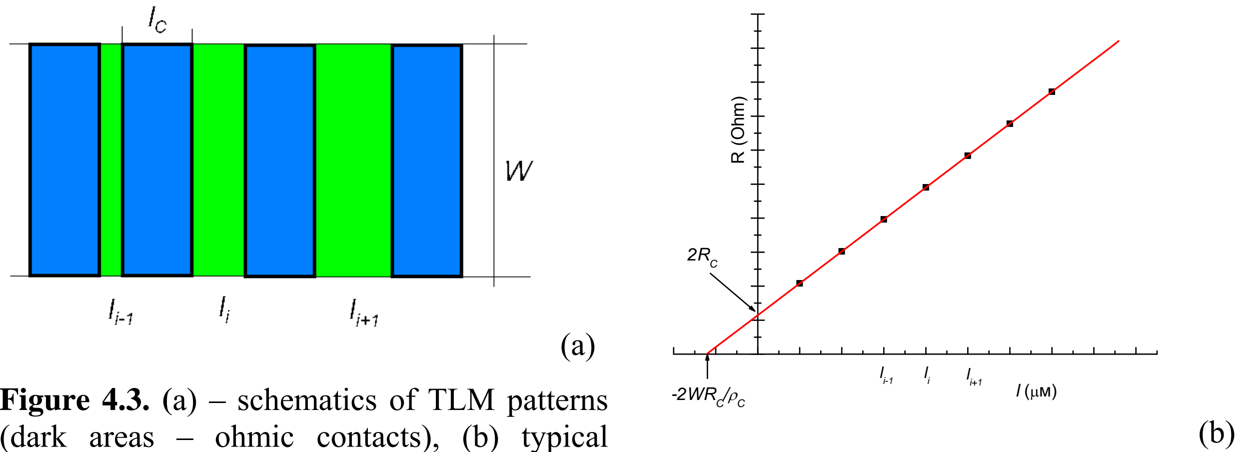

Figure 4.3. (a) – schematics of TLM patterns (dark areas – ohmic contacts), (b) typical dependence of total resistance of TLM pair on distance between contacts.

Generally, TLM pattern consist of a set of aligned ohmic contacts. The spacing between each pair of neighbor contacts is increased in some step from left to right (Fig. 4.3 (a)), i.e. $l_i<l_{i+1}$ for each i.

Current flow I through two neighbor contacts causes a voltage drop of

$$U = IR = I(2R_C + r_S \frac{l_i}{W}), \tag{4.1.4}$$

where R – total resistance, R_C – single contact resistance, W – channel width, l_i – contact spacing, r_s – sheet resistance.

Figure 4.3 (b) explains how contacts and sheet resistance can be evaluated from IV measurements of TLM patterns.

This technique was used in order to separate contacts and channel effects in AlGaN/GaN HEMT and TLM devices. It was found that ohmic contact resistance does not exceed 10% of total resistance of HEMTs. The monitoring of contacts resistances on different stages of investigation shows that the quality of ohmic contacts has a significant influence on device performance, which will be further discussed in detail.

Noise Characteristics

In this work the investigation of noise spectra was carried in order to get the information about fluctuation phenomena in AlGaN/GaN HEMTs, and additional data about electron traps dynamics in these systems. Thermal, shot, generation-recombination and 1/f noise models were used in analysis of peculiarities in observed noise spectra.

Fluctuation phenomena, also called as noise, occur in semiconductors due to the statistical nature of different physical processes in these materials. In general, when a quantity X shows noise we may write:

$$X(t) = \langle X \rangle + \Delta X(t) \tag{4.2.1}$$

The symbol $\langle X \rangle$ means averaging over a long period of time. Now $\Delta X(t)$ may be written in a Fourier series:

$$\Delta X(t) = \sum_i \left[a_i \exp(j2\pi f_i t) + a_i^* \exp(-j2\pi f_i t) \right] \tag{4.2.2}$$

where the coefficients a_i are fluctuating amplitudes. The noise component measured at a frequency f_i is then

$$\langle \Delta X_i \rangle = 0, \quad \langle (\Delta X_i)^2 \rangle = 2\langle a_i a_i^* \rangle \tag{4.2.3}$$

If we are measuring in a finite bandwidth Δf, the Fourier components inside the bandwidth add up quadratically. Such a noise, measured in a unit of bandwidth is called the spectral density. For a steady state process the value of spectral density is determined as follows:

$$S_X(f) = \lim_{T \to \infty} (2T \langle a_i a_i^* \rangle) \tag{4.2.4}$$

Here asterisk denotes the complex conjugate of the quantity involved.

Another basis parameter in noise theory is so called autocorrelation function $\varphi_x(t)$. $\varphi_x(t)$ describes how, on the average, a deviation $\Delta X(t_0)$ will decay. The autocorrelation function is defined by

$$\varphi_X(t) = \langle \Delta X(t_0) \Delta X(t_0 + t) \rangle \tag{4.2.5}$$

$\varphi_x(t)$ *and* $S_X(f)$ connectedby the Wiener-Khintchinerelations[134]:

$$S_X(f) = 4\int_0^\infty \varphi_X(t) \cos(2\pi f t) dt \tag{4.2.6}$$

$$\varphi_X(t) = 4\int_0^\infty S_X(f) \cos(2\pi f t) df \tag{4.2.7}$$

These equations are used when making a physical model for an observed noise.

There are three well understood types of noise that are frequently seen in noise spectra: thermal noise, shot noise and generation-recombination noise.

(a) Thermal noise.

The statistical nature of the scattering of free charge carriers causes random changes in their velocities and, hence, random microscopic diffusion currents. In equilibrium situation this motion has an average energy of $\frac{1}{2}kT$. As a result, a fluctuating current that is equal to the sum of these microcurrents exists in semiconductor samples and a fluctuating voltage is observed at their electrical contacts (Brownian motion noise). Under thermal equilibrium conditions, this noise is called thermal noise or Johnson noise. In a more general case it is called diffusion noise.

In terms of resistance it means that any resistance R shows spontaneous current fluctuations or voltage fluctuations governed by the equations:

$$S_I = S_V / R^2 = 4kT / R \tag{4.2.8}$$

This white spectrum is always found, whatever the nature of the conduction process, or the nature of the mobile charge carriers. Thermal noise is generated in any dissipative physical resistor.

(b) Shot noise.

Charge transfer in semiconductor often connected with overcoming of different potential barriers. For example, electrons emitted from a hot cathode in a vacuum diode, or electrons, crossing potential barrier in heterostructure - these carriers are randomly generated. Random generation leads to fluctuation around the average current I:

$$S_I = 2eI \tag{4.2.9}$$

It worth to note that shot noise is a non-equilibrium phenomenon associated with current flow in a driven stationary state. The spectrum is white at all attainable frequencies because of the very high transit time of the electrons.\

(c) Generation-Recombination (GR) noise.

The number of free electrons in the conduction band may fluctuate because of generation and recombination processes between the band and traps. The appearance and disappearance of carriers in a semiconducting sample by the processes of generation and recombination is described by a differential equation [135]:

$$-\frac{d\Delta N}{dt}=\frac{\Delta N}{\tau} \tag{4.2.10}$$

where ΔN is the fluctuation in the number of carriers and τ is the lifetime of added carriers.

The Wiener-Khintchine theorem (Equations (4.2.6)-(4.2.7)) gives for GR:

$$S_N(f)=\left\langle(\Delta N)^2\right\rangle\frac{4\tau}{1+(2\pi f\tau)^2} \tag{4.2.11}$$

This type of spectrum is called Lorentzian. If there is only one type of trap, then the variance $<(\Delta N)^2>$ is given by:

$$\frac{1}{\left\langle(\Delta N)^2\right\rangle}=\frac{1}{N}+\frac{1}{X_n}+\frac{1}{X_p} \tag{4.2.12}$$

where X_n is the average number of occupied traps and X_p the average number of empty traps. The variance thus approximates the smallest of the quantities N, X_n and X_p.

(d) 1/f Noise.

There is, however, another type of noise that is often seen on spectra but did not have simple unified theory behind. It is *1/f* noise - fluctuation in the conductance with a spectral density proportional to f^{γ}, where $\gamma = 1.0 \pm 0.1$ in a wide frequency range, usually measured in the range from 1Hz to 100 kHz. It is clear that the spectrum $\frac{S_I}{I^2}\sim\frac{1}{f}$ cannot be exactly *l/f* the whole range $0<f<\infty$. Firstly, $S\to\infty$, when $f\to 0$. Also, the integral of $S\to\infty$ at both frequency limits $f\to 0$ and $f\to\infty$. Therefore, if noise is stationary the spectrum must flatten below a certain low frequency and it must become steeper above a certain high frequency. Neither of these frequency limits has ever been observed. High frequency limit is masked by thermal noise usually and practically not reachable. For low frequency limit observation two solutions are

possible: (a) the noise is not stationary, or (b) we must measure at still lower frequencies. Second choice is hard to perform, as measurements at frequencies around 10^{-6} Hz will need around a month to be completed.

Unlike the first three sources mentioned above, which are well understood, the origin of the *1/f noise* is still open to debate [136,137]. At the moment, two theoretical approaches to describing the 1/f noise are discussed: the McWorter and Hooge models. The main physical difference between these two cases is the origin of noise sources. McWorter's model of the noise deals with surface or interface noise sources (fluctuations of concentration Δn), with noise spectral density of

$$\frac{S_I(f)}{I^2} = \frac{N_{te}}{N^2 A \ln(\tau_2 / \tau_1)} \frac{1}{f} \tag{4.2.13}$$

where N_{te} – number of traps which can capture electrons, N – total number of traps, A – interface area, in assumption of uniformly distributed traps with capture time varied in the range from τ_1 to τ_4.

While Hooge's model takes into consideration the distribution of noise sources in the volume (mobility fluctuations, $\Delta\mu$) [138] and empirical spectral density

$$\frac{S_R}{R^2} = \frac{\alpha}{Nf} \tag{4.2.14}$$

where N – total number of traps, a – Hooge constant.

The question whether Δn or $\Delta\mu$ is responsible for current fluctuations in HEMTs even in the case of equilibrium (low voltage) noise still remains open.

Low-Frequency Noise

In this work the noise spectra of HEMTs were measured in the frequency range of 1Hz – 100kHz in the transistor's linear operating regime. At drain-source voltages of up to 100 mV the current-voltage characteristics demonstrate a linear dependence. The linearity is also conserved when the temperature is reduced to 45 K. The channel resistance decreases with decreasing temperature mainly due to the growth of mobility because the carrier concentration remains practically unchanged. The noise and high-frequency conductivity were measured with a Hewlett-Packard noise figure meter HP 8970B.

Typical current noise spectra of HEMT devices (sample #A) measures at different are shown in figure 4.4.

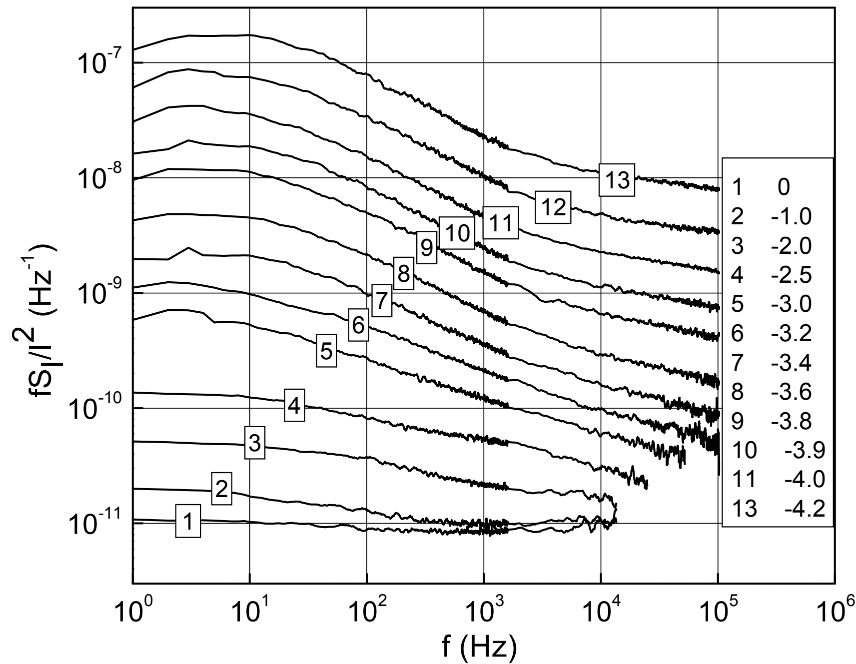

Figure 4.4. Normalized current noise spectra measured at room temperature and different gate voltages. Gate length is 250 nm, spacing between source and drain is 3μm, V_{DS}=100mV.

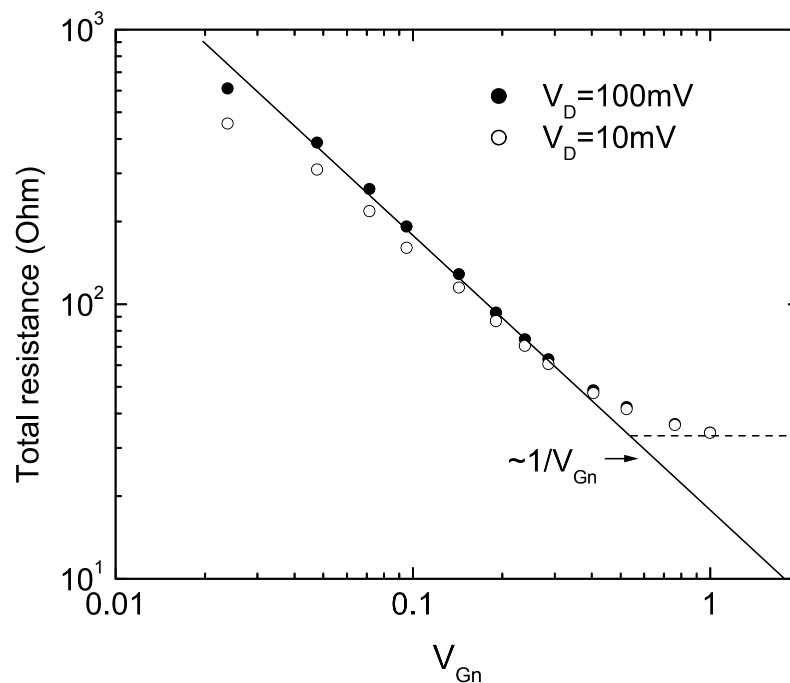

Figure 4.5. Total resistance of the channel as a function of normalized effective gate voltage. Symbols are experimental data obtained at V_{DS}=10 mV (open circles) and V_{DS}=100 mV (solid circles). T = 300 K. The solid line shows $1/V_{Gn}$ dependence, and the dashed line determines invariable background (resistance of passive region).

In the linear regime, the total resistance of the channel demonstrates an inversely proportional dependence on gate voltage, V_G. It is convenient to use normalized effective gate voltage to threshold voltage, V_T: $V_{Gn} = (V_G - V_T)/|V_T|$, and present the total channel resistance as a sum: $R = R_p + R_a$, where R_p comprises the resistance of that part of the channel outside the gate metallization (passive region), R_a is the resistance under the gate (active region).

Measurements of transmission line model (TLM) structures showed that contacts did not contribute much to the total resistance (10% of total resistance) and their influence can be neglected. As seen in Fig.4.5, the total resistance follows $1/V_{Gn}$ dependence fairly well. Because the gate voltage affects the active region only, the changes in R are due to the changes in R_a. Deviations are observed only at very small negative gate voltages, where $R_a << R_p$ and the total resistance approaches the invariable background (total resistance of the channel at $V_G = 0$), and at gate voltages close to pinch-off, where changes in carrier mobility should be expected due to the hot electron effect in the strongly non-uniform high electric field.

In order to analyze the features observed in the noise spectra we assume the noise sources in the passive and active regions of the channel are uncorrelated. In this case the following expression for the current noise density can be written [139]:

$$\frac{S_I}{I^2} = \frac{S_R}{R^2} = \frac{S_{Ra} + S_{Rp}}{R^2} = \frac{\alpha_a e\mu R_a^3}{L_a f (R_a + R_p)^2} + \frac{\alpha_p e\mu R_p^3}{L_p f (R_a + R_p)^2} \tag{4.2.15}$$

where α, μ, L are a Hooge parameter, carrier mobility and channel length, respectively, e is electronic charge, subscripts a and p correspond to active and passive regions. The ratio of the resistance and power of noise in active and passive regions will determine the effect of the gate voltage on the current noise density. If the gate region dominates, i.e. $R_a >> R_p$, $S_{Ra} >> S_{Rp}$ and taking into account the dependence $R_a \sim 1/V_G$, Eq. (4.2.15) easily transforms to

$$\frac{S_I}{I^2} = \frac{S_{Ra}}{R_a^2} \sim \frac{1}{V_G} \tag{4.2.16}$$

In the opposite case, when the passive region dominates, i.e. $R_a << R_p$, $S_{Ra} << S_{Rp}$, the current noise density is expected to be constant. Two other cases concern intermediate conditions. If the noise source of the active region remains more powerful ($S_{Ra} >> S_{Rp}$), while its resistance is much smaller than R_p, Eq. (4.2.15) yields the following approximation

$$\frac{S_I}{I^2} = \frac{S_{Ra}}{R_p^2} \sim \frac{1}{V_G^3} \qquad (4.2.17)$$

And finally, at large negative gate voltages close to pinch-off, where $R_a >> R_p$ and assuming that resistance fluctuations are determined by the passive region ($S_{Ra} << S_{Rp}$) we obtain

$$\frac{S_I}{I^2} = \frac{S_{Rp}}{R_a^2} \sim V_G^2 \qquad (4.2.18)$$

A comparison of the experimental data plotted in Fig.4.6 with the approximations presented above shows that in the entire range of the gate voltages the cases described by Eqs. (4.2.16) and (4.2.18) are the most realistic. The latter allows us to conclude that in spite of the large ratio of L_{SD}/L_G, the active region of the device is the main contributor to the observed low frequency noise. It should be noted that when speaking about the active region, we include not only part of the conducting channel under the gate, but also adjacent parts of the source-to-gate and gate-to-drain regions.

It is seen from Fig.4.6 that it is the threshold gate bias, $V_{Gt} \approx -3V$, which distinguishes different regimes of the transistor operation with weak and strong control of the channel resistance.

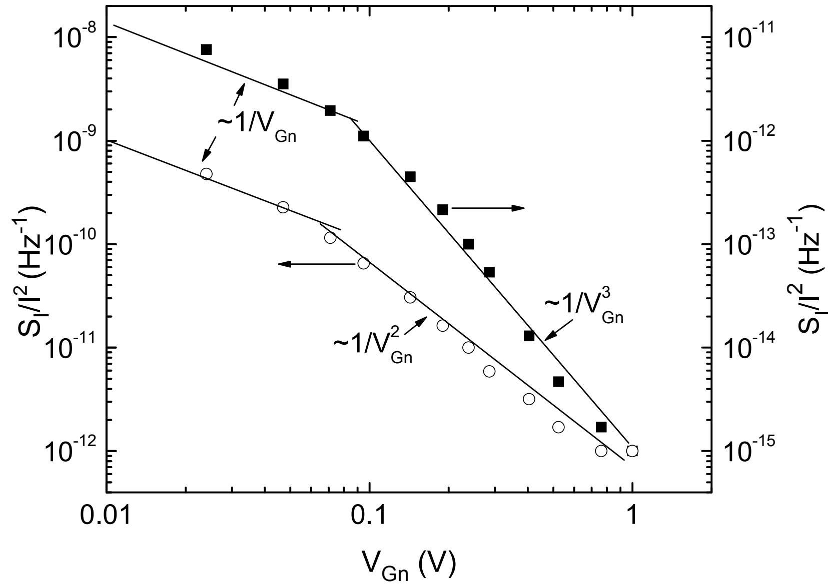

Figure 4.6. Dependences of current noise density on normalized effective gate voltage. Symbols are experimental data obtained at 10 Hz (open circles) and 10 kHz (solid squares). T = 300 K. The solid lines show for convenience different power dependences on gate voltage.

Also it should be noted that conventional generation-recombination processes cannot explain the behaviour observed [140]. It seems that a model based on dynamic redistribution of lateral potential along the conducting channel is more relevant. A static approach to such redistribution has been developed in [141].

The authors of [142] also propose a model based on the existence of lumped-thermal-noise generators along the semiconductor-air or semiconductor-dielectric protection interface. It is assumed that additional conductive channel is located either on the surface or in the barrier layer at a short distance from the basic two-dimensional gas (2DEG) channel. Between the 2DEG and additional channels strong electrostatic coupling should appear. At high enough electric fields (at large gate voltage the electric field in the active region approaches several kV/cm), the difference in lateral distribution of the potential in the basic and additional channels leads to charge redistribution in the additional channel. The latter should determine the redistribution of the transverse potential that supports 2DEG in the basic channel. As a result, lateral distribution of electron density in the basic channel is changed. In the proposed model, intrinsic density fluctuations in the 2DEG play the role of dynamic inhomogeneities. These fluctuations are associated with electrons in the additional channel which pull them along. At low frequencies this effect causes "slow" electrons of the additional channel to contribute to 1/f noise together with "fast" electrons of the basic channel, which causes an increase of the 1/f noise level. At high frequencies, "slow" electrons of the additional channel cannot respond to fast fluctuations of the 2DEG. In this case, there is no extra contribution to the 1/f noise. Thus, from analyses of the noise spectra, one can conclude that the low-frequency part of the 1/f noise contains high-frequency "fast" electron fluctuations, which are caused by dynamic potential redistribution at certain gate voltages in basic and additional channels.

Middle Frequency Range Investigation

The investigation of fluctuation phenomena of the HEMT structure in a wide range of applied electrical fields is an important issue because its noise is up-converted to the high-frequency noise in the oscillator circuit, and therefore the MHz frequency range plays a crucial role.

For detailed analysis of the noise origin in the frequency range from 10 to 100 MHz two equivalent approaches were used: expressing noise through noise temperature as well as through the resistance fluctuation model. Additionally, self-consistently calculated potential profiles of the structure at different voltages were analyzed.

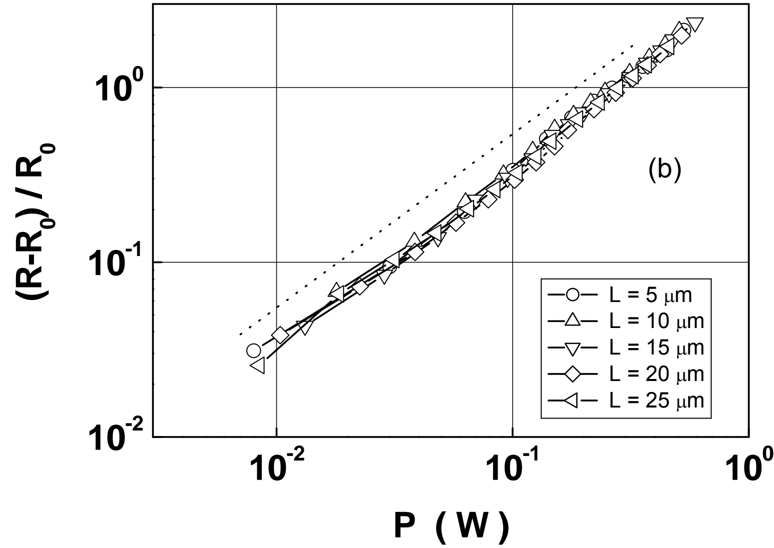

Figure 4.7. The relative change of resistance of TLM structures of the samples of different lengths measured as a function of dissipated power. Dashed line shows approximation slope.

As it was also shown [71], the dependence of the relative change of resistance on dissipated power $P = IxU$ is linear (Fig.4.7) and coincides for samples of different lengths. Assuming that the increase of temperature is proportional to the dissipated power one can conclude that the change of resistance of the sample is proportional to the change of temperature. This fact will be used in later analysis.

Spectral density of voltage fluctuations $S_V^{'}$ was extracted from the measured noise figure using equation:

$$F = 10\log\frac{S_V^{'} + S_{V0}}{S_{V0}}, \qquad (4.2.19)$$

where $S_{V0} = 4kT \cdot 50$ – is the thermal noise of the 50 Oohm impedance waveguide, k – is the Boltzmann constant, T – is the temperature. It should be noted that the noise of the noise figure-meter device is excluded. Typical voltage noise results, measured at frequency f = 90 MHz for HEMT structure patterned with TLM contacts of different lengths from 5 to 25 μm versus applied voltage are shown in Fig.4.8. The observed noise behavior correlates with the non-linearity of the current-voltage characteristics.

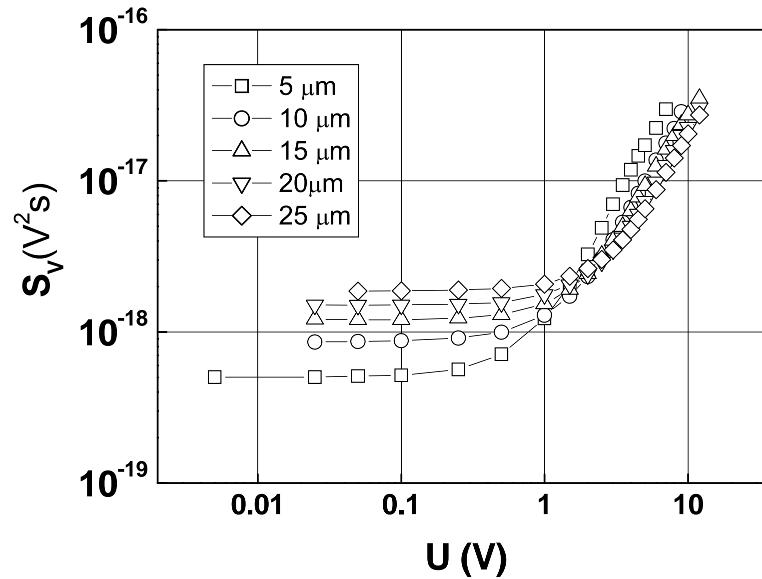

Figure 4.8. Voltage noise spectral density, measured at frequency f = 90 MHz for TLM structures of different lengths versus applied voltage.

To analyze the obtained noise results obtained we considered three possible mechanisms of noise origin. Noise in the range from 10 to 100 MHz can contain an equilibrium thermal (Nyquist) noise. It may also contain diffusive noise of hot electrons and excessive current noise, caused by generation-recombination processes. Below we consider each of the above-mentioned mechanisms in detail.

The origin of the observed noise as a thermal noise will be discussed first. For the investigated voltage range, we consider that the shape of the electron distribution function does not change under applied biases. In this case, the temperature of the two-dimensional electron gas coincides with the lattice temperature and the thermal noise spectral density is determined by the formula (4.2.8). The resistance of the sample in the case of self-heating can be determined as:

$$R = R_0 + \Delta R \tag{4.2.20}$$

where R_0 – resistance without self-heating effect, ΔR – resistance deviation due to heating effect. Taking into account the linear dependence of the relative change of the resistance vs dissipated power the resistance and the temperature of the sample can be described as:

$$R = R_0 + k_1 P \tag{4.2.21}$$

$$T = T_0 + k_2 P$$

where k_1 and k_2 are constants. Then the thermal noise can be written as:

$$S_V = 4k(T_0 + k_2 P)(R_0 + k_1 P). \tag{4.2.22}$$

The equation after normalization to R_0 (obtained by extrapolation of R to $V = 0$) will be represented in the following form:

$$\frac{S_V}{R_0} = 4k\left[T_0 + \left(\frac{k_1}{R_0}T_0 + k_2\right)P + \frac{k_1}{R_0}k_2 P^2\right] \tag{4.2.23}$$

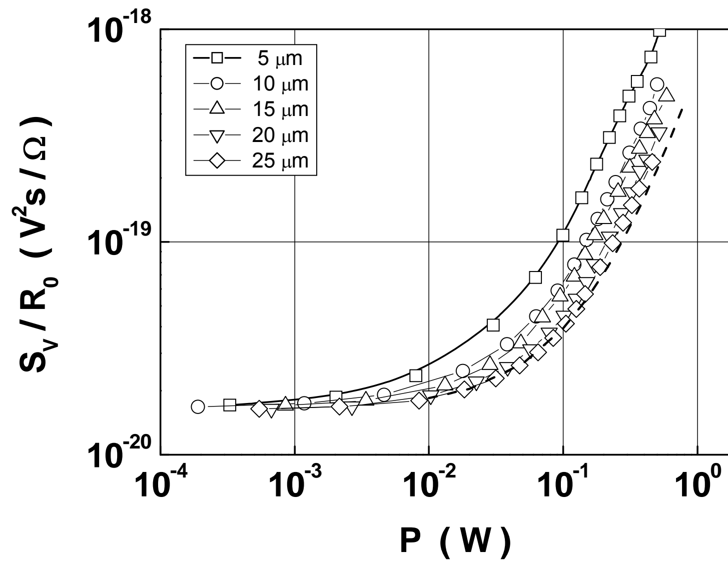

Figure 4.9. Spectral density of noise fluctuations as a function of dissipated power, measured for samples with of different lengths. Dashed curve corresponds to the theoretical curve accordingly to Eq. (4.2.23) for the sample with a length of 25 μm.

The value of k_1/R_0 equal to $3.67\ \mathrm{W}^{-1}$ is the same for all samples due to the coincidence of the curves shown in Fig. 4.7, corresponding to the samples of different lengths. Accordingly to the Eq.(4.2.23) $S_V(P)$ contains three terms: constant level term $S_{V0} = 4kT_0R_0$, linear term and term with quadratic vs power dependence. In Fig. 4.9 are shown shows the theoretical dependence (4.2.23) calculated for the sample with a length of $L = 25\ \mu\mathrm{m}$ and the experimentally obtained relative noise increase as a function of the power for a frequency of $f = 90$ MHz. From

the coincidence of the fitting curve to the experimental data the coefficient k_2 is extracted to be equal:equal to $k_2 = 2200\,\mathrm{KW}^{-1}$.

As one can be seen, even if we assume that dissipated power is about 1W, then the overheating value is $\Delta T = 2200\,\mathrm{K}$ (which is definitely much larger than any experimental evaluations), the value of the measured noise is still higher than the calculated noise. Moreover, the experimental dependences for samples of different lengths do not coincide as it should follow from equation (4.2.23). Therefore, we can conclude that the observed noise cannot be the thermal noise.

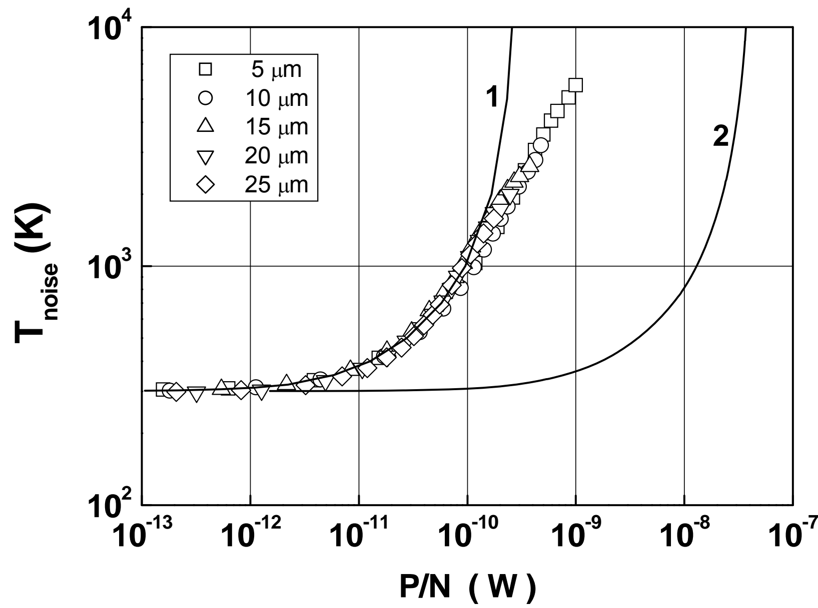

Figure 4.10. Noise temperature dependence on dissipated power per one electron measured for samples with of different lengths. Theoretical dependencies calculated accordingly to Eq. (4.2.24) calculated for $\tau_{ph} = 50\,\mathrm{ns}$ (curve1) иand $\tau_{ph} = 350\,\mathrm{fs}$ (curve 2) are shown by lines.

Let us now analyze the results within the model of diffusive hot electron noise, driven by the scattering of hot electrons on phonons [143]. For this we shall represent our measured noise in terms of noise temperature (experimental points in Fig.4.10) and build the dependence of the noise on power applied to one electron. In the same coordinates we shall plot the value of hot electron noise, calculated with the empirical formulae [143], that takes into account phonon scattering:

$$P_s = \Delta\varepsilon / \tau_{ph} \{\exp(-\Delta\varepsilon / kT_n) + [\exp(-\Delta\varepsilon / kT_n) - 1] / [\exp(\Delta\varepsilon / kT_L) - 1]\}, \qquad (4.2.24)$$

where $\Delta\varepsilon = 0.09\,\text{eV}$ - is the energy of the optical phonon, $T_L = 300\,\text{K}$ - is the lattice temperature, T_n - is the noise temperature, P_s – is the dissipated power per one electron. Curve 2 corresponds to the typical value of phonon time $\tau_{ph} = 350\,\text{fs}$ [144]; curve 1, that which partially coincides with the experimental points, corresponds to $\tau_{ph} = 50\,\text{ns}$, which is much higher than the value commonly used for GaN-based structures. Consequently, the hot electron noise also cannot explain the observed results either.

The third possibility: measured noise is generation-recombination (G-R) noise. This is determined by the formula (4.2.11). Let us assume that the investigated frequency $f = 90\,\text{MHz}$ lies within a region where $2\pi f\tau << 1$. Then expression (4.2.11) can be written as:

$$\frac{S_I N}{I^2} = 4g\tau \qquad (4.2.25)$$

where $\overline{\Delta N^2}/N = g$.

The right side of (4.2.25) does not depend on sample size but can depend on temperature (dissipated power). Therefore we shall build a dependence of the left side of (4.2.25) on dissipated power, taking into account that a number of electrons, N, are proportional to length of a sample L. Since, as stated above, the temperature of the sample is determined solely by dissipated power, the curves obtained for different lengths should coincide (due to coincidence of corresponding resistance-power characteristics for different sample lengths).

As the thermal noise is always present at the non-zero temperature, we should subtract value $S_{V0} = 4kT_0R$ from the analyzed spectra. As a result we obtain dependence of value $L(S_V - S_{V0})/I^2R^2$ on dissipated power $P = UI$ (Fig.4.10).

Additional thermal noise $S_{VT} = 4k(T - T_0)R$ under condition $T - T_0 = k_2P$ (as explained above) equals:

$$S_{VT} = 4kk_2I^2R^2 \qquad (4.2.26)$$

In the coordinates of Fig.4.11:

$$\frac{LS_{VT}}{I^2R^2} = 4kk_2L \qquad (4.2.27)$$

At k_2 = 1200 K/W $k_2 = 1200\,\text{K/W}$ (the extraction procedure for this coefficient will be described below) and $L = 25\,\mu\text{m}$, $4kk_2$L = 1.66x10^{-22} cm·s can be obtained. The value is much

lower then the measured level of noise. At smaller lengths the value will be only be lower, thereforeso that this additional thermal noise can be neglected.

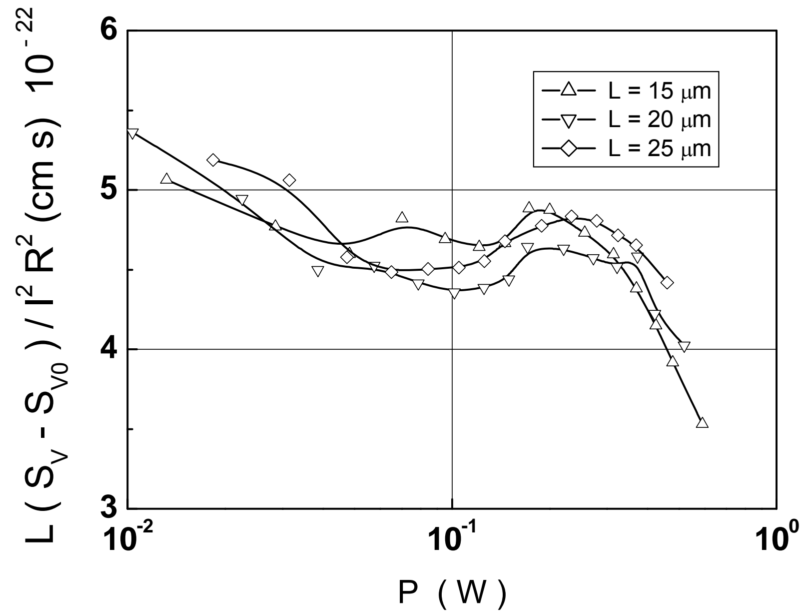

Figure 4.11. Dependence of normalized noise of samples of different lengths on dissipated power at f = 90 MHz.

It is seen from Fig.4.11 that not only do the curves for $L = 25, 20, 15\,\mu\text{m}$ coincide well at low power, but also the position and shape of the special feature observed at high power in the range from 0.1W to 0.6 W coincide with the maximum at $P \approx 0.25\,\text{W}$. This feature confirms our assumption of the G-R character of the observed noise.

Two kinds of transport mechanisms in two-dimensional electron channels may be responsible for generation-recombination noise. The first one is electron redistribution due to the presence of electrons on more than one quantum level with different mobility. In this case, spontaneous transitions between the levels lead to fluctuations of the total conductance of the channel. This model was used in [145] to explain excessive noise at $f = 10\,\text{GHz}$. The second reason for the G-R noise can be as a result of the penetration of the 2D electron wavefunction to the barrier region of the structure, where the concentration of traps is generally higher. The mobility of these electrons is therefore reduced due to interaction with the traps.

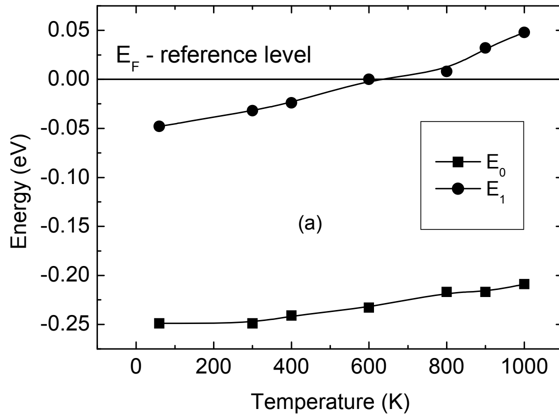

Figure 4.12 (a). Dependence of position of ground and first exited level in 2DEG.

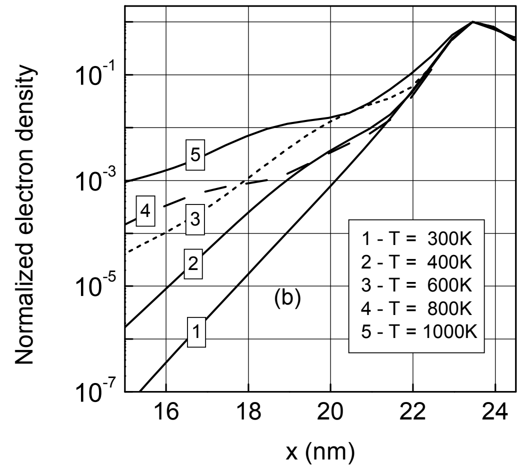

Figure 4.12 (b). Distribution of density of 2DEG in the direction perpendicular to the interface at different temperatures. The interface position is at 23nm in the calculation.

To analyze the influence of the first suggested mechanism of GR noise we self-consistently calculated the potential profile of the structure at different temperatures. The positions of the ground and first excited quantum levels in 2DEG relative to the Fermi energy calculated for different temperatures are shown in Fig.4.12 (a). It is interesting to note that at $T \approx 600\,\mathrm{K}$ the position of the first excited level coincides with the Fermi energy. According to the theory of GR noise, the temperature dependence of equation (4.2.25) should have a maximum at this point. Indeed, in Fig.4.11 we observe such a maximum at $W \approx 0.25\,\mathrm{W}$, which allows us to ascribe this noise feature to the fluctuation of the number of electrons at the first excited quantum level. Now we can estimate the value of k_2: $k_2 = \Delta T/P = 300\mathrm{K}/0.25\,\mathrm{W} = 1200\,\mathrm{K/W}$. This value is much smaller than $k_2 = 2200\,\mathrm{K/W}$ used in our analysis of the influence of thermal noise (Fig.4.9) and can serve as further evidence of the negligible role of equilibrium thermal noise in the total measured noise spectra.

To evaluate the role of the second reason mentioned above for excessive noise in the structure we plotted electron density normalized to a maximum (in the ground level of 2DEG) as a function of coordinate *x*, perpendicular to the 2DEG layer (Fig.4.12 (b)). Increasing the temperature leads to a rise of electron density within the barrier layer (x<23nm). This rise should lead to an increasing of number of electrons with lower mobility and, consequently, to an increase in the noise caused by an exchange between fast and slow electron populations. But, as is seen from Fig.4.11, the total noise of the structure does not increase with temperature

(dissipated power). Therefore this model cannot be used to explain the results of noise measurements at $f = 90\,\mathrm{MHz}$.

A similar analysis was carried-out for noise results obtained at 20 MHz frequency. The temperature dependence of equation (4.2.25) was also found to coincide for samples of different lengths (Fig.4.13 (a)), but in this case the character of the dependence differs from the results obtained at $f = 90\,\mathrm{MHz}$.

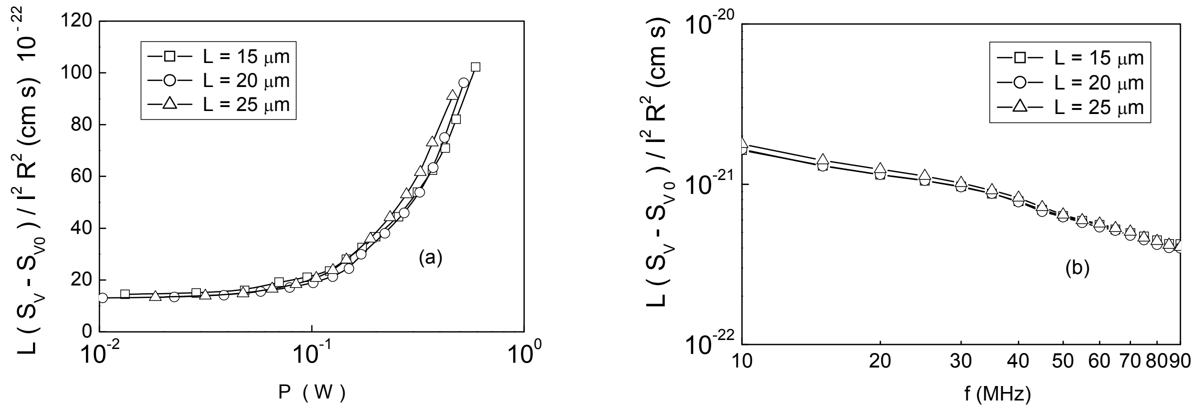

Figure 4.13 (a). Dependence of normalized noise of samples of different lengths on dissipated power at $f = 20$ MHz

Figure 4.13 (b). Normalized noise spectra of TLM samples of different lengths measured at dissipated power P = 0.3 W.

Our analysis shows that the noise also has a generation -recombination character, but of different origin. The frequency dependence of noise measured at a dissipated power of 0.3W (Fig.4.13 (b)) shows non-zero frequency slope, which can be analyzed as a spectrum combined from two noise components. The first one is a high-frequency component described above for $f = 90\,\mathrm{MHz}$. The second one is at lower frequencies, with a corner frequency of around $f_0 = 50\,\mathrm{MHz}$, which corresponds to the time constant $\tau = 3.2\,\mathrm{ns}$. This component can originate from the increase in the population of electrons in the barrier region of the structure with temperature (Fig.4.12 (b)). This model can explain the effect of increasing noise at 20MHz with a rise of dissipated power and, correspondingly, with an increase of temperature (Fig.4.13 (a)).

Radiation Effect on Transport and Structural Properties of AlGaN/GaN heterostructures

The amount of radiation that semiconductor devices and materials encounter during their lifecycle strongly depends on the radiation environment and their operating conditions. For space missions and military applications it is obvious that there is a radiation-harsh environment. However also during their fabrication process and even for standard terrestrial operation the devices may suffer from ionizing radiation.

In general. one can differentiate between the following different environments

- Space
- High-energy physics experiments
- Nuclear
- Natural environments
- Processing-induced radiation

Each of these environments is characterized by its own spectrum of particles and energy distribution. There may be an interaction between the different environments as for instance the inherent built-in damage during the device fabrication may impact the device performance during a space mission. The fabrication of modem semiconductor devices relies on a great number of processing steps which can introduce radiation-damage. Typical examples are ion implantation, dry etching, resist stripping. e-beam or X-ray lithography, plasma enhanced chemical vapor deposition, ion milling, sputtering of barriers and metal layers etc. Although the degree of introduced damages in processing is much lower than for the other radiation environments mentioned above, the state-of-the-art GaN-based devices are very sensitive to damages during processing. This is critical in the case of ultra-thin gate dielectrics and spacer oxides.

In this work ^{60}Co gamma-source with flux of 100 rad/sec is used for investigation of radiation effects in AlGaN/GaN based device and structures. The temperature in active zone of irradiation does not exceed 40 ^{o}C.

In order to estimate the radiation hardness of AlGaN/GaN based heterostructures few samples were subjected to gamma-ray irradiation. The influence of gamma radiation on operational parameters of transistors was monitorted with I-V measurements of HEMT right after irradiation. It was found that that despite of significant degradation in device performance (in some cases, devices only showed 50% of their initial performance levels) at very high doses of gamma radiation ($2x10^9$ Rad), they were still operating. (It should be noted that according to literature HEMTs based on GaAs experience catastrophic failure at doses of gamma radiation as

high as 6x10^8 Rad.) The most astonishing effect of gamma radiation is the improvement of HEMT operational parameters and a significant decrease in their dispersion over the wafer under doses lower than 10^6 Rad (Fig. 4.14).

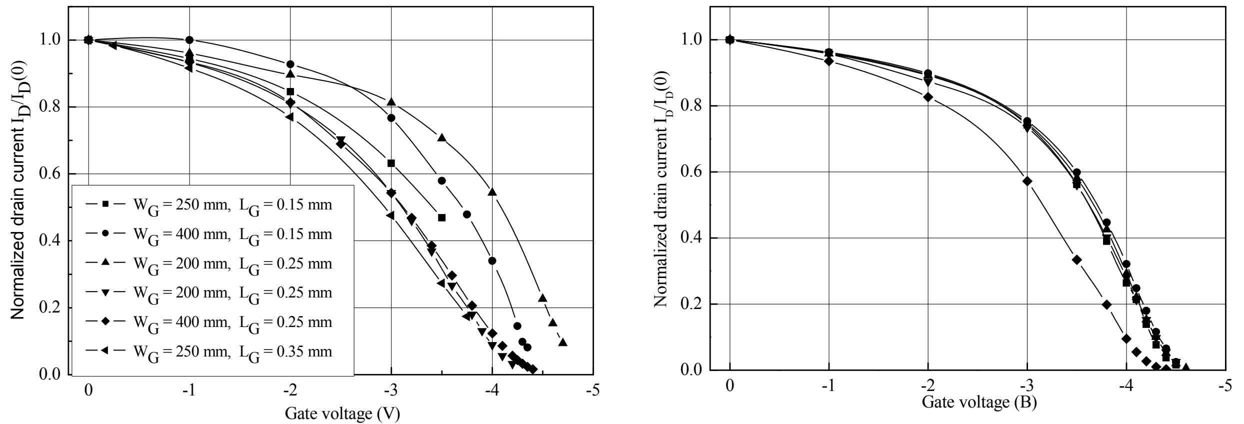

Figure 4.14. Normalized transfer characteristics for set of pre-irradiated (left) and irradiated at 10^6 rad (right) HEMTs. Source-drain bias 100 mV, room temperature.

Irradiated structures were studied at low temperatures in order to prove radiation stimulated improvement effect on low-temperature transport properties. Magnetotransport measurements were performed in a wide temperature range *T*=(0.3-300) K and in magnetic fields up to 10 T using standard low frequency (17 Hz) lock-in techniques. Measurements are typically made with a current modulation of 100 nA to prevent heating effects. From Shubnikov-de Haas (SdH) oscillation period sheet concentration of the 2DEG was determined. The effective mass was calculated from temperature dependence of the amplitude of the SdH oscillations. All parameters of the samples under study required for further analysis are summarized in Table 4.1.

Table 4.1.

Sample	E_F (meV)	n_s (10^{13}, cm^{-2})	m_F^* (m_0)	τ_q (fs)	μ (cm^2/V.s) (0.35K/300K)
#D before irradiation	131	1.02	0.20±0.01	79	5100/1260
#D after irradiation	128	1.0	0.20±0.01	410	28700/1350
#E before irradiation	129	1.01	0.19±0.01	90	11500/1850
#E after irradiation	123	0.96	0.19±0.01	350	19600/2000

There is no significant difference in the carrier concentration of different samples measured at low- (Hall effect) and high- (SdH oscillations) magnetic fields. This result indicates that the electrons occupy only the lowest subband. The most striking result obtained for samples #D and #E is the gigantic amplification of SdH oscillation amplitude after irradiation to 10^6 Rad.

The results of the electrical characterization of the structures obtained before and after irradiation can be resumed as follows: the carrier concentration is slightly decreased after an irradiation dose of 10^6 Rad, while the low-temperature 2DEG mobility exhibits a considerable increase. The minor changes in carrier concentration observed under visible relaxation of the AlGaN layer are less expectable. It is known that the most peculiar feature of nitride heterostructures is the presence of huge spontaneous and piezoelectric polarization fields. As a consequence, a high-density two-dimensional electron gas appears at the AlGaN/GaN interfaces even without doping. Any changes in polarization fields will cause changes in 2DEG concentrations. If the expected decrease of the piezoelectric contribution does not affect the carrier concentration two reasons should be considered. The first, the decrease of the piezoelectric field is minor under the observed strain relaxation. The second, the variation of surface charge compensates the decrease of the piezoelectric field to provide the same carrier concentration before and after irradiation.

The onset of oscillations as well as their amplitude is determined by the degree of disorder broadening of the developing Landau levels (LLs), and in addition to zero-field mobility, can be used for the estimation of material quality. Thus, the observed amplification of SdH oscillation amplitude (Fig. 4.15) together with the increase of the average time between scattering events, known as the quantum scattering time τ_q, strongly support the conclusion concerning the carrier mobility enhancement due to native defect ordering as is supporting by the structural characterization.

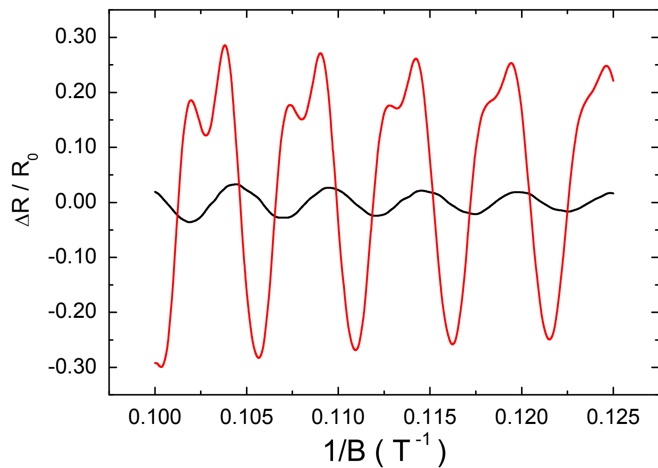

Figure 4.15. High magnetic field part of the magnetoresistance for sample #E. Light and Dark lines correspond to irradidiated and pre-radiated sample, respectively.

The structural characterization of the heterostructures was performed by X-ray diffraction (XRD) and secondary ion mass spectroscopy (SIMS). To gain insight into the structural transformation of the heterostructures during irradiation the angular distribution of the X-ray diffraction corresponding to the (0002), (0004), (10-12), and (-1-124) reflections of GaN and AlGaN layers was measured by means of triple-crystal differential diffractometry (PANalytical X'Pert MRD) under conditions of symmetrical and asymmetrical Bragg- and Laue-geometry. The shift of the peak corresponding to (0004) plane of AlGaN to lower angle is observed after irradiation. This change in spectra clearly indicates a strain relaxation in the AlGaN layer after irradiation. To prove this statement direct measurements of the elastic strain in the heterostructures were carried out. An integrated method for measuring surface curvature was used [146]. The results of these measurements for sample #A are presented in Fig.4.16.

It is seen that strain relaxation occurs up to doses of 10^6 Rad. It should be noted that strain relaxation in HEMT structure can result in generation of extra-defects or native defects compensation and structural ordering. The observed room temperature mobility improvement (1380/1460 initial and irradiated up to 10^6 Rad) indicates that the latter is dominating during radiation stimulated relaxation in sample #A.

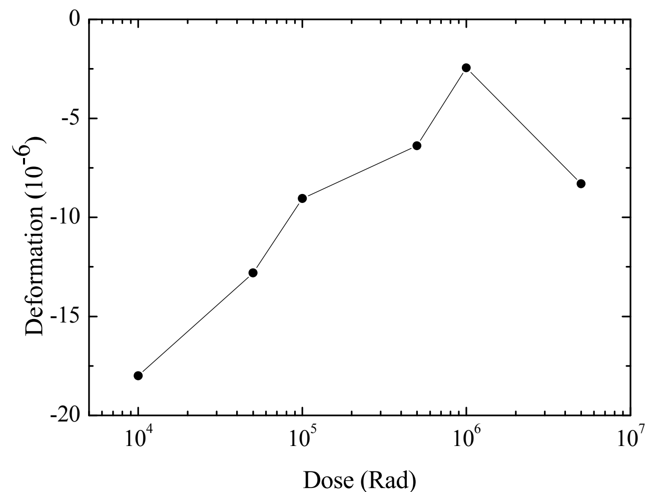

Figure 4.16. Dose dependence of elastic strains of the AlGaN layer

Study Self-heating Effect in High-Power GaN-based HEMTs

Since high electric field and high current density can be achieved in GaN-based devices the thermal properties of the structure and the wafer design have a strong influence on the overall device performance.

The channel resistance obtained from the measured I-V characteristics at room temperature is presented in table 4.2. As can be seen, the channels of AlGaN/GaN TLM structures with different layer composition have different resistance. Particularly, the

$Al_{0.33}Ga_{0.67}N$/GaN structures grown on sapphire substrate demonstrate high channel resistance. Two times lower resistance is observed on structures with wide bandgap $Al_{0.75}Ga_{0.25}N$ barrier layer. The use of AlN spacer results in an increase of channel resistance. Despite the expected improved transport properties of the structures grown on SiC substrate, the channel resistance obtained is slightly higher then that for the samples on sapphire substrate. It should be noted that the structures with thick GaN buffer show better performance then those with thin buffer. A slight decrease in channel conductance is observed for a thicker substrate.

Table 4.2.

Sample	**Channel resistance (Ohm/μm)**
#B	4.10
#D (0.3mm)	3.89
#D (3mm)	3.95
#A (Al_2O_3)	4.10
#A (SiC)	4.28
#C	4.95

The values in brackets in table 4.2 indicate sapphire substrate sickness and type of substrate for samples #D and #A respectively (also see Fig. 2.3).

The deviation from the ohmic law is observed in the I-V characteristics at dc bias higher then 1V (Fig.4.17). It is seen that the samples #A (SiC), #D show almost identical performance. The samples #A and #C show the worst performance. It can be clearly seen from the dependence of the relative change of the resistance on dissipated power at temperatures close to 300K (Fig.4.18), that the highest current in the sublinear regime is demonstrated by a high barrier sample #B. The use of SiC substrate or thick buffer layer results in higher current of saturation region of TLM I-Vs. On the other hand the use of an AlN spacer has a minor influence on the current value in the sublinear region. The measurements at temperatures from 70 K to 300K demonstrate similar results.

The comparison of the curves in Fig. 4.18 (with assumption that a similar dissipated power corresponds similar overheating temperature) allows one to conclude that increase of channel resistance under current flow has a complex origin. Not only a mobility decrease contributes to the decrease of conductance during overheating but also an additional mechanism, most likely a charge redistribution along the channel.

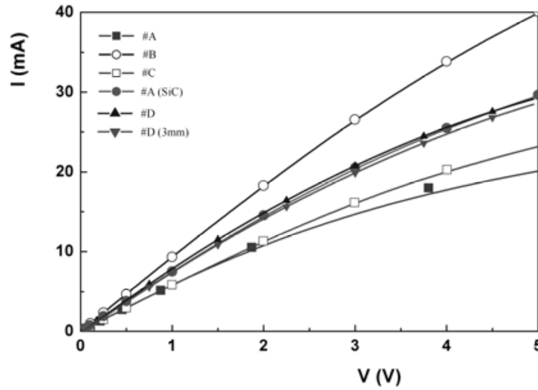

Figure 4.17. Comparison of TLM I-Vs. Channel length is 25 μm, width – 100 μm.

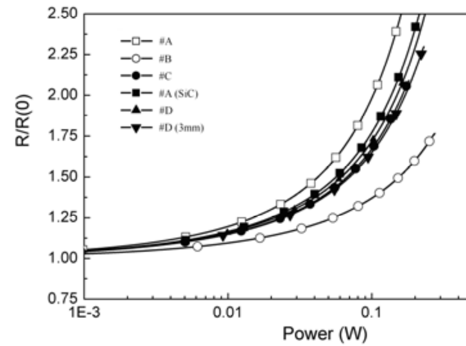

Figure 4.18. Relative change of resistance for different TLM-structures as a function of dissipated power.

The degree of charge redistribution along the channel can be reduced with the decrease of recharging intensity of traps in a barrier region.

The dynamics of traps recharging can be observed by measurements of non-equilibrium noise spectra. A significant difference in the noise spectra for samples with different barrier height was revealed (see Fig.4.19). It can be seen, that all devices demonstrate $1/f$ dependence in the high frequency part of the spectrum, but at lower frequencies additional noise appears. However, in low Al content devices the transition from low noise to high noise region is proportional to $1/f^2$ (corresponding to unity slope in normalized spectra in Fig.4.19), while in high Al content devices it exhibits $1/f^{3/2}$ behaviour ($f^{-1/2}$ slope in Fig.4.19).

The level of noise in samples with high Al content was found to be much lower than for low barrier samples. Additionally a decrease of the non-equilibrium noise was also registered for $Al_{0.33}Ga_{0.67}N/GaN$ samples with thin AlN spacer layer.

In order to understand the self-heating, and layer composition influence on the effect the theoretical model was build. The results of calculation of overheating temperature in the active channel of HEMT show that its value not only strongly depended on substrate type and thickness but also on thickness of buffer layer (fig. 4.20 (a), (b)).

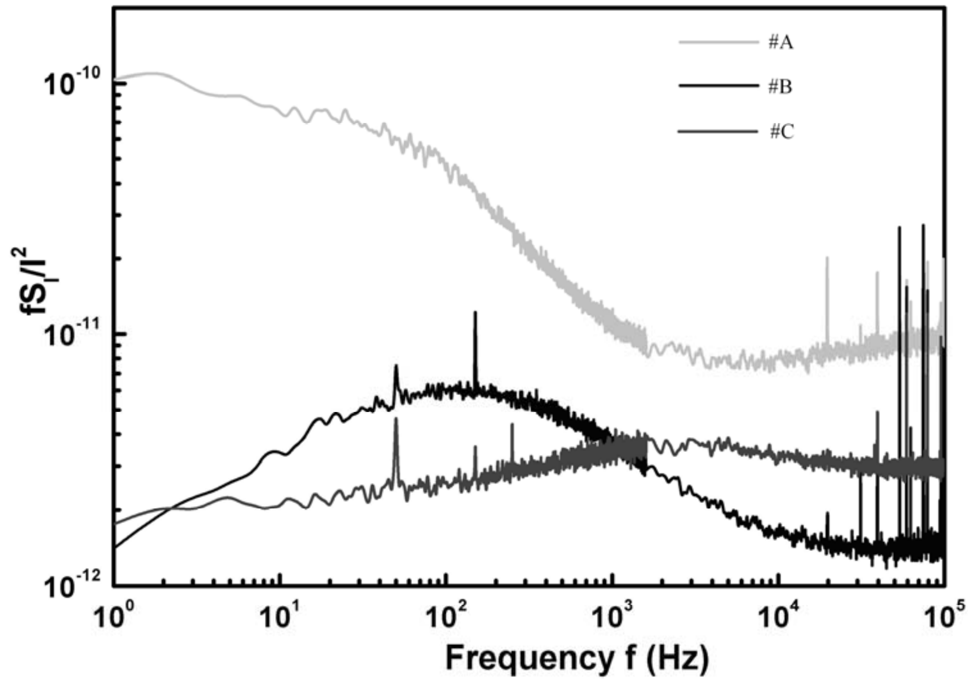

Figure 4.19. The low frequency noise of low and high Al content devices, measured for TLM structures at bias U = 10V and T = 300K.

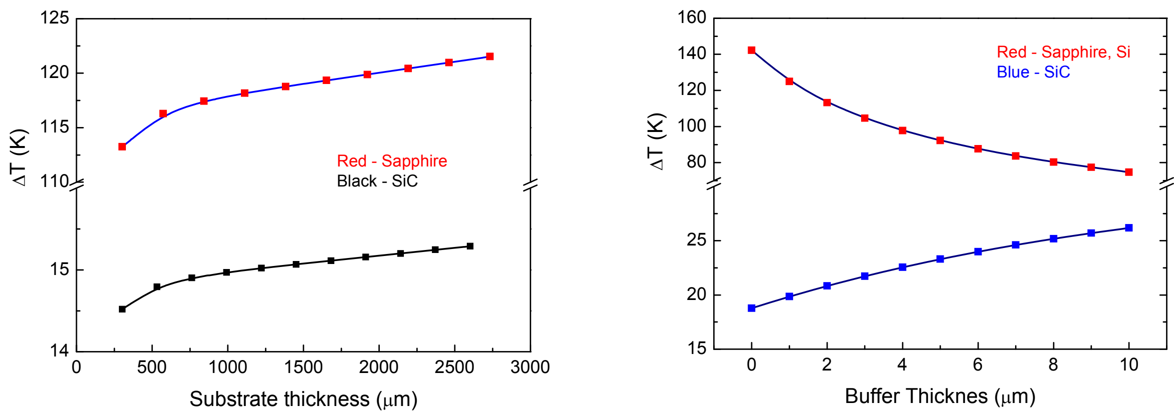

a b

Figure 4.20. a – dependence of temperature rise in the HEMT channel during operation on substrate sickness for sapphire and silicon carbide; b – dependence of the temperature rise on buffer layer thickness.

Summary

Noise spectra measurements allow to investigate the fundamental properties of advanced materials and heterostructures for the design of an ultra low-noise oscillators and sensors.

The analysis of noise spectra reviled fluctuation phenomena in GaN-based HEMT depend on several factors: layer structure design, processing technology, operating voltages, heating effects and quantum phenomena, variation of designed structure parameters with temperature, radiation surrounding.

Two characteristic gate voltage ranges were established, separated by different ratios of resistances and noise sources of the passive and active regions along the channel of the HEMT. An important contribution of the active region to the low-frequency part of noise spectra with increasing gate voltage was observed in the linear regime. Observed peculiarities in 1/f noise spectra were explained within the framework of a model based on the dynamic redistribution of lateral potential along the conducting channel.

The noise figure and corresponding value of voltage noise fluctuations of AlGaN/GaN transistor heterostructures are analysed in the important frequency range from 10 MHz to 100 MHz for different applied biases. It was established, that the observed noise can not be thermal noise, because this would yield an extremely high overheating temperature, about 2200 K. Also hot carrier noise cannot explain the observed results, while in this case the phonon lifetime should be very long, i.e. about 50 ns. At the same time, the results are very well described in the generation-recombination noise approach. Moreover, two independent components of the noise with different temperature behaviour were observed and investigated. It was determined that the maximum, observed in the temperature dependence of noise is caused by GR fluctuations at points of coincidence of quantum level with Fermi energy. Therefore the noise, measured at $f = 90\,\mathrm{MHz}$, originates from fluctuations of concentration at the first excited quantum level of 2DEG. Another GR component was observed at lower frequencies with time constant $\tau = 3.2\,\mathrm{ns}$. It demonstrates a different temperature dependence. The mechanism of the noise can be explained by increasing of penetration of electron wavefunctions into the barrier region with increase of self-heating.

A strong dependence of the thermal budget on the device structure was revealed and analyzed. It was shown that the use of wider bandgap barrier layers in heterostructures results in a significant improvement of device performance in comparison with narrow bandgap barriers. The insertion of a thin AlN spacer layer does not significantly affect the resistance of the device but leads to a decrease of low-frequency noise for the devices. The use of highly thermally conducive substrate or thick buffer layer results in an increase of current through devices due to enhanced thermal conductance of the structure. An increase of substrate thickness, however, has a minor influence on the 2DEG transport properties. It was shown that implementation of wider bandgap barrier layer in heterostructure, as well as wide bandgap spacer resulting in improvement of 2DEG dc performance and decrease of the noise level in TLM device structures.

The influence of gamma ray irradiation on the properties of AlGaN/GaN based HEMT structures has been investigated. It was found that even after high doses of gamma-irradiation up to 10^9 rad the devices remain operational. The possibility of radiation stimulated improvement of operational parameters of HEMT and mobility of 2DEG at low doses of gamma radiation (10^6 rad) is established.

Chapter 5. Transport of AlGaN/GaN-based RTD structures

In its simplest implementation, the resonant tunneling diode structure consists of two potential barriers sandwiching a well region. The structure is formed using two different semiconductor materials, typically a GaN well sandwiched by AlGaN (AlN) layers. The conduction band discontinuity between the GaN and AlGaN layers produces the potential barrier. Under equilibrium conditions, with no externally applied potential, the device, neglecting impurities and defects, is in flat band condition, as shown in Fig. 5.1 (a). There are three different regions of the device: the emitter, quantum well, and collector, as shown in the diagram. Notice that the emitter and collector regions are assumed to be degenerately doped. Consequently, the Fermi levels lie above the conduction band edge within these two regions, as shown in the diagram. The device is designed such that the first quantum level lies above the Fermi levels in the emitter and collector at equilibrium. Upon the application of a bias, the energy bands bend within the barriers and well, as shown in Fig. 5.1 (b). Since the emitter and collector are degenerately doped, it is assumed that all of the applied bias appears across the barriers and well. If the bias is sufficiently high, the quantum level becomes aligned with the Fermi level within the emitter. As a result, electrons within the emitter can now tunnel through the first barrier into the quantum level and then into the collector.

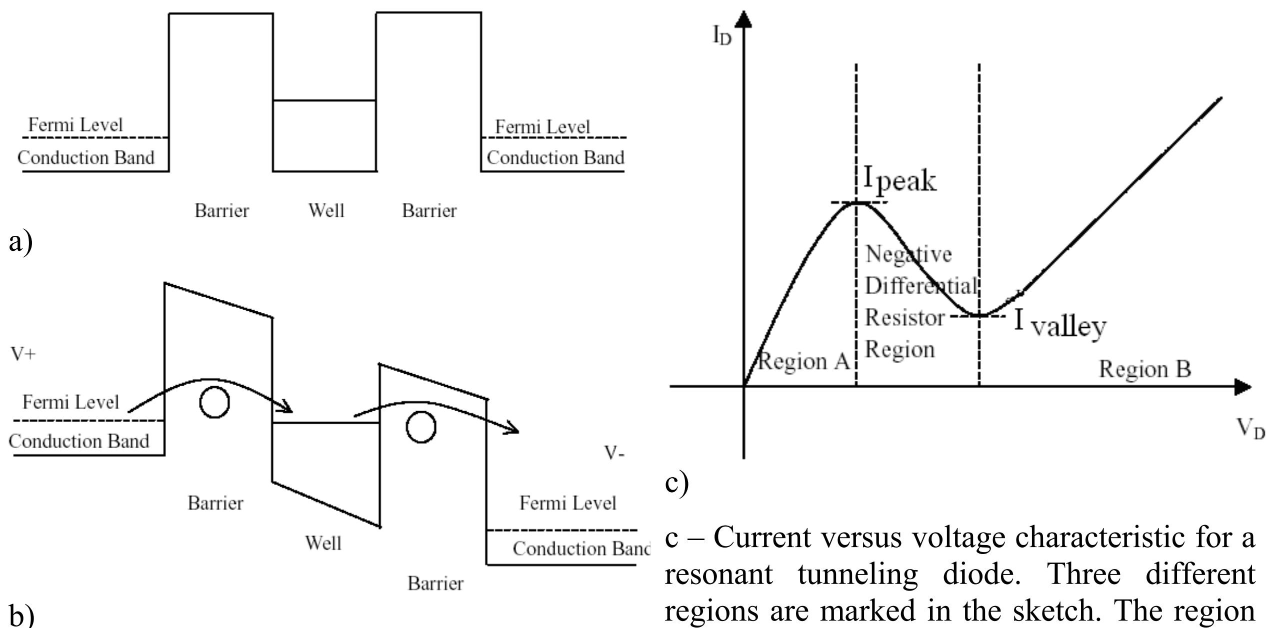

Figure 5.1 a- Two-barrier, single-quantum-well resonant tunneling diode under equilibrium conditions, b - double-barrier resonant tunneling diode under bias. Notice that the bias is such that the quantum level is aligned with the Fermi level in the emitter

c – Current versus voltage characteristic for a resonant tunneling diode. Three different regions are marked in the sketch. The region A corresponds to the case of low applied voltage, where the quantum level lies above the Fermi level within the emitter. The second region corresponds to alignment of the quantum level and the emitter Fermi level. The region B corresponds to thermionic emission.

The physics of the resonant tunneling process can be understood as follows. Tunneling occurs when the energy of an incident electron within the emitter matches that of an unoccupied state in the quantum well corresponding to the same lateral momentum. The current as a function of the applied voltage is shown in Figure 5.1 (c). The system starts in equilibrium, and of course, the current is zero. As the bias is applied, the quantum well is lowered in energy until the quantum level becomes aligned with the Fermi level within the emitter. Until the quantum level aligns with the Fermi level, the current is relatively low. Once the quantum level becomes aligned with the emitter Fermi level, a high current is flowing since tunneling now occur. As the voltage increases, the quantum level is continuously brought into alignment with electronic states (lying below the Fermi level) in the emitter and the current is increasing. As the voltage is increased further, the quantum level drops below the conduction band edge in the emitter. At these conditions there are no allowed energy states in the emitter. As a result, electrons cannot tunnel from the emitter into the quantum level and the current drops to a minimum value. The high current in region B is due to thermionic emission current flowing over the potential barriers since the bias is now sufficiently high that the potential barrier is pulled down close to the Fermi level. The two-barrier structure with quantum well in between is often compared to a Fabry–Perot resonator. Two barriers act like the partially transparent mirrors through which a electromagnetic wave coupled into and out of in a Fabry–Perot resonator. The transmissivity for electrons through the double-barrier shows resonant peaks when the perpendicular kinetic energy of the incident electron is equal to the quantum confined state energy. At these energies, the transmissivity of a double-barrier structure approaches 100% even though the transmissivity of a single barrier can be as low as 1%. The large enhancement in the transmissivity of the double-barrier structure arises physically from the fact that the amplitude of the resonant modes increases within the well due to multiple reflections of the electron wave by the potential barriers. As such, the device shows a dramatic increase in current upon resonant alignment. It is precisely for this reason that the process is referred to as resonant tunneling.

The most important parameters are peak current (I_{peak}), peak to valley ratio:

$$PVCR = I_{peak}/I_{valley} \tag{5.1.1}$$

First of all, the evolution of the potential profile was analysed at different applied voltages including resonant conditions (two of the profiles for more important cases: 0 V voltage bias and resonant condition bias are shown in Fig.5.2. The profiles were calculated for both polarities by self-consistently solving Schrödinger and Poisson equations taking into account

polarization effects in the structure. The calculated I-V characteristics were obtained from the profiles (shown in Fig. 5.3). Two resonant peaks were observed for both polarities. The first one is very small due to the location of the quantum-size level slightly below the conduction band on the right side of the active part device bowed by strong polarization fields. It should be noted that three orders of magnitude higher current density is expected for the peak current at reverse polarity in comparison to forward polarity.

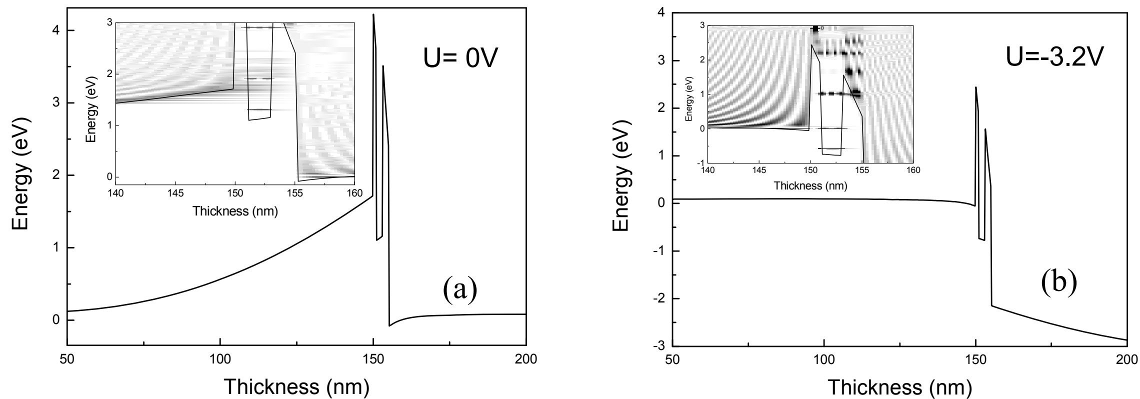

Figure 5.2 Self-consistently calculated conduction band profile and electron density of -states for the investigated AlN/GaN RTD a) at 0 V bias, b) at resonance peak position at reverse bias.

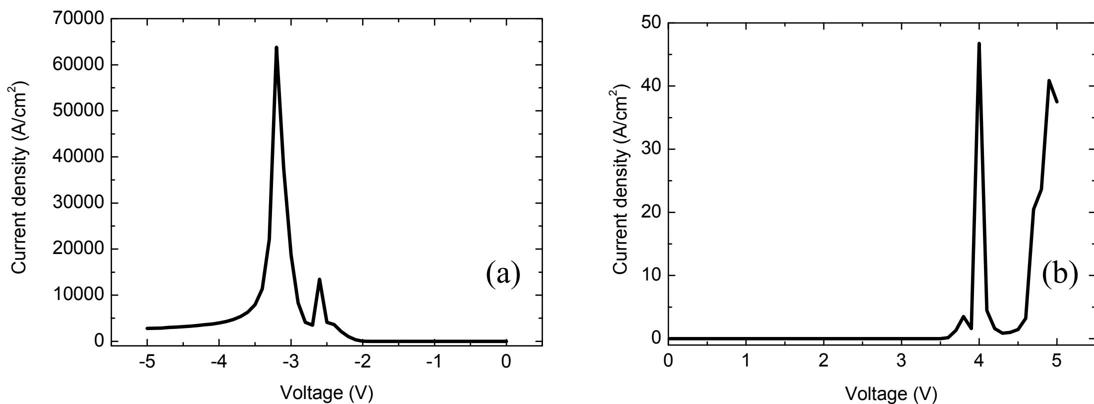

Figure 5.3 Calculated I-V characteristics for the investigated AlN/GaN RTD a) reverse bias, b) forward bias.

Fig. 5.4 shows the room temperature current-voltage characteristics of the RTD with 100 μm mesa diameter measured at forward and reverse biases. The forward bias corresponds to the tunnelling direction of the injected electrons from the substrate side. The high degree of current symmetry in the I-V characteristic is observed for the first measurement run with negative differential resistance region. The NDR disappeared after several runs just as observed previously and reported in [94]. This can be explained by current instabilities due to traps. The

density of the current is about 14 A/cm^2 at -3.4 V, where a peak at reverse polarity is predicted. The value is very small in comparison to the predicted 65 kA/cm^2, which is an additional confirmation of scattering processes in the structure.

Despite unstable behaviour observed in I-V, the C-V characteristics show very stable operation (Fig. 5.5). The C-V characteristics of a double-barrier RTD shows different behaviour under forward and reverse polarities and a strong dependence on frequency (some of the characteristics are shown in Fig. 5.5a). There is a growth of capacitance with forward bias, while a more complicated dependence appears at reverse voltages. At a frequency of 100 kHz a well-resolved maximum at about –2.7V is observed (Fig. 5.5b). It becomes more pronounced upon increasing the measurement frequency. The maximum position can be estimated from calculated profiles of the structure taking into account polarization effects at the AlN/GaN interfaces. The simulation reveals the formation of a 100 nm long depletion region at one side of the structure. The estimated zero-voltage capacitance caused by this region is in good agreement with experimental values at high frequencies. At frequencies lower than 100 kHz, the measured capacitance increases with decreasing frequency. This behaviour can be qualitatively explained by the influence of additional charges accumulated by traps located in the near-barrier region.

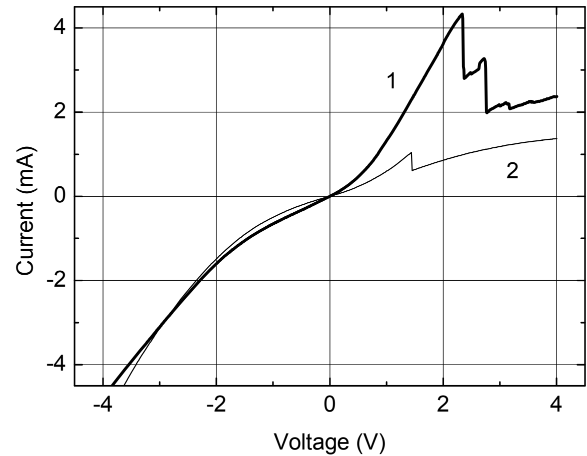

Figure 5.4 Current-voltage characteristics of RTD structures under test: 1 – initial, 2 – after several measurement runs.

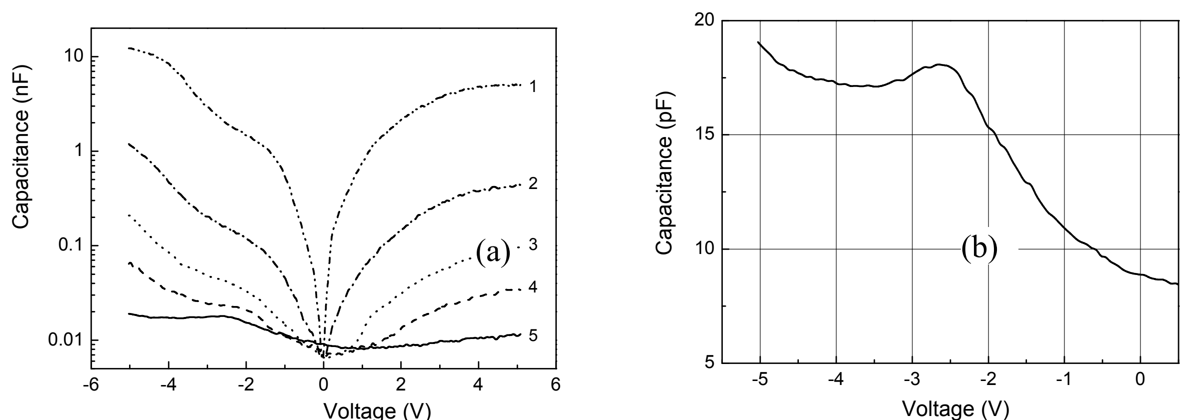

Figure 5.5 Capacitance-voltage characteristics, measured for a set of test signal frequencies: a) 1 – 1 kHz, 2 – 10 kHz, 3 – 50 kHz, 4 – 150 kHz, 5 – 1 MHz, b) enlarged characteristics measured at 1 MHz.

An additional confirmation of the influence of traps on the total capacitance of the structure is the small increase of capacitance observed in forward bias. The calculated conduction band profile for different forward and reverse voltages allows us to estimate the influence of the trapped charges on the capacitance behaviour. Capacitance values measured at reverse voltages are determined by charge trapping effects, depletion layer and the capacitance of the active double-barrier structure. In fact, with increasing frequency from 1 kHz to 100 kHz the decrease of capacitance can be explained by conduction band profile transformation and trap discharging. At the same time, at higher frequencies the transport phenomena are not influenced by most of the traps, and a maximum appears in the CV characteristics. The measured peak voltage is in good agreement with the calculated resonant tunnelling peak of the RTD. The results can be used for designing AlGaN/GaN RTDs with optimized layout and a more efficient analysis of resonant tunnelling processes and for improving the peak-to-valley ratio of NDR regions.

Conclusions

Structures made of Gallium Nitride and its alloys are promising for a wide range of different applications. These include: high-temperature, high-power and ultra-high-speed electronic devices, high frequency microwave oscillators, THz coherent sources, short-wavelength lasers, UV-optoelectronics, as well as specific devices - biological sensors and chemical sensors working in harsh environments. Semiconductor nanostructures based on the Group III-Nitrides hold out the prospect of greatly increased functionality and performance enhancement of microelectronic and optoelectronic devices compared with devices based on more established semiconductors like Gallium Arsenide and Silicon. The unique electron transport properties of the nitrides, particularly the large peak and saturated drift velocities and high breakdown fields, are promising to the development of high-power and very high-frequency transistors.

The factors influencing the effective mass enhancement in the 2DEG formed at the AlGaN/GaN heterojunction were analyzed. It is shown that the conduction band non-parabolicity effect is overestimated and that the wave function penetration into the barrier layer should be taken into account. The contribution of the wave function hybridization is determined to play the dominant role. The band edge effective mass value is deduced to be 0.185 ±0.01 m_0.

The effect of spin-orbit interaction is studied in 2DEG system at AlGaN/GaN interface. The effect of weak antilocalization is observed on low-temperature conductivity of 2DEG in asymmetrical AlGaN/GaN quantum well in low-magnetic field. The value of Rashba constant, as strength of spin-orbit interaction, found to be 1.01×10^{-12} eVm in AlGaN/GaN 2DEG.

The improvement of transport properties of the 2DEG in AlGaN/GaN heterostructures after the treatment with the small doses of gamma-irradiation is described. The samples displayed a considerable increase of mobility at T = 0.3 K. This work suggests that further improvements in transport characteristics can be achieved by using gamma-quanta irradiation in processing technology.

It is found that the noise behaviour of GaN-based devices depends on several factors: layer structure design, processing technology, operating voltages, heating effects and quantum phenomena, variation of designed structure parameters with temperature and radiation surrounding. Two characteristic gate voltage ranges were established, separated by different ratios of resistances and noise sources of the passive and active regions along the channel of the HEMT. An important contribution of the active region to the low-frequency part of noise spectra with increasing gate voltage was observed in the linear regime. Observed peculiarities in 1/f noise spectra were explained within the framework of a model based on the dynamic redistribution of lateral potential along the conducting channel. It was shown that implementation of wider bandgap barrier layer in heterostructure, as well as wide band gap spacer resulting in improvement of 2DEG dc performance and decrease of the noise level in TLM device structures.

The noise figure and corresponding value of voltage noise fluctuations of AlGaN/GaN transistor heterostructures are analysed in the important frequency range from 10 MHz to 100 MHz for different applied biases. It was established, that the observed noise can not be thermal noise. The results are very well described in the generation-recombination noise approach. Moreover, two independent components of the noise with different temperature behaviour were observed and investigated. It was determined that the maximum, observed in the temperature dependence of noise is caused by GR fluctuations at points of coincidence of quantum level with Fermi energy. The noise, measured at $f = 90\ \text{MHz}$, originates from fluctuations of concentration at the first excited quantum level of 2DEG. Another GR component was observed at lower frequencies with time constant $\tau = 3.2\ \text{ns}$. It demonstrates a different temperature dependence. The mechanism of the noise can be explained by increasing of penetration of electron wavefunctions into the barrier region with increase of self-heating.

A strong dependence of the thermal budget on the device structure was revealed and analyzed. It was shown that the use of wider bandgap barrier layers in heterostructures results in a significant improvement of device performance in comparison with narrow bandgap barriers. The insertion of a thin AlN spacer layer does not significantly affect the resistance of the device but leads to a decrease of low-frequency noise for the devices. The use of highly thermally conducive substrate or thick buffer layer results in an increase of current through devices due to enhanced thermal conductance of the structure. An increase of substrate thickness, however, has

a minor influence on the 2DEG transport properties, but increase of GaN buffer layer thickness for devices made on sapphire can significantly improve their performance.

In contrast to the I-V characterization of double barrier heterostructures, our capacitance measurements demonstrate reproducible characteristics in all frequency ranges. The observed peculiarities in capacitance-voltage characteristics reveal a strong correlation with estimated resonance parameters for the investigated double-barrier structures. The analysis of frequency-dependent changes of capacitance-voltage profiles provides additional information on peculiarities in the transport properties of RTD devices related to an interface state. Thus, the capacitance measurements of double-barrier RTDs are a powerful and sensitive tool for the exploration of transport features and structural quality. The results can be used for designing AlGaN/GaN RTDs with optimized layout, a more efficient analysis of resonant tunnelling processes and for improving the peak-to-valley ratio of NDR regions.

The obtained results should be taken into account during development of new devices based on AlGaN/GaN heterostructures for high-speed and high-power electronics, and during conduction of new researches on transport properties and radiation hardness of GaN-based device structures.

References

[1] Z. Bougrioua, I. Moerman, L. Nistor, B. Van Daele, E. Monroy, T. Palacios, F. Calle, and M. Leroux: *Engineering of an insulating buffer and use of AlN interlayers: two optimisations for AlGaN−GaN HEMT-like structures*, Physica Status Solidi (a) 195 (1), p. 93, 2003

[2] H. Morkoc: *Nitride Semiconductors and Devices*, Springer, 1999

[3] S.N. Mohammad, H. Morkoc: *Progress and prospects of group-III nitride semiconductors*, Progress in Quantum Electronics 20 (5/6) p. 361, 1996

[4] http://www.scirus.com/

[5] S.J. Pearton, J.C. Zolper, R.J. Shul, F. Ren: *GaN: Processing, defects, and devices*, Journal of Applied Physics 86 (1), p.1, 1999

[6] S.J. Pearton, F. Ren, A.P. Zhang, K.P. Lee: *Fabrication and performance of GaN electronic devices*, Materials Science and Engineering, R30, p.55, 2000

[7] O Ambacher, J Majewski, C Miskys, A Link, M Hermann, M Eickhoff, M Stutzmann, F Bernardini, V Fiorentini, V Tilak, B Schaff and L F Eastman: *Pyroelectric properties of Al(In)GaN/GaN hetero- and quantum well structures,* Journal of Physics: Condensed Matter 14, p.3399, 2002

[8] O. Ambacher, B. Foutz, J. Smart, J. R. Shealy, N. G. Weimann, K. Chu, M. Murphy, A. J. Sierakowski, W. J. Schaff, L. F. Eastman, R. Dimitrov, A. Mitchell, and M. Stutzmann: *Two dimensional electron gases induced by spontaneous and piezoelectric polarization in undoped and doped AlGaN/GaN heterostructures*, Journal of Applied Physics 87 (1), p. 334, 2000

[9] M. S. Shur, R. Gaska, A. Bykhovski: *GaN-based electronic devices*, Solid-State Electronics 43 (8), p.1451, 1999

[10] J. P. Ibbetson, P. T. Fini, K. D. Ness, S. P. DenBaars, J. S. Speck, and U. K. Mishra: *Polarization effects, surface states, and the source of electrons in AlGaN/GaN heterostructure field effect transistors*, Applied Physics Letters 77, p.250

[11] L. Hsu and W. Walukiewicz: *Theoretical transport studies of p-type GaN/AlGaN modulation-doped heterostructures*, Applied Physics Letters **74**, p. 2405, 1999

[12] M. S. Shur, A. D. Bykhovski, and R. Gaska: *Two-dimensional hole gas induced by piezoelectric and pyroelectric charges*, Solid-State Electron. **44 (2)**, p. 205, 2000

[13] S. Hackenbuchner, J. A. Majewski, G. Zandler, and P. Vogl: *Polarization induced 2D hole gas in GaN/AlGaN heterostructures*, Journal of Crystal Growth **230**, p. 607, 2001

[14] A. Link, O. Ambacher, I. P. Smorchkova, U. K. Mishra, J. S. Speck, and M. Stutzmann: *Formation and electronic transport of 2D electron and hole gases in AlGaN/GaN heterostructures,* Materials Science Forum **353-356**, p. 787, 2000

[15] P. Kozodoy, M. Hansen, S. P. DenBaars, and U. K. Mishra: *Enhanced Mg doping efficiency in $Al_{0.2}Ga_{0.8}N$/GaN superlattices*, Applied Physics Letters **74**, p. 3681, 1999

[16] K. Kumakura and N. Kobayashi: *Increased Electrical Activity of Mg-Acceptors in* $Al_xGa_{1-x}N$*/GaN Superlattices*, Japanese Journal of Applied Physics, **38**, L1012, 1999

[17] D. Pavlidis: *GaN THz Electronics*, 12th Gallium Arsenide Application Symposium, Amsterdam, p.551, 2004

[18] X. Liu, L. Wang, D.-C. Lu, D. Wang, X. Wang, L. Lin: *The influence of thickness on properties of GaN buffer layer and heavily Si-doped GaN grown by metalorganic vapor-phase epitaxy*, Journal of Crystal Growth 189-190, p. 287, 1998

[19] A.M. Wells, M.J. Uren, R.S. Balmer, K.P. Hilton, T. Martin, M. Missous: *Direct demonstration of the 'virtual gate' mechanism for current collapse in AlGaN/GaN HFETs*, Solid-State Electronics 49 (2), p.279, 2005

[20] P Kordos, J Bernát, D Gregusová, M Marso, H Lüth: *Impact of surface treatment under the gate on the current collapse of unpassivated AlGaN/GaN heterostructure field-effect transistors*, Semiconductor Science and Technology 21 (1), p. 71, 2006

[21] G. Simin, A. Koudymov, A. Tarakji, X. Hu, J. Yang, M. Asif Khan, M. S. Shur and R. Gaska: Induced strain mechanism of current collapse in AlGaN/GaN heterostructure field-effect transistors, Applied Physics Letters 79 (16), p. 2651, 2001

[22] N. Sghaier, M. Trabelsi, N. Yacoubi, J.M. Bluet, A. Souifi, G. Guillot, C. Gaquière, J.C. DeJaeger: *Traps centers and deep defects contribution in current instabilities for AlGaN/GaN HEMT's on silicon and sapphire substrates*, Microelectronics Journal 37 (4), p. 363, 2006

[23] S. A. Vitusevich, S. V. Danylyuk, and N. Klein, M. V. Petrychuk, A. Yu. Avksentyev, V. N. Sokolov, V. A. Kochelap, A. E. Belyaev, V. Tilak, J. Smart, A. Vertiatchikh, L. F. Eastman: *Separation of hot-electron and self-heating effects in two-dimensional AlGaN/GaN-based conducting channels*, Applied Physics Letters 82 (5), p. 748, 2003

[24] J. Kim, J.A. Freitas, Jr., J. Mittereder, R. Fitch, B.S. Kang, S.J. Pearton and F. Ren: *Effective temperature measurements of AlGaN/GaN-based HEMT under various load lines using micro-Raman technique*, Solid-State Electronics 50 (3), p. 408, 2006

[25] J. Würfl, V. Abrosimova, J. Hilsenbeck, E. Nebauer, W. Rieger and G. Tränkle: Reliability considerations of III-nitride microelectronic devices, Microelectronics Reliability 39 (12), p. 1737, 1999

[26] P. Horowitz, W. Hill: *The Art of Electronics,* Cambridge University Press, Cambridge, 1989

[27] B. S. Kang, J. Kim, S. Jang, and F. Ren, J. W. Johnson, R. J. Therrien, P. Rajagopal, J. C. Roberts, E. L. Piner, and K. J. Linthicum, S. N. G. Chu, K. Baik, B. P. Gila, C. R. Abernathy, and S. J. Pearton: *Capacitance pressure sensor based on GaN high-electron-mobility transistor-on-Si membrane*, Applied Physics Letters 86, 253502, 2005

[28] A. J. Ekpunobi, A. O. E. Animalu: *Band offsets and properties of AlGaAs/GaAs and AlGaN/GaN material systems*, Superlattices and Microstructures 31 (5), p. 247, 2002

[29] H. Ünlü and A. Asenov: *Band offsets in III-nitride heterostructures*, Journal of Physics D: Applied Physics 35, p. 591, 2002

[30] F. Yun, M. A. Reshchikov, L. He, T. King, H. Morkoc, S.W. Novak, L. Wei: *Energy band bowing parameter in $Al_xGa_{1-x}N$ alloys*, Journal of Applied Physics 92 (8), p.4837, 2002

[31] S. Satpathy, Z. S. Popovic, W. C. Mitchel: *Theory of the composition dependence of the band offset and sheet carrier density in the GaN/$Al_xGa_{1-x}N$ heterostructure*, Journal of Applied Physics 95 (10), p.5597, 2004

[32] I. Vurgaftman and J. R. Meyer, L. R. Ram-Mohan: *Band parameters for III–V compound semiconductors and their alloys*, Journal of Applied Physics 89 (11), p.5815, 2001

[33] D. R. Hang, C. H. Chen, and Y. F. Chen, H. X. Jiang and J. Y. Lin: *$Al_xGa_{1-x}N$/GaN band offsets determined by deep-level emission*, Journal of Applied Physics 90 (4), p.1887, 2001

[34] A. N. Westmeyer, S. Mahajan, and K. K. Bajaj, J. Y. Lin and H. X. Jiang, D. D. Koleske, R. T. Senger: *Determination of energy-band offsets between GaN and AlN using excitonic luminescence transition in AlGaN alloys,* Journal of Applied Physics 99, 013705, 2006

[35] I. Vurgaftman and J. R. Meyer: *Band parameters for nitrogen-containing semiconductors*, Journal of Applied Physics 94 (6), p. 3675, 2003

[36] J.-P. Zhang, D.-Z. Sun, X.-L. Wang, M.-Y. Kong, Y.-P. Zeng, J.-M. Li, L.-Y. Lin: *Fermi-edge singularity observed in a modulation-doped AlGaN/GaN heterostructure*, Applied Physics Letters 73 (17), p.2471, 1998

[37] W. Knap, E. Frayssinet, and M. L. Sadowski, C. Skierbiszewski, D. Maude, V. Falko, M. Asif Khan, M. S. Shur: *Effective g* factor of two-dimensional electrons in GaN/AlGaN heterojunctions*, Applied Physics Letters 75 (20), p.3156, 1999

[38] E. Frayssinet W. Knap, P. Lorenzini, N. Grandjean, and J. Massies, C. Skierbiszewski, T. Suski, I. Grzegory, and S. Porowski, Simin, X. Hu, and M. Asif Khan, S. Shur and R. Gaska: *High electron mobility in AlGaN/GaN heterostructures grown on bulk GaN substrates*, Applied Physics Letters 77 (16), p.2551, 2000

[39] D. R. Hang, C.-T. Liang, C. F. Huang, Y. H. Chang, and Y. F. Chen, H. X. Jiang and J. Y. Lin *Effective mass of two-dimensional electron gas in an $Al_{0.2}Ga_{0.8}N$/GaN heterojunction*, Applied Physics Letters 79 (1), p.66, 2001

[40] Z.-F. Li, W. Lu, and S. C. Shen, S. Holland, C. M. Hu, and D. Heitmann, B. Shen and Y. D. Zheng, T. Someya and Y. Arakawa: *Cyclotron resonance and magnetotransport measurements in $Al_xGa_{1-x}N$/GaN heterostructures for x 0.15– 0.30*, Applied Physics Letters 80 (3), p. 431, 2002

[41] N. Thillosen, Th. Schapers, N. Kaluza, H. Hardtdegen, and V. A. Guzenko: *Weak antilocalization in a polarization-doped $Al_xGa_{1-x}N$/GaN heterostructure with single subband occupation*, Applied Physics Letters 88, 022111, 2006

[42] N. Tang, B. Shen,a_ M. J. Wang, K. Han, Z. J. Yang, K. Xu, and G. Y. Zhang, T. Lin, B. Zhu, W. Z. Zhou, and J. H. Chu: *Beating patterns in the oscillatory magnetoresistance originated from zero-field spin splitting in $Al_xGa_{1-x}N$/GaN heterostructures*, Applied Physics Letters 88, 172112, 2006

[43] S. Elhamri, W. C. Mitchel, W. D. Mitchell, and G. R. Landis, R. Berney, A. Saxler: *Study of the effects of an AlN interlayer on the transport properties of AlGaN/AlN/GaN heterostructures grown on SiC*, Applied Physics Letters 90, 042112, 2007

[44] T. Wang, J. Bai, and S. Sakai, Y. Ohno and H. Ohno: *Magnetotransport studies of AlGaN/GaN heterostructures grown on sapphire substrates: Effective mass and scattering time*, Applied Physics Letters 76 (19), p.2737, 2000

[45] S. Syed, J. B. Heroux, Y. J. Wang, M. J. Manfra, R. J. Molnar, H. L. Stormer: *Nonparabolicity of the conduction band of wurtzite GaN*, Applied Physics Letters 83 (22), p.4553, 2003

[46] N. Tang, B. Shen,a_ M. J. Wang, Z. J. Yang, K. Xu, and G. Y. Zhang, T. Lin, B. Zhu, W. Z. Zhou, and J. H. Chu: *Effective mass of the two-dimensional electron gas and band nonparabolicity in* $Al_xGa_{1-x}N/GaN$ *heterostructures*, Applied Physics Letters 88, 172115, 2006

[47] D. R. Hang, C. F. Huang, Y. F. Chen: *Two-subband-populated AlGaN/GaN heterostructures probed by electrically detected and microwave-modulated magnetotransport measurements*, Applied Physics Letters 89, 092116, 2006

[48] K. S. Cho, Tsai-Yu Huang, Hong-Syuan Wang, Ming-Gu Lin, Tse-Ming Chen, C.-T. Liang, and Y. F. Chen, Ikai Lo: *Zero-field spin splitting in modulation-doped* $Al_xGa_{1-x}N/GaN$ *two-dimensional electron systems*, Applied Physics Letters 86, 222102, 2005

[49] P. Lorenzini and Z. Bougrioua, A. Tiberj, R. Tauk, M. Azize, M. Sakowicz, K. Karpierz, and W. Knap: *Quantum and transport lifetimes of two-dimensional electrons gas in AlGaN/GaN heterostructures*, Applied Physics Letter 87, 232107, 2005

[50] J J Harris, K J Lee, T Wang, S Sakai, Z Bougrioua, I Moerman, E J Thrush, J B Webb, H Tang, T Martin, D K Maude and J-C Portal: *Relationship between classical and quantum lifetimes in AlGaN/GaN heterostructures*, Semiconductor Science and Technology 16, p. 402, 2001

[51] M. J. Manfra, S. H. Simon, K. W. Baldwin, A. M. Sergent, and K. W. West, R. J. Molnar and J. Caissie: *Quantum and transport lifetimes in a tunable low-density AlGaN/GaN two-dimensional electron gas*, Applied Physics Letters 85 (22), p. 5278, 2004

[52] S. Contreras, W. Knap, and E. Frayssinet, M. L. Sadowski, M. Goiran, M. Shur: *High magnetic field studies of two-dimensional electron gas in a GaNOGaAlN heterostructure: Mechanisms of parallel conduction,* Journal of Applied Physics 89 (2), p.1251, 2001

[53] Z. W. Zheng and B. Shen, Y. S. Gui, Z. J. Qiu, and C. P. Jiang, N. Tang, J. Liu, D. J. Chen, H. M. Zhou, R. Zhang, Y. Shi, and Y. D. Zheng, S. L. Guo and J. H. Chu, K. Hoshino and Y. Arakawa: *Enhancement and anisotropy of the Landau g factor in modulation-doped* $Al_{0.22}Ga_{0.78}N/GaN$ *heterostructures*, Journal of Applied Physics 95 (5), p.2473, 2004

[54] K. S. Cho, Tsai-Yu Huang, Chao-Ping Huang, Yi-Hsing Chiu, C.-T. Liang, and Y. F. Chen, Ikai Lo: *Exchange-enhanced g-factors in an* $Al_{0.25}Ga_{0.75}N/GaN$ *two-dimensional electron system,* Journal of Applied Physics 96 (12), p.7370, 2004

[55] S. Das Sarma, F. Stern: *Single-particle relaxation time versus scattering time in impure electron gas*, Physical Review B 32 (12), p. 8442, 1985

[56] E. Frayssinet, W. Knap, P. Lorenzini, N. Grandjean, J. Massies, C. Skierbiszewski, T. Suski, I. Grzegory, S. Porowski, G. Simin, X. Hu, M. Asif Khan, M. S. Shur, R. Gaska, and D. Maude: *High electron mobility in AlGaN/GaN heterostructures grown on bulk GaN substrates,* Applied Physics Letters 77 (16), p. 2551, 2000

[57] L. K. Li, B. Turk, and W. I. Wang, S. Syed, D. Simonian, and H. L. Stormer: *High electron mobility AlGaN/GaN heterostructures grown on sapphire substrates by molecular-beam epitaxy,* Applied Physics Letters 76 (6), p.742, 2000

[58] M. J. Manfra, K. W. Baldwin, A. M. Sergent, and K. W. West, R. J. Molnar and J. Caissie: *Electron mobility exceeding 160 000 cm^2/Vs in AlGaN/GaN heterostructures grown by molecular-beam epitaxy*, Applied Physics Letters 85 (22), p.5394, 2004

[59] Syed, M. J. Manfra, Y. J. Wang, R. J. Molnar, and H. L. Stormer: *Electron scattering in AlGaN/GaN structures*, Applied Physics Letters 84 (9), p. 1507, 2004

[60] W. Knap, V.I. Fal'ko, E. Frayssinet, P. Lorenzini, N. Grandjean, D. Maude, G. Karczewski, B.L. Brandt, J. Łusakowski, I. Grzegory, M. Leszczynski, P. Prystawko, C. Skierbiszewski, S. Porowski, X. Hu, G. Simin, M. Asif Khan and M.S. Shur: *Spin and interaction effects in Shubnikov–de Haas oscillations and the quantum Hall effect in GaN/AlGaN heterostructures,* Journal of Physics: Condensed Matter 16, p. 3421, 2004

[61] Z.J. Qiu, Y.S. Gui, Z.W. Zheng, N. Tang, J. Lu, B. Shen, N. Dai, J.H. Chu: *Beating patterns in the oscillatory magnetoresistance of an AlGaN/GaN heterostructure*, Solid State Communications 129, p. 187, 2004

[62] N. Tang, B. Shen,a_ M. J. Wang, K. Han, Z. J. Yang, K. Xu, and G. Y. Zhang, T. Lin, B. Zhu, W. Z. Zhou, and J. H. Chu: *Beating patterns in the oscillatory magnetoresistance originated from zero-field spin splitting in AlxGa1−xN/GaN heterostructures*, Applied Physics Letters 88, 172112, 2006

[63] K. Tsubaki, N. Maeda, T. Saitoh, and N. Kobayashi: *Spin splitting in modulation-doped AlGaN/GaN two-dimensional electron gas*, Applied Physics Letters 80 (17), p.3126, 2002

[64] W. Weber, S. D. Ganichev,a_ S. N. Danilov, D. Weiss, and W. Prettl, Z. D. Kvon, V. V. Bel'kov and L. E. Golub, Hyun-Ick Cho and Jung-Hee Lee: *Demonstration of Rashba spin splitting in GaN-based heterostructures,* Applied Physics Letters 87, 262106 2005

[65] S. A. Vitusevich, A. M. Kurakin, S. V. Danylyuk, N. Klein, H. Lüth, and A. E. Belyaev: *Low-Temperature Transport in AlGaN/GaN 2D Electron Systems*, AIP Conference Proceedings 772, p. 459, 2005

[66] V. Renard, Z. D. Kvon, Hyun-Ick Cho, Jung-Hee Lee, and J. C. Portal: *Weak localization and interaction effects in 2D electron gas in AlGaN/GaN heterostructure in presence of phonons*, AIP Conference Proceedings 772, p. 445, 2005

[67] S. Schmult, M. J. Manfra, A. Punnoose, A. M. Sergent, K. W. Baldwin, and R. J. Molnar: *Large Bychkov-Rashba spin-orbit coupling in high mobility GaN/AlGaN heterostructures*, Physical Review B 74, 033302, 2006

[68] Yu. A. Bychkov, E.I. Rashba: *Properties of 2D electron gas with lifted spectral degeneracy*, JETP Letters 39 (2), p. 78, 1984

[69] S. A. Vitusevich, S. V. Danylyuk, A. M. Kurakin, N. Klein, and A. Offenhausser, M. V. Petrychuk, A. E. Belyaev: *Origin of noise in AlGaN/GaN heterostructures in the range of 10–100 MHz*, Journal of Applied Physics 99, 073706, 2006

[70] S. A. Vitusevich, S. V. Danylyuk, N. Klein, M. V. Petrychuk, V. N. Sokolov, V. A. Kochelap, A. E. Belyaev, V. Tilak, J. Smart, A. Vertiatchikh, and L. F. Eastman: *Excess low-frequency noise in AlGaN/GaN-based high-electron-mobility transistors*, Applied Physics Letters 80 (12), p. 2126, 2002

[71] S. A. Vitusevich, S. V. Danylyuk, and N. Klein, M. V. Petrychuk, A. E. Belyaev: *Power and temperature dependence of low frequency noise in AlGaN/GaN transmission line model structures*, Journal of Applied Physics 96 (10), p.5625, 2004

[72] S.A. Vitusevich, S.V. Danylyuk, M.V. Petrychuk, O.A. Antoniuk, N. Klein, A.E. Belyaev: *Equilibrium and non-equilibrium 1/f noise in AlGaN/GaN TLM structures,* Applied Surface Science 238, p. 143, 2004

[73] Rolando S. Duran and Grover L. Larkins, Jr., Carolyne M. Van Vliet, Hadis Morkoc: *Generation–recombination noise in gallium nitride-based quantum well structures*, Journal of Applied Physics 93 (9), p. 5337, 2003

[74] J. A. Garrido, B. E. Foutz, J. A. Smart, J. R. Shealy, M. J. Murphy, W. J. Schaff, and L. F. Eastman, E. Munoz: *Low-frequency noise and mobility fluctuations in AlGaNOGaN heterostructure field-effect transistors*, Applied Physics Letters 76 (23), p. 3442, 2000

[75] M. E. Levinshtein and S. L. Rumyantsev, D. C. Look, R. J. Molnar, M. Asif Khan, G. Simin, and V. Adivarahan, M. S. Shur: *Low-frequency noise in n-GaN with high electron mobility*, Journal of Applied Physics 86 (9), p. 5075, 1999

[76] S. L. Rumyantsev, Y. Deng, S. Shur, M. E. Levinshtein, M. Asif Khan, G. Simin, J. Yang, X. Hu, R. Gaska: *On the low frequency noise mechanisms in GaN/AlGaN HFETs*, Semiconductor Science and Technology 18, p. 589, 2003

[77] S. L. Rumyantsev, N. Pala, M. S. Shur, R. Gaska, M. E. Levinshtein, M. Asif Khan, G. Simin, X. Hu, J. Yang: *Low frequency noise in GaN metal semiconductor and metal oxide semiconductor field effect transistors*, Journal of Applied Physics 90 (1), p. 310, 2001

[78] M.N.Tutt, D.Pavlidis, A.Khatibzadeh and B. Bayraktaroglu: *Investigation of HBT oscillator noise through 1/f noise and noise upconversion studies,* IEEE MTT-S Int.Microwave Symp.Dig. p. 727, 1992

[79] H.Fukui: *Optimal Noise Figure of Microwave GaAs MESFET's*, IEEE Trans. Electron Devices **ED-26**, p.1032, 1979

[80] H.-F. Teng, S.-L. Jang and M.-H. Juang: *Modeling of Degradation Effects on the High Frequency Noise of Metal–Oxide–Semiconductor Field-Effect Transistors,* Japanese Journal Applied. Physics **44**, p.38, 2005

[81] L.Pantisano, and K.P.Cheung: *Origin of microwave noise from an n-channel metal–oxide–semiconductor field effect transistor*, Journal Applied Physics **92**, p.6679, 2002

[82] R. Vetury, N. Q. Zhang, S. Keller, U. K. Mishra: *The impact of surface states on the DC and RF characteristics of AlGaN/GaN HFETs*, IEEE Transactions on Electron Devices 48, p. 560, 2001

[83] S. Arulkumaran, T. Egawa, H. Ishikawa, T. Jimbo, Y. Sano: *Surface passivation effects on AlGaN/GaN high-electron-mobility transistors with SiO_2, Si_3N_4, and silicon oxynitride*, Applied Physics Letters 84 (4), p. 613, 2004

[84] M. Asif Khan, X. Hu, G. Sumin, A. Lunev, J. Yang, R. Gaska, and M. S. Shur: *AlGaN/GaN metal oxide semiconductor heterostructure field effect transistor*, IEEE Electron Device Letters 21 (2), p.63, 2000

[85] R. Mehandru, B. Luo, J. Kim, and F. Ren, B. P. Gila, A. H. Onstine, C. R. Abernathy, and S. J. Pearton, D. Gotthold, R. Birkhahn, and B. Peres, R. Fitch, J. Gillespie, T. Jenkins, J. Sewell, D. Via, and A. Crespo: *AlGaN/GaN metal–oxide–semiconductor high electron mobility transistors using Sc_2O_3 as the gate oxide and surface passivation*, Applied Physics Letters 82 (15), p. 2530, 2003

[86] J.R. Shealy, T.R. Prunty, E.M. Chumbes, B.K. Ridley: *Growth and passivation of AlGaN/GaN heterostructures,* Journal of Crystal Growth 250, p. 7, 2003

[87] D. J. Chen, Y. Q. Tao, C. Chen, R. Zhang, and Y. D. Zheng, M. J. Wang and B. Shen, Z. H. Li, G. Jiao, and T. S. Chen: *Improved transport properties of the two-dimensional electron gas in AlGaN/GaN heterostructures by AlN surface passivation layer*, Applied Physics Letters 89, 252104, 2006

[88] A. Asgari, M. Kalafi, L. Faraone: *The effects of GaN capping layer thickness on two-dimensional electron mobility in GaN/AlGaN/GaN heterostructures*, Physica E 25, p. 431, 2005

[89] J. Bernat, P. Javorka, A. Fox, M. Marso, H. Lüth, P. Kordos: *Effect of surface passivation on performance of AlGaN/GaN/Si HEMTs,* Solid-State Electronics 47, p. 2097, 2003

[90] B.M. Greene, K.K. Chu, E.M. Chumbes, J.A. Smart, J.R. Shealy and L.F. Eastman: *The effect of surface passivation on the microwave characteristics of undoped AlGaN/GaN HEMTs*, IEEE Electron Device Letters 21, p. 268, 2000

[91] C.M. Jeon, J.-L. Lee: Effects of tensile stress induced by silicon nitride passivation on electrical characteristics of AlGaN/GaN heterostructure field-effect transistors, Applied Physics Letters 86, 172101, 2005

[92] M.A. Mastro, J.R. LaRoche, N.D. Bassim and C.R. Eddy, Jr: *Simulation on the effect of non-uniform strain from the passivation layer on AlGaN/GaN HEMT,* Microelectronics Journal 36 (8), p. 705, 2005

[93] A. Kikuchi, R. Bannai, K. Kishino, C.-M. Lee, J.-I. Chyi: *AlN/GaN double-barrier resonant tunneling diodes grown by rf-plasma-assisted molecular-beam epitaxy*, Applied Physics Letters 81 (9), p. 1729, 2002

[94] C.T. Foxon, S.V. Novikov, A.E. Belyaev, L.X. Zhao, O. Makarovsky, D.J. Walker, L. Eaves, R.I. Dykeman, S.V. Danylyuk, S.A. Vitusevich, M.J. Kappers, J.S. Barnard, C.J. Humphreys: *Current-voltage instabilities in GaN/AlGaN resonant tunnelling structures*, Physica Status Solidi C 0, p. 2389, 2003

[95] A.E. Belyaev, O. Makarovsky, D.J. Walker, L. Eaves, C.T. Foxon, S.V. Novikov, L.X. Zhao, R.I. Dykeman, S.V. Danylyuk, S.A. Vitusevich, M.J. Kappers, J.S. Barnard, C.J. Humphreys: *Resonance and current instabilities in AlN/GaN resonant tunnelling diodes*, Physica E 21, p. 752, 2004

[96] A. E. Belyaev, C. T. Foxon, S. V. Novikov, O. Makarovsky, and L. Eaves, M. J. Kappers and C. J. Humphreys *Comment on ''AlN/GaN double-barrier resonant tunneling diodes grown by rf-plasma-assisted molecular-beam epitaxy''*, Applied Physics Letters 83 (17), p. 3626, 2003

[97] A. Kikuchi, R. Bannai, K. Kishino, C.-M. Lee, J.-I. Chyi: *Response to "Comment on `AlN/GaN double-barrier resonant tunneling diodes grown by rf-plasma-assisted molecular-beam epitaxy' "*, Applied Physics Letters 83 (17), p. 3628, 2003

[98] S. Golka, C. Pflugl, W. Schrenk, G. Strasser, C. Skierbiszewski, M. Siekacz, I. Grzegory, S. Porowski: *Negative differential resistance in dislocation-free GaN/AlGaN double-barrier diodes grown on bulk GaN*, Applied Physics Letters 88, 172106, 2006

[99] R.B. Fair: *Rapid Thermal Processing: Science and Technology*, 1993

[100] A.E. Belyaev, J. Breza, E.F. Venger, M. Vesely, I.Yu. Il'in, R.V. Konakova, J. Liday, V.G. Lyapin, V.V. Milenin, I.V. Prokopenko, Yu.A. Tkhorik: *Radiation resistance of GaAs-based microwave Schottky-barrier devices*, Kiev, Interpress Ltd., 1998

[101] E.D. Atanassova, A.E. Belyaev, R.V. Konakova, P.M. Lytvyn, V.V. Milenin, V.V.Shynkarenko: *Effect of active actions on the properties of semiconductor materials and structures*, Kharkiv: NTC, 2007

[102] A.E. Belyaev, E.F. Venger, I.B. Ermolovich, R.V. Konakova, P.M. Lytvyn, V.V. Milenin, I.V. Prokopenko, G.S. Svechnikov, E.A. Soloviev, L.L. Fedorenko: *Effect of microwave and laser radiation on the parameters of semiconductor structures*, Kyiv, Intas, 2002

[103] M. Linde, S. J. Uftring, and G. D. Watkins, V. Härle, F. Scholz: *Optical detection of magnetic resonance in electron-irradiated GaN*, Physical Review B 55 (16), R10177, 1997

[104] C. Bozdog, H. Przybylinska, G. D. Watkins, V. Harle, F. Scholz, M. Mayer, M. Kamp, R. J. Molnar, A. E. Wickenden, D. D. Koleske, R. L. Henry: *Optical detection of electron paramagnetic resonance in electron-irradiated GaN*, Physical Review B 59, 12479, 1999

[105] S. A. Vitusevich, N. Klein, A. E. Belyaev, S. V. Danylyuk, M. V. Petrychuk, R. V. Konakova, A. M. Kurakin, A. E. Rengevich, A. Y. Avksentyev, B. A. Danilchenko, V. Tilak, J. Smart, A. Vertiatchikh, L. F. Eastman: *Effects of γ-irradiation on AlGaN/GaN-based HEMTs*, Physica Status Solidi A 195, p. 101, 2003

[106] G.A. Umana-Membreno, J.M. Dell, G. Parish, B.N. Nener, L. Faraone, R. Ventury, U.K. Mishra: *Effects of ^{60}Co gamma-irradiation on two-dimentional electron gas transport and device characteristics of AlGaN/GaN HEMTs,* phys. stat. sol. 1-4 (2005)

[107] O. Aktas, A. Kuliev, V.. Kumar, R. Schwint, S. Toshkov, D. Costescu, J. Stubbins, I. Adesida: *60Co gamma radiation effects on DC, RF, and pulsed I-V characteristics of AlGaN-GaN HEMTs,* Solid-State Electronics 48 (2004) 471-475

[108] B.Luo, J.W. Johnson, F.Ren, K.K. Allums, C.R. Abernathy, S.J. Pearton, A.M. Dabiran, A.M. Wowchak, C.J. Polley, P.P. Chow, D. Schoenfeld, A.G. Baca: *Influence of 60Co gamma-rays on dc performance of AlGaN/GaN HEMT,* Applied Physics Letters vol 80, No. 4 (2002)

[109] M. R. Hogsed, Y. K. Yeo, M. Ahoujja, M.-Y. Ryu, J. C. Petrosky, R. L. Hengehold: *Radiation-induced electron traps in* $Al_{0.14}Ga_{0.86}N$ *by 1 MeV electron radiation*, Applied Physics Letters 86, 261906, 2005

[110] D. C. Look, D. C. Reynolds, J. W. Hemsky, J. L. Sizelove, R. L. Jones, R. J. Molnar: *Defect Donor and Acceptor in GaN*, Physical Review Letter **79**, p. 2273, 1997

[111] D. C. Look, G. C. Farlow, P. J. Drevinsky, D. F. Bliss, J. L. Sizelove: *On the nitrogen vacancy in GaN*, Applied Physics Letters 83, p. 3525, 2003

[112] T. Kelly: *Irradiation Damage to Solids,* Pergamon, New York, 1966

[113] S.A. Vitusevich, N. Klein, A.E. Belyaev, S.V. Danylyuk, M.V. Petrychuk, R.V Konakova, A.M. Kurakin, A.E. Rengevich, A.Yu. Avksentiev, B.A. Danilchenko, V. Tilak, J. Smart, A. Vertiatchikh, L.F. Eastman: *Radiation hardness of AlGaN/GaN based HEMTs*, Material Research Society Symposium Proceedings 719, p. 133, 2002

[114] M.A. Herman, W. Richter and H. Sitter: *Epitaxy: Physical Principles and Technical Implementation*, Springer, 2004

[115] J.H. Edgar, S.T. Strite, I.Akasaki, H. Amano, C.Wetzel: *Properties, processing and application of Gallium Nitride and related semiconductors*, INSPEC, 1999

[116] G.S. May, C.J. Spanos: *Fundamentals of Semiconductor Manufacturing and Process Control*, John Wiley & Sons Inc., 2006

[117] Z. Bougrioua, I. Moerman, L. Nistor, B. Van Daele, E. Monroy, T. Palacios,F. Calle, and M.Leroux: *Engineering of an insulating buffer and use of AlN interlayers: two optimisations for AlGaN-GaN HEMT-like structures,* Physica Status Solidi (a) **195 (1)**, p. 93, 2003

[118] J.R. Shealy, V. Kaper, V. Tilak, T. Prunty, J.A. Smart, B. Green, and L.F. Eastman: *An AlGaN/GaN high-electron-mobility transistor with an AlN sub-buffer layer,* Journal of Physics: Condensed Matter **14(13)**, p. 3499, 2002

[119] N.Nastase, H.Hardtdegen, R.Schmidt, H.Bay, H Lüth, A.Alam, and M.Heuken: The *Influence of Nucleation Parameters on GaN Buffer Layer Properties Used for HEMT Application*, Physica Status Solidi (a) **188(2)**, p. 647, 2001

[120] C. Enss, S. Hunklinger: *Low-temperature physics*, Springer, 2005

[121] By Martin N. Wilson: *Superconducting magnets*, Oxford University Press, 1987

[122] M. Grundmann: *The Physics of Semiconductors*, Springer, 2006

[123] H. Fröhlich: *Electrons in lattice fields*, Advances In Physics 3(11), p. 325, 1954

[124] G. Bastard *Wave mechanics applied to semiconductor heterostructures*, EDP Sciences, 1992

[125] Ya.A. Bychkov, E.I. Rashba: *Properties of a 2D electron gas with lifted spectral degeneracy*, JETP Letters 39 (2), p.78, 1984

[126] G. Engels, J. Lange, Th, Schäpers, H. Lüth *Experimental and theoretical approach to spin splitting in modulation-doped InxGa1-xAs/InP quantum wells for B→0*, Physical Review B 55(4), R1958, 1997

[127] T. Ihn: *Electronic Quantum Transport in Mesoscopic Semiconductor Structures weak localization*, Springer, 2004

[128] A.Punnoose: *Magnetoconductivity in the presence of Bychkov-Rashba spin-orbit interaction*, Applied Physics Letters 88, 252113, 2006

[129] S. Hikami, A.I. Larkin, Y. Nagaoka: *Spin-Orbit Interaction and Magnetoresistance in the Two Dimensional Random System*, Progress of Theoretical Physics 63(2), p. 707, 1980

[130] M.A.Brummell, R.J.Nicholas, L.C.Brunel, S.Huant, M.Baj, J.C.Portal, M.Razeghi, M.A.Di Forte-Poisson, K.Y.Cheng, and A.Y.Cho: *Cyclotron resonance and polaron effects in a two-dimensional electron gas in GaInAs*, Surface Science **142**, p. 380, 1984

[131] T.Ando, A.B.Fowler, and F.Stern: *Electronic properties of two-dimensional systems*, Reviews of Modern Physics **54**, p. 437, 1982

[132] M.Drechsler, D.M.Hofmann, B.K.Meier, T.Detchprohm, H.Amano, and I.Akasaki: *Determination of the Conduction Band Electron Effective Mass in Hexagonal GaN*, Japanese Journal of Applied Physics **34**, L1178, 1995

[133] S.Das Sarma: *Polaron effective mass in GaAs heterostructure*, Physical Review B **27**, p. 2590, 1983

[134] N. Wiener: *Generalized Harmonic Analysis*, Acta Mathematica 55, p. 117, 1930

[135] Van der Ziel: *Noise in solid state devices and circuits*, John Wiley & Sons Inc, 1986

[136] J. A. Garrido, B. E. Foutz, J. A. Smart, J. R. Shealy, M. J. Murphy, W. J. Schaff, and L. F. Eastman, E. Muñoz: *Low-frequency noise and mobility fluctuations in AlGaN/GaN heterostructure field-effect transistors*, Applied Physics Letters 76(23), p. 3442, 2000

[137] A.L. MacWhorter: in *Semiconductor Surface Physics*, Ed. R.H. Kingston, Philadelphia PA, Univ. of Philadelphia Press, 207, 1957

[138] F.N. Hooge: *1/f noise is no surface effect*, Physical Letters A 29, p. 139, 1969

[139] J.-M. Peransin, P. Vignaud, D. Rigaud, and L. K.J. Vandamme: *1/f Noise in MODFET's at low drain bias*, IEEE Trans. on Electron. Devices **37**, p. 2250, 1990

[140] F. N. Hooge: *On the additivity of generation–recombination spectra. Part 1: Conduction band with two centres*, Physica B **311**, p. 238, 2002

[141] B. K. Ridley: *Coupled surface and channel transport in semiconductor heterostructures*, Journal Applied Physics **90**, p. 6135, 2001

[142] M. Poudysegur, J. Graffeuil, and J.-L. Cazaux: *Origin of 1/f/sup 3/2/ noise in GaAs thin-film resistors and MESFETs*, IEEE Trans. on Electron. Devices **34**, p. 2178, 1987

[143] J.Liberis and A.Matulionis: *Hot-electron noise in nitride 2DEG Channels*, in Noise and Fluctuations, edited by Josef Sikula, Brno: CNRL Publisher, 2003, pp. 241-246.

[144] A.Matulionis, J.Liberis, I.Matulioniene, M.Ramonas, L.F.Eastman, J.R.Shealy, V.Tilak and A.Vertiatchikh: *Hot-phonon temperature and lifetime in a biased* $Al_xGa_{1-x}N/GaN$ *channel estimated from noise analysis*, Physical Review B **68**, 035338, 2003

[145] L. Ardaravicius, J.Liberis, A.Matulionis, L.F.Eastman, J.R.Shealy and A. Vertiatchikh: *Self-heating and microwave noise in AlGaN/GaN*, Physica Status Solidi (a) **201**, p.203, 2004

[146] G.H.Olsen and M.Ettenberg: *Calculated stresses in multilayered heteroepitaxial structures*, Journal Applied Physics **48**, p. 2543, 1977

Acknowledgements

I would like to acknowledge the contribution of my supervisors, colleges and partners to the results presented in the frame of this work:

Dr. N. Klein, Dr. S. Vitusevich, Dr. S. Danylyuk

IBN-2, Forschungszentrum Juelich, Germany

Prof. A.E. Belyaev, Prof. R.V. Konakova

Institute of Semiconductor Physics, National Academy of Sciences of Ukraine, Ukraine

Prof. A.E. Danylchenko

Institute of Physics, National Academy of Sciences of Ukraine, Ukraine

Dr. M.V. Petrychuk

Taras Shevchenko National University, Ukraine

Special Thanks to our Technology Partners:

H. Hardtdegen group, IBN-1, Forschungszentrum Juelich, Germany

L.F. Eastman group, Cornell University, USA

C.T.Foxon group, University of Nottingham, UK

Centre de Recherche sur l'Hétéro-Epitaxie et ses Applications (CRHEA), France

Personal Publication List:

1. **Dynamic redistribution of the electric field of the channel in AlGaN/GaN high electron mobility transistor with nanometer-scale gate length.** S. A. Vitusevich, S. V. Danylyuk, ***A. M. Kurakin***, N. Klein, H. Luth, V. Petrychuk, A. E. Belyaev. // APPLIED PHYSICS LETTERS **87**, 192110 2005

2. **Origin of noise in AlGaN/GaN heterostructures in the range of 10–100 MHz.** S. A. Vitusevich, S. V. Danylyuk, ***A. M. Kurakin***, N. Klein, and A. Offenhausser, M. V. Petrychuk, A. E. Belyaev. // JOURNAL OF APPLIED PHYSICS **99**, 073706 2006

3. **Capacitance characterization of AlN/GaN double-barrier resonant tunnelling diodes.** ***A. M. Kurakin***, S. A. Vitusevich, S. V. Danylyuk, A. V. Naumov, C. T. Foxon, S. V. Novikov, N. Klein, H. Luth, and A. E. Belyaev. // phys. stat. sol. (c) 3, No. 6, 2265–2269 (2006)

4. **Effects of *γ*-irradiation on AlGaN/GaN-based HEMTs.** S. A. Vitusevich, N. Klein, A. E. Belyaev, S. V. Danylyuk, M. V. Petrychuk, R. V. Konakova, ***A. M. Kurakin***, A. E. Rengevich, A. Yu. Avksentyev, B. A. Danilchenko, V. Tilak, J. Smart, A. Vertiatchikh, and L. F. Eastman. // phys. stat. sol. (a) 195, No. 1, 101– 105 (2003)

5. **Low-frequency noise in AlGaN/GaN HEMT structures with AlN thin film layer.** S. A. Vitusevich, O. A. Antoniuk, M. V. Petrychuk, S. V. Danylyuk, ***A. M. Kurakin***, A. E. Belyaev, and N. Klein. // phys. stat. sol. (c) 3, No. 6, 2329–2332 (2006)

6. **Influence of surface passivation on low-frequency noise properties of AlGaN/GaN high electron mobility transistor structures.** S. A. Vitusevich, M. V. Petrychuk, S. V. Danylyuk, ***A. M. Kurakin***, N. Klein,and A. E. Belyaev. // phys. stat. sol. (a) **202**, No. 5, 816–819 (2005)

7. **Effect of Gamma Radiation on the Characteristics of Gallium Nitride HEMT Heterostructures.** ***A.M.Kurakin*** // Technical Phys. Lett. 29 (9), 748-749 (2003)

8. **Quantum confinement effect on the effective mass in two-dimensional electron gas of AlGaN/GaN heterostructures.** ***A.M. Kurakin***, S. A. Vitusevich, S. V. Danylyuk, H. Hardtdegen, N. Kaluza, N. Klein, Z. Bougrioua, A.V. Naumov and A. E. Belyaev. // Physical Review B, *submitted*

9. **Improvement of electrical characteristics of the two-dimensional electron gas in AlGaN/GaN heterostructures under small dose gamma-quanta irradiation.** ***A.M. Kurakin***, S.A. Vitusevich, S.V. Danylyuk, H. Hardtdegen, N. Kaluza, N. Klein, Z. Bougrioua, B.A. Danilchenko, R.V. Konakova and A.E. Belyaev. // Physical Review B, *submitted*

10. **Low-temperature transport in AlGaN/GaN 2D electron systems.** S.A. Vitusevich, ***A.M. Kurakin***, S.V. Danylyuk, N.Klein, H. Lüth, A.E. Belyaev // 27th International Conference on the Physics of Smiconductors, p. 255 (2004)

11. **Radiation hardness of AlGaN/GaN based HEMTs.** S.A. Vitusevich, N. Klein, A.E. Belyaev, S.V. Danylyuk, M.V. Petrychuk, R.V. Konakova, ***A.M. Kurakin***, A.E. Rengevich, A.Yu. Avksentyev, B.A. Danylchenko, V. Tilak, J. Smart, A. Vertiatchikh, L.F. Eastman // Material Research Society Symposium proceedings vol. 719, pp. 133-138 (2002)

12. **High-frequency noise in AlGaN/GaN heterostructures.** S.A. Vitusevicg, M.V. Petrychuk, S.V. Danylyuk, A.M. Kurakin, A.E. Belyaev //Unsolved Problems of Noise and Fluctuations 2005, pp. 131-136 (2005)

13. **Influences of Small Doses of Gamma Irradiaiton on Transport and Noise Properties of SiC MESFETs.** S.A. Vitusevich, M.V. Petrychuk, ***A.M. Kurakin***, S.V. Danylyuk, A.E. Belyaev, H.-Y. Cha, M.G. Spencer, L.F. Eastman, N. Klein // 18th International Conference on Noise and Fluctuations, pp. 713-716 (2005)

14. **Noise study of AlGaN/GaN HEMTs and X-Band Oscillators.** S.V. Danylyuk, S.A. Vitusevich, ***A.M. Kurakin***, N. Klein // Proceedings of the International Nanoelectronics Workshop, Forschungszentrum Jülich, February 9-11, 2005. - S. 167

15. **Low-temperature transport in AlGaN/GaN 2D electron systems.** S.A. Vitusevich, ***A.M. Kurakin***, S.V. Danylyuk, N. Klein, H. Lueth, A.E. Belyaev // Proceedings of the 27th International Conference on the Physics of Semiconductors (ICPS27), S. 439 – 440 (2004)

16. **Magnetoresistance of Two-Dimensional Electron GaS in AlGaN/GaN Quantum-Sized Heterostructures.** S.A. Vitusevich, ***A.M. Kurakin***, S.V. Danylyuk, N. Klein, H. Lueth, A.E. Belyaev // Proceedings of the International Nanoelectronics Workshop, Forschungszentrum Jülich, February 9-11, 2005. - S. 161 – 162

17. **Transport and noise features in AlGaN/GaN field effect transistors with nanometer-scaling gate length.** S.A. Vitusevich, M.V. Petrychuk, S.V. Danylyuk, ***A.M. Kurakin***, N. Klein, H. Lüth, A.E. Belyaev // International Journal of Nanoscience, 4 (2005), 999

18. **Improved Performance of 4H-SiC MESFETs under Small Doses of Gamma Radiation Treatment.** S.A. Vitusevich, M.V. Petrychuk, ***A.M. Kurakin***, S.V. Danylyuk, A.E. Belyaev // Proceedings of the 29th Workshop on Compound Semiconductor Devices and Integrated Circuits, - 2005. - S. 73 – 75

19. **Barrier material improvement in AlGaN/GaN microwave transistors under gamma irradiation treatment.** S.A. Vitusevich, M.V. Petrychuk, N. Klein, S.V. Danylyuk, A.E. Belyaev, R.V. Konakova, A.Yu. Avksentyev, ***A.M. Kurakin***, P.M. Lytvyn, B.A. Danilchenko, V. Tilak, J. Smart, A. Vertiatchikh, L.F. Eastman // Materials Research Society Symposium proceedings ; 764. - 1-55899-701-6. - S. 183 – 188 (2003)

20. **Low-temperature peculiarities of AlGaN/GaN heterostructure transport.** ***A. Kurakin***, S. Vitusevich, S. Danylyuk, N. Klein, A. Belyaev // 2006 APS March Meeting proceedings

Appendix A. Photolithography Masks

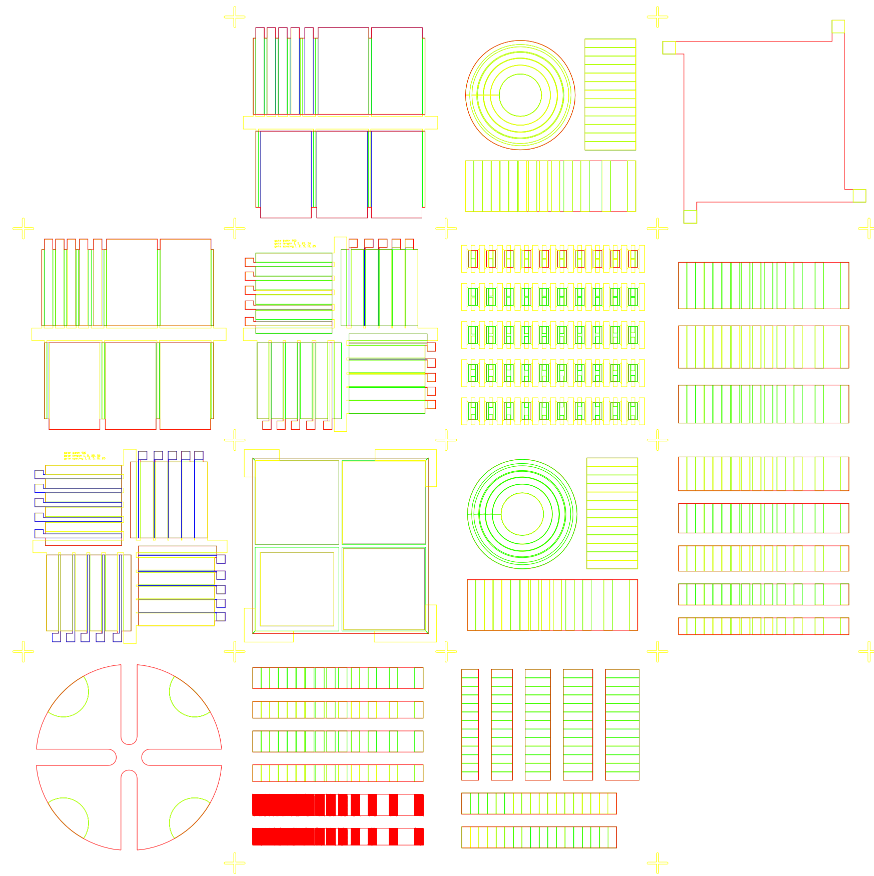

Mask 1. TLMs, Schottky diodes, Van der Pauw structures

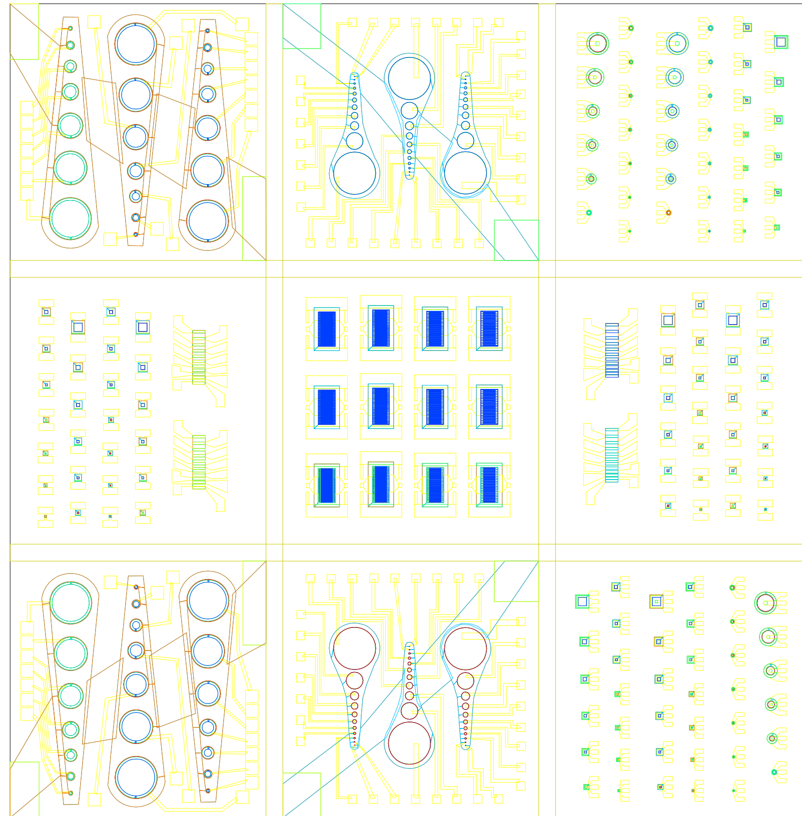

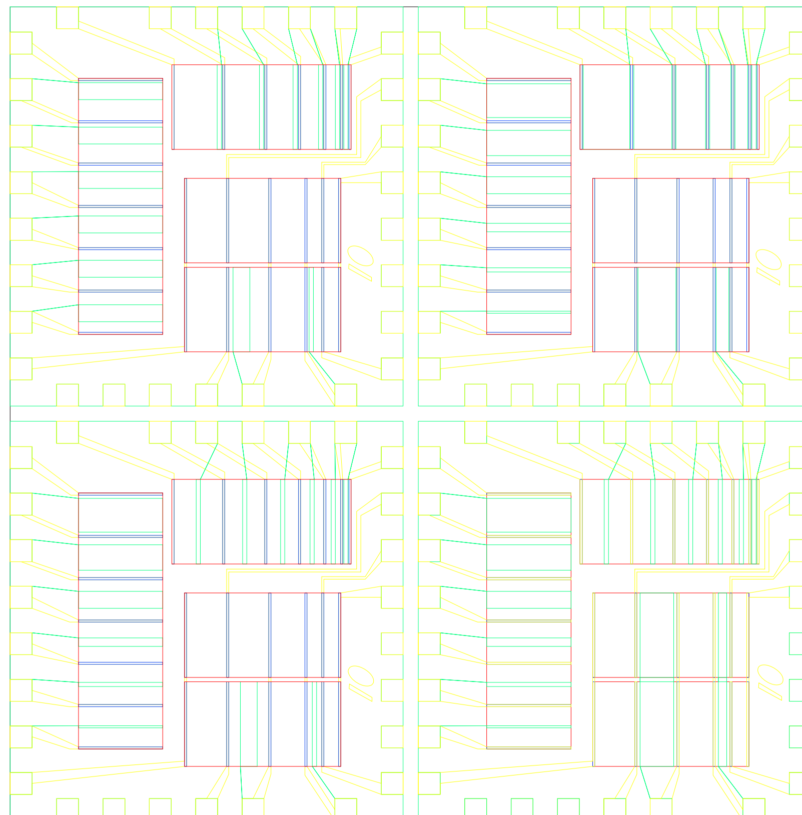

Mask 2. RTDs & Transistors

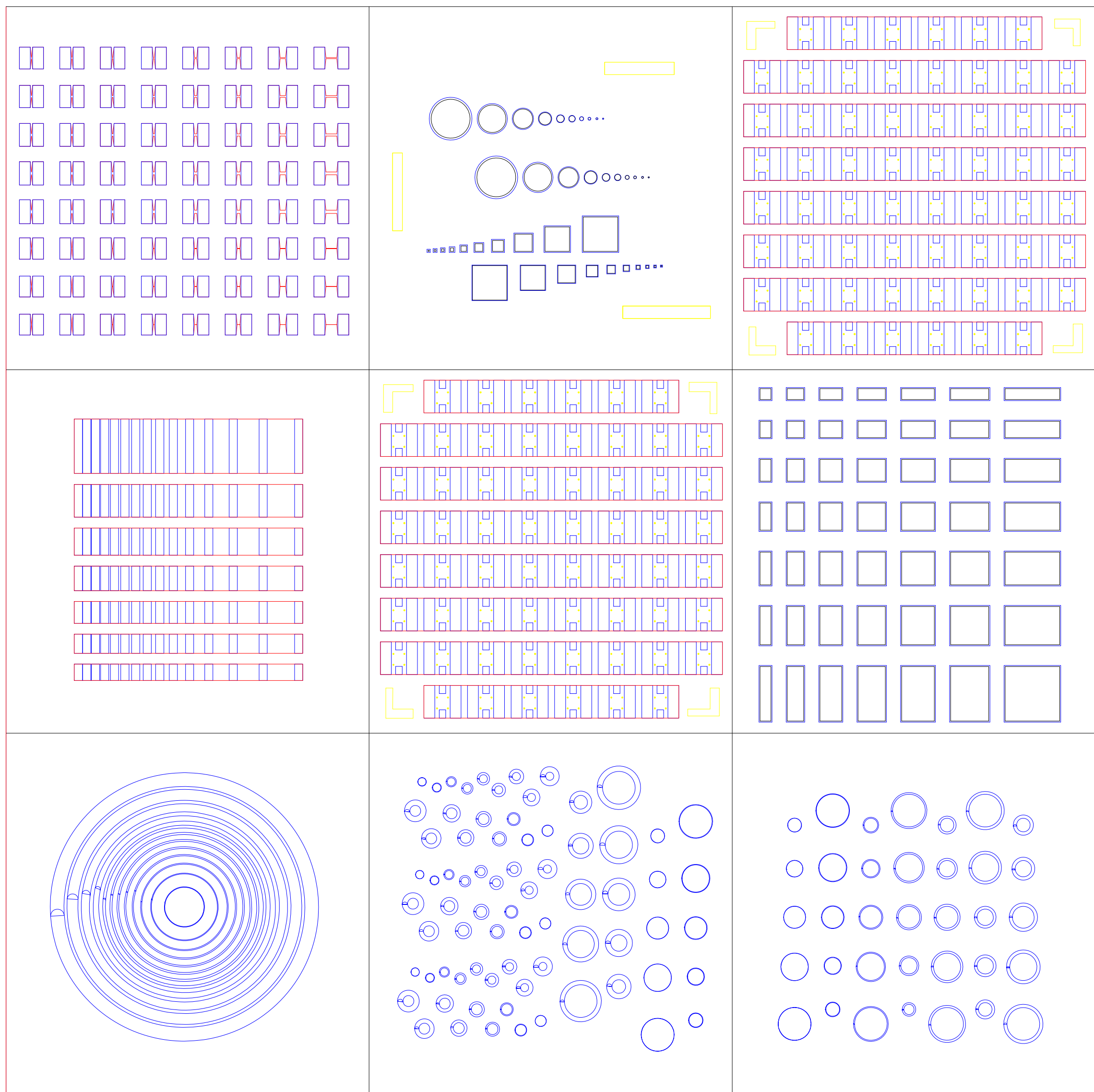

Mask 3. circle TLMs, Schottky diodes

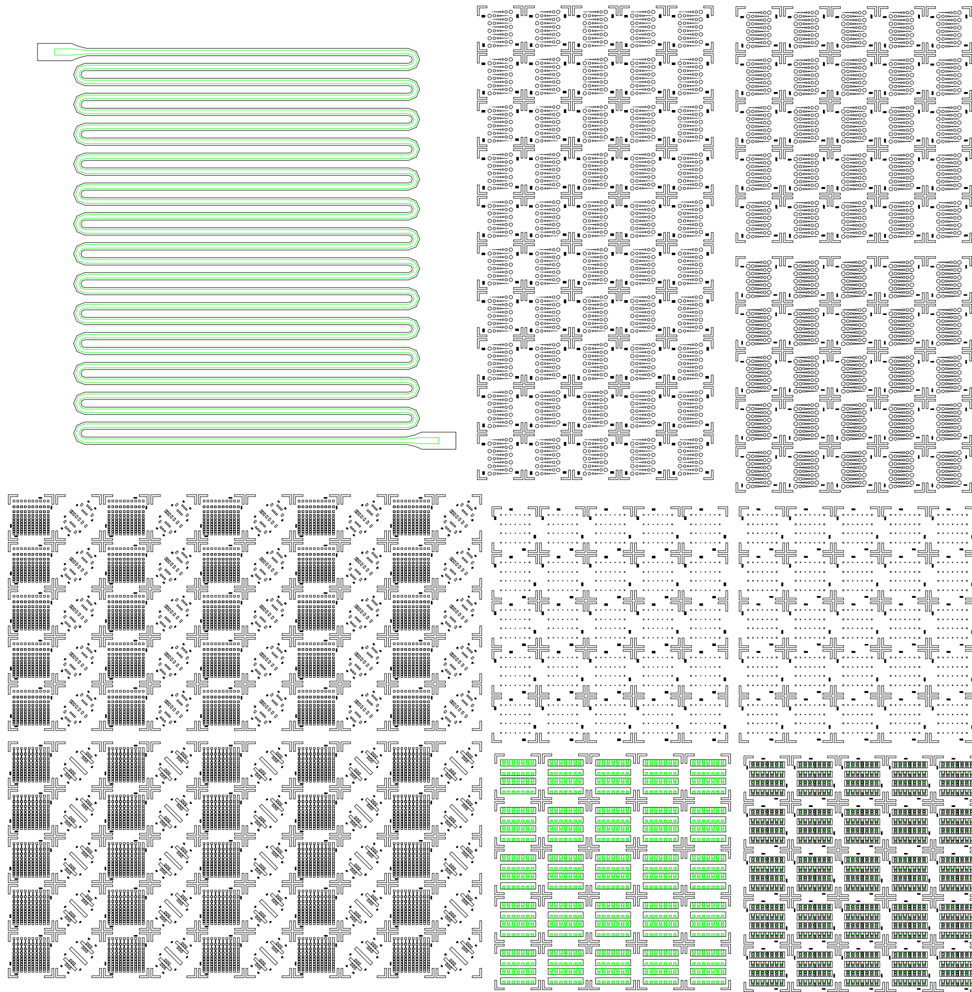

Mask 4. Hall bars, TLMs

Appendix B. Digamma Function

The digamma function is the logarithmic derivative of the gamma function.

$$\psi(z) = \frac{d[\ln\Gamma(z)]}{dz} = \frac{\Gamma'(z)}{\Gamma(z)} \qquad \text{(A.1)}$$

where Γ(z) is the usual Gamma function:

$$\Gamma(z) = \int_0^\infty t^{(z-1)} e^{-t} dt \qquad \text{(A.2)}$$

The most important properties of digamma function are:

1) $\psi(z+1) = \psi(z) + \psi(1/z)$ (A.3)

2) $\psi(z) \approx -\gamma - \frac{1}{z}$ as $z \to 0$ (A.4)

3) $\psi(z) \approx \ln(z) - \frac{1}{2z} - \frac{1}{12z^2}$ when $z >> 1$ (A.5)